THE UNIVERSITY of ADELAIDE

Exploring Possibilities to Enhance Silicon Solar Cell Efficiency by Downconversion of Sunlight

by

Muddassar Naeem

Thesis submitted for the fulfilment of the degree of

Master of Philosophy

The University of Adelaide

School of Chemistry and Physics

April 2015

Statement of Declaration

I certify that this work contains no material which has been accepted for the award of any other degree or diploma in my name, in any university or other tertiary institution and, to the best of my knowledge and belief, contains no material previously published or written by another person, except where due reference has been made in the text. In addition, I certify that no part of this work will, in the future, be used in a submission in my name, for any other degree or diploma in any university or other tertiary institution without the prior approval of the University of Adelaide and where applicable, any partner institution responsible for the joint-award of this degree.

I give consent to this copy of my thesis, when deposited in the University Library, being made available for loan and photocopying, subject to the provisions of the Copyright Act 1968.

I also give permission for the digital version of my thesis to be made available on the web, via the University's digital research repository, the Library Search and also through web search engines, unless permission has been granted by the University to restrict access for a period of time.

Muddassar Naeem

Supervisors:

Prof. Jesper Munch

A/Prof. Murray Hamilton

A/Prof. Heike Ebendorff-Heidepriem

STATEMENT OF DECLARATION

To my family

Abstract

Improving the efficiency of solar cells is an active area of research in photovoltaic industry. The research work presented in this dissertation is based on a quest for better and improved silicon solar cells. The current work aims to explore different possibilities by studying advance approaches for PV applications. Additionally this work is intended to seek the feasibility of new photonic concepts for improving silicon solar cells.

In this work we have investigated solar downconverters consisting of tellurite glass. Their fabrication process is discussed followed by the experimental characterization. Optical measurements such as absorption spectra, fluorescence spectra and fluorescence quantum efficiency are undertaken. These optical measurements enabled to understand physical processes associated with the materials used.

Furthermore, the work presented in the thesis is focused on the realization of a downconverter. The work can be roughly sub-divided into two parts. One part identifies the suitable energy conversion materials and the second part deals with the development and demonstration of the experimental method for characterizing a downconverter. The final part of the work extends investigation for more efficient materials prior to their use at the practical level. We also propose an architectural design for the efficient use of a downconverter with a silicon solar cell.

Acknowledgements

First of all, I would like to thank my principal supervisor, Jesper Munch, for the opportunity to be a part of his group and to be able to work on an interesting problem. I am grateful for a number of discussions and meetings as well as encouragement, care and support. I acknowledge his efforts and guidance to accomplish this work. I thank him for proof-reading of the thesis during write-up. And of course his mentorship enriched in me will stay forever.

I am very grateful to my co-supervisors, Murray Hamilton and Heike Ebendorff-Heidepriem, for their guidance throughout the work. I am highly thankful to Murray, for the provided support, assistance, many fruitful discussions, suggestions and corrections on thesis. I greatly appreciate Murray for his constructive ideas and provided necessary experimental equipment. Also I greatly thank to Heike for the provided samples to undertake investigation. Her help on sharing knowledge of glass materials at the early stage of the project was really useful.

I thank to Nigel Spooner for giving me access to his lab and lending me spectrometer and many optical components for the experimental measurements. I enjoyed on some occasions sharing ideas on experimental equipments.

I must acknowledge fruitful talks and support from David Hosken. Many thanks to the people in Optics group Peter Veitch, David Ottaway, Keiron Boyd, Miftar Ganija, Nick Chang, Ori Henderson, Ka Wu, Lachlan Harris, Nicky Huichao, Myles Clark, Sophie Hollitt, Eleanor Jeans, and Simon Curtis for their friendly talks.

I would like to thank Stephen, Erik, Mariusz, Nathan and Manuel for their friendly talks with me around the Physics department.

I also thank the people in the Physics workshop for their technical support, especially Blair Middlemess, who always prepared components as a part of my experimental setup.

I also acknowledge The University of Adelaide for the award of university research fee scholarship and other facilities to continue further studies.

On the personal side, there are many people in the family to whom I would like to thank for their continued support and best wishes. In particular, I wish to thank my Uncle, Muhammad Zia who was very kind, generous and helpful throughout my stay at Adelaide. He has always supported financially and encouraged me to persevere with research studies.

Last but not the least I would like to thank my parents who have been kind, loving and praying for me all the time. Without their support and financial help, it would not have been possible to achieve this goal. Special thanks to my sisters and a brother for their continued support, sharing joys, and encouragement. I truly wish you all the best for the whole of your lives.

Contents

List of Figures

List of Tables

List of Abbreviations

Throughout the thesis, several abbreviations will be used to represent specific short descriptions or notations, the following is a list for the readers convenience. This list is not exhaustive but every effort has been made to maintain conformity of notations used here.

AM	Air Mass
ARC	Anti-reflection coating
BP	Band-pass
CdTe	Cadmium tellurite
CIGS	Copper indium gallium arsenide
DC	Downconversion
DS	Downshifting
ECL	Escape cone loss
EQE	External quantum efficiency
FQE	Fluorescence quantum efficiency
FTIR	Fourier transform infrared
IPV	Impurity photovoltaic
IQE	Internal quantum efficiency
LED	Light emitting diode
LP	Long-pass
NIR	Near-infrared
NPR	Non-radiative phonon relaxation
OFD	Organic flourescent dyes

PCE	Photon cascade emission
PV	Photovoltaics
QC	Quantum cutting
QD	Quantum dot
QS	Quantum splitting
RE	Rare-earth
SC	Solar cell
Si	Silicon
TIR	Total internal reflection
UC	Upconversion
UV	Ultraviolet
Vis	Visible
VUV	Vacuum ultraviolet

Chapter 1

Introduction

- Motivation and background
- Advanced approaches to enhance the efficiency of Si solar cells
- Downconversion process
- Review of literature
- State-of-the-art work
- Objectives of this work
- Thesis overview

Solar energy is useful in providing a clean, sustainable, and renewable source of electric power. However, current solar cells are inefficient and could be improved to achieve better solar to electric conversion. This chapter commence with the motivation for undertaking research and then describes the advanced approaches to improve the efficiency of silicon solar cells. Further, the downconversion approach is introduced followed by the review of literature. Finally, this chapter presents the objectives and the overview of the thesis.

1.1 Motivation and background

The primary motivation is to search for approaches to improve the efficiency of primarily single junction silicon solar cells. These solar cells suffer losses which can be reduced allowing to enhance their performance. Given the statement, it is therefore natural to address the following questions: i) Why it is essential to use solar energy?, ii) Why photovoltaics?, and iii) What limits silicon solar cells efficiency?

1.1.1 Why it is essential to use solar energy?

The amount of solar energy reaching the surface of the earth every hour is greater than the amount of energy consumed by mankind over an entire year. The total power density emitted by the Sun is approximately 6.4×10^7 W/m^2 of which ~ 1370 W/m^2 is incident upon the Earth's atmosphere with no absorption in space [1]. Of this, 980 W/m^2 of the power density reaches at the Earth's surface after going through the absorption and reflection from the atmosphere. Further, the amount of energy contained in the solar light is so vast that in one year it is about twice as much as will ever be obtained from all of the Earth's non-renewable resources like coal, oil, and natural gas combined [2]. Therefore, it is important to make devices that allow us to benefit from this free available resource in nature. Solar cells are devices that convert solar energy into useful electric energy. However, solar cells are often inefficient and suffer from optical losses which are described in Section 1.1.3. One of the reasons for the inefficiency of the silicon solar cells is that they do not extract efficiently the solar energy available. Figure 1.1 shows the spectrum of solar light reaching the Earth's surface.

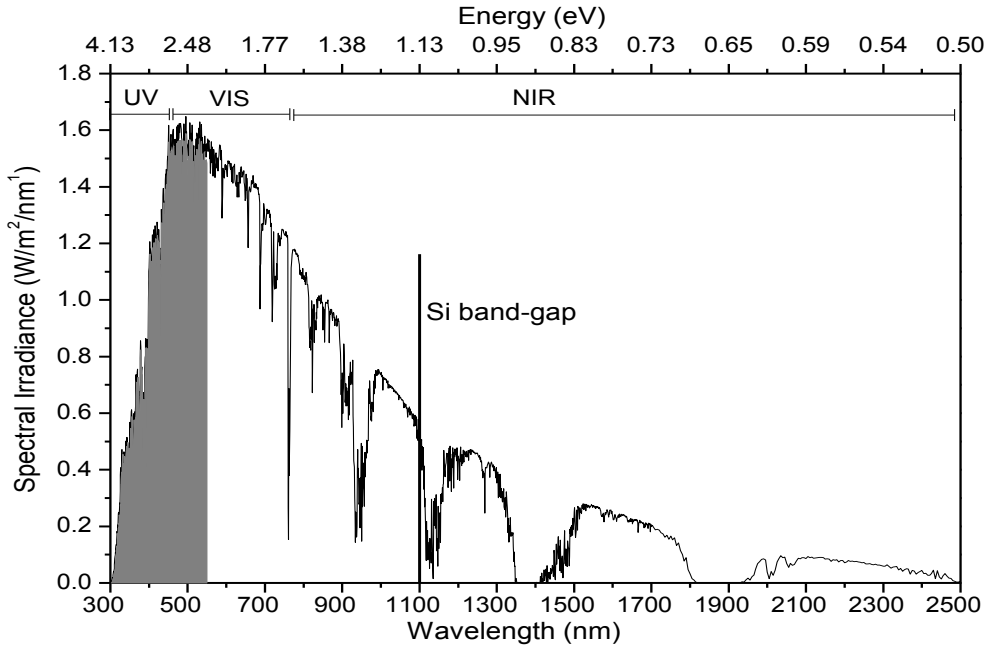

Figure 1.1: The solar spectrum (AM1.5-G[1]) of sun at the Earth's surface [3]. (Indicated is the Si band-gap wavelength (vertical line) and the shaded region indicates the fraction of solar energy potentially useful for downconversion)

This spectrum encompasses the 39% visible (VIS) and 52% near-infrared (NIR) regions with a portion of 9% in the ultraviolet (UV). In case of Si solar cells, the region of wavelengths longer than the band-gap at 1100 nm is not absorbed, while the region below 550 nm is poorly exploited. The intensity (or power density) available in the shaded region (see Figure 1.1) is 308 W/m^2, of which a maximum possible ~ 110 W/m^2 could be utilized by the Si solar cells, assuming 100% conversion efficiency. There remains an intensity of ~ 198 W/m^2 to be harnessed efficiently by the silicon solar cells. The estimated average energy per photon in the shaded region is about 3 eV. Each photon has an energy more than two times the band-gap of Si (~ 1.1 eV) and has potential to be converted into at

[1] AM stands for air mass and G for global; AM refers to the path length travelled by the solar radiation through the atmosphere.

least two lower energy photons which can be absorbed by the silicon solar cell, thereby increasing the efficiency.

1.1.2 Why photovoltaics?

The use of photovoltaics (PV) is a simple and elegant method of directly converting sunlight into useful electricity without producing air pollution or excessive heat losses. This environment friendly technology will have an improved impact upon the current global plight if the efficiency of solar cells is increased significantly prior to implementation on a massive scale in order to reduce cost and to compete with existing fossil fuels technology. PV devices (solar cells) are solid state, therefore, they are rugged and simple in design and require very little maintenance. Perhaps the main advantage of these devices is that they can be constructed as stand alone systems for use at a large scale, producing megawatts of power [4, 5].

Numerous publications have reported that silicon wafer based solar cells (single-crystalline and multi-crystalline) and thin-film solar cells (amorphous silicon and CdTe) are manufactured in the world wide PV industry, but silicon wafer based solar cells dominate (~ 90%) over the rest of PV solar cells manufacturing and sales [6, 7]. Further, there has been a rise in the production of multi-crystalline silicon solar cells than single crystalline silicon solar cells since 2005 [6]. This has been possible due to the cheaper cost of fabrication, abundance of raw silicon material, design technology for multi-crystalline silicon with a slight reduction in performance as compared to the single crystalline silicon solar cells and other PV technologies.

1.1.3 What limits Si solar cells efficiency?

Efficiency is an important factor in the photovoltaic conversion of solar energy as it determines the ultimate performance of a solar cell. The Shockley-Queisser maximum power conversion efficiency for a single junction silicon (band-gap energy ~ 1.1 eV) solar cell under AM1.5-G solar illumination is 33% [8]. The remaining 67% of incident solar energy not converted to electrical energy includes: 47% converted to heat loss through lattice thermalization, 18.5% lost to transmission of sub band-gap photons and 1.5% lost to the radiative recombination [9]. One can see that the heat loss is mainly responsible for limiting the conversion efficiency of Si solar cells.

The solar spectrum, as shown in Figure 1.1, contains photons with energies ranging from about 0.5 to 3.5 eV. Photons of energies greater than the band-gap energy (E_g) of a solar cell are not used fully which may contribute significantly to the useful electrical output. Photons with energies less than the semiconductor band-gap (E_g) are not absorbed and pass directly through the solar cell. This inefficient absorption of sunlight is due to the spectral mismatch between the solar spectrum and the solar cell material. Spectral losses, thermalization of charge carriers (electrons and holes) and the transmission losses are further explained with the aid of a schematic band diagram of a single junction solar cell as shown in Figure 1.2.

The low energy photons, also called sub band-gap photons that have energy lower than the band-gap (E_g) transmit directly through the solar cell and are lost as a transmission loss represented by (1) as illustrated in Figure 1.2. In addition, thermalization of charge carriers, generated by the absorption of high energy

photons, is another major loss mechanism which limits the performance of conventional single junction solar cells.

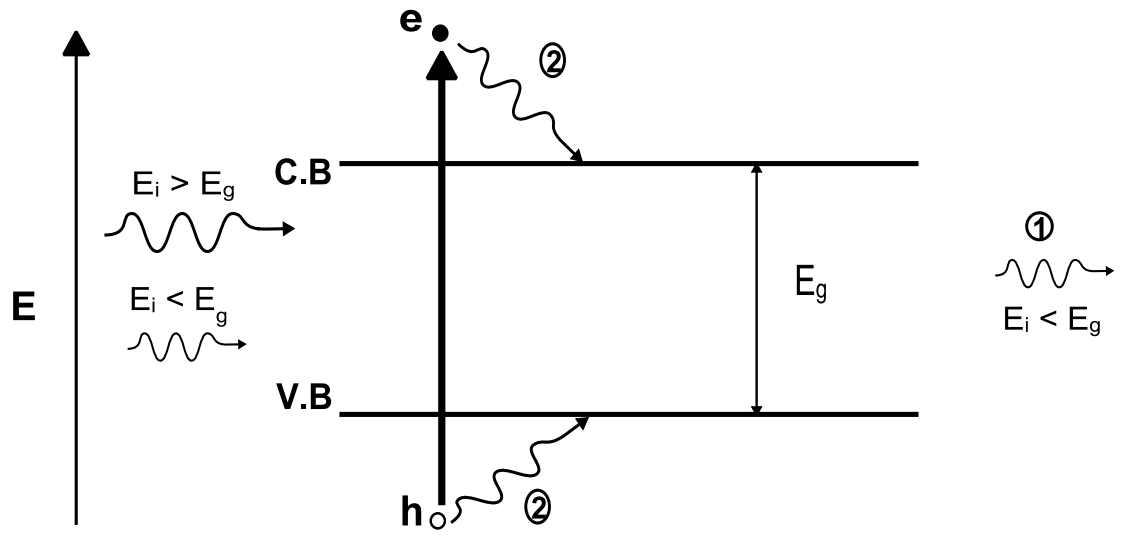

Figure 1.2: Band diagram of a single junction solar cell showing that a high energy photon is absorbed, while a low energy photon is transmitted. Thus (1) represents transmission loss while (2) represents thermalization loss. E_i is the energy of incident photon and E_g is the band-gap energy of semiconductor. (C.B and V.B stands for conduction band and valence band respectively)

The extra energy (E_i-E_g), other than that which is used for the creation of a single electron-hole (e-h) pair in the semiconductor, is lost as thermal relaxation through phonon emission and therefore known as thermalization loss which is represented by (2) as shown in Figure 1.2. It was concluded from previous investigations [7] that it is necessary to reduce these major spectral losses so that a substantial improvement in the conversion efficiency of solar cells can be achieved.

1.2 Advanced approaches to enhance the efficiency of Si solar cells

To date, photovoltaic technology may be categorized generally into three generations. The first generation of PV devices is based on crystalline Si single junction solar cells, exhibiting conversion efficiency up to 25% in laboratory settings. The second PV generation consists of thin-film amorphous silicon (a-Si), $CuInGeSe_2$ (CIGS), cadmium tellurite (CdTe) and III-V semiconductor solar cells approaching efficiencies up to 16%. However both these PV generations suffer energy losses restricting their efficiency to less than the Schockley-Queisser conversion efficiency (theoretical) limit of 33% for single junction devices [8].Thus it is important to address the trade-off between the laboratory and the theoretical efficiency for single junction solar cells.

Maximizing the efficiency of single junction solar cells is one of the major challenges PV research is facing today [7]. Third generation PV devices aim to overcome the energy losses associated with the non-absorption of below band-gap photons and the thermalization of above band-gap photons to the semiconductor band edge. Trupke et al. [10] extended the detailed balance limit theoretically and estimated that the efficiency can approach 38.6% by modifying high energy photons in the solar spectrum. However, this efficiency has not been achieved in practice. Many different third generation photovoltaic approaches have been pursued in order to reduce the major losses and subsequently increase the efficiency of silicon solar cells. These new concepts include tandem solar cells with multiple junctions [7], graded band-gap devices [7], impurity photovoltaic devices [11], hot carrier solar cells [12], intermediate band-gap solar cell [13] and photon conversion [10, 14-16].

Tandem solar cells have been studied since 1960 [7, 17]. This concept is based on an arrangement of solar cells with decreasing band-gap energies starting from the top to bottom in a stack form such that the overall solar cell exploits different parts of the solar spectrum efficiently. Such a solar cell with an infinite number of cells could reach a maximum theoretical efficiency of 86.8% under the normal direct sunlight [7, 18]. However, since these cells are in series the solar cell producing the lowest current limits the performance of the whole solar cell. Another disadvantage of this approach is that the required solar cell structures are complex and costly to fabricate.

A solar cell based on an impurity photovoltaic (IPV) effect utilizes the two step emission via impurity states within the band-gap of the semiconductor and hence sub band-gap photons are absorbed resulting in efficiency enhancement [19]. In this system, three possible transitions are required to better match the band-gap of Si. The main challenge is to find a host material with a wide band-gap such as phosphors and a sufficiently radiative luminescent species such as rare-earth elements to dope it with.

A hot carrier solar cell concept has been proposed by Ross and Nozik [20], which exceeds the Shockley-Queisser efficiency limit [8]. This approach allows efficiency enhancement by reducing energy losses related to the absorption of high energy photons greater than the band-gap energy (commonly known as thermalization loss) of semiconducting material. The idea is to extract the energy of the hot electron and hole ensembles before they cool down by interacting with the lattice [7, 12]. This requires an absorber both with slow carrier cooling properties and collection of carriers over a limited range of energies, such that cold carriers in the external contacts do not cool the hot carriers to be extracted

[21]. In this advanced model, the main difficulty is to design complex contacts, and it has not been realized in practice.

Luque and Marti [13] introduced an intermediate band-gap solar cell idea for the enhancement of solar cell efficiency which may present advantages compared to tandem solar cells. The approach is based on the idea of creating an additional half filled band in the forbidden energy gap of the solar cell material thus providing a means for induced transitions at lower energies as illustrated in Figure 1.3. In this way low energy photons are absorbed by the solar cell, and a limiting theoretical efficiency of 63.2% has been calculated for this arrangement [22]. The high energy photons lose their energy due to thermalization as they rapidly decay to the conduction band edge. Finally there remains one more problem: the intermediate band also creates new opportunities for recombination losses which are not beneficial. Thus in practice no improvement in the solar cell performance using this approach has yet been achieved.

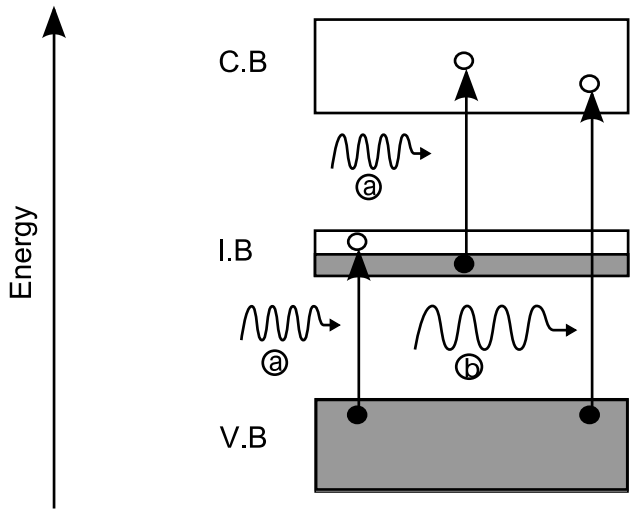

Figure 1.3: Intermediate band solar cell model (a) represents low energy photon while (b) represents high energy photon. (V.B, I.B, and C.B stands for valence band, intermediate band and conduction band; empty and filled circles represent electrons and holes respectively)

An alternative approach is photon conversion which is fundamentally unique and offers significant advantages over the first and second PV generations [10, 14]. Photon conversion can occur in three ways namely: upconversion (UC), downconversion (DC), and downshifting (DS). First the addition of two lower energy photons to obtain one higher energy photon is known as upconversion. Second, the conversion of one higher energy photon into two lower energy photons, both of which can be absorbed by the solar cell is known as downconversion. Finally, downshifting is the process whereby only one lower energy photon is obtained after non-radiative relaxation upon the absorption of one higher energy photon. Thus it has a lower efficiency which is always less than unity. As stated above, thermalization losses are the main optical losses which limit solar cells efficiency. Therefore, reducing these losses by any means could improve the solar cell efficiency. Down or upconversion processes are particularly attractive because they transform the incident spectrum, not affecting any of the physical processes inside the solar cell, can in principle be applied to existing first and second generations PV devices.

Over the last 50 years, numerous investigations regarding photon conversion have been undertaken in order to optimize silicon based solid state junction devices. While the progress has been promising further work is required to make use of all photons available in the solar spectrum rather than changing the electronic properties of the solar cell which is not simple to implement and may be expensive. One possible way for improving the efficiency of the silicon solar cell is through the spectral downconversion process which will be the subject of this thesis.

1.3 Downconversion process

Downconversion (DC) is an optical process whereby one high energy photon is converted into at least two low energy photons. The idealized DC process in a three energy level system is illustrated in Figure 1.4(a) and a corresponding schematic diagram of a combined PV device is shown in Figure 1.4(b).

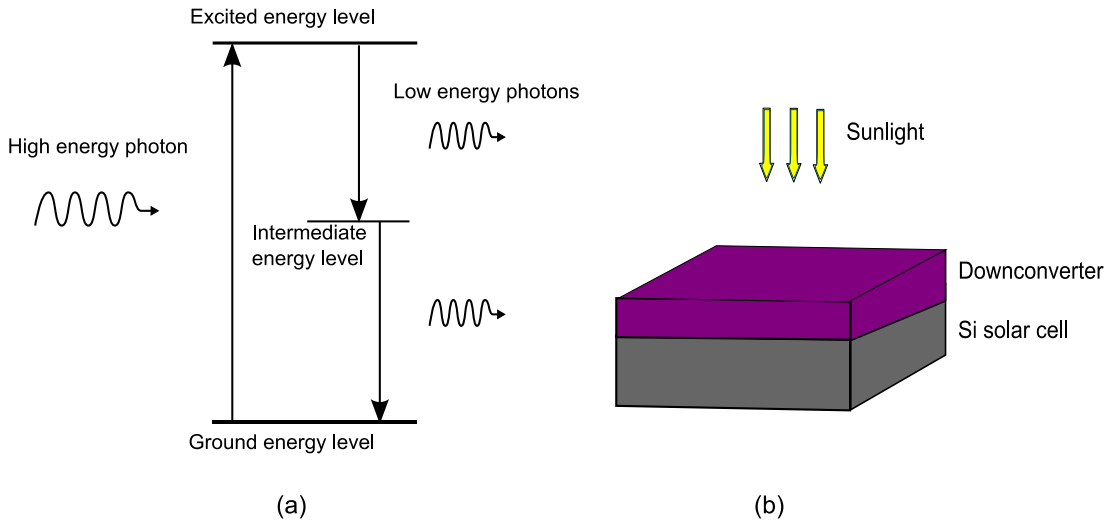

Figure 1.4: (a) DC process in a three level energy system, and (b) Combined PV device: Downconverter attached to the front of a Si solar cell.

1.3.1 Advantages and significance

There are two important benefits in successfully applying luminescent downconverters (or DC layers) to PV technologies. First, downconverting components would be passive, optical devices with carrier collection still performed via the under laying single junction solar cells. Therefore, Si solar cells with downconverter can have a distinct advantage over tandem solar cells, where the photocurrents generated in upper and lower cells must match in order to avoid significant mismatch losses. Second, the application of a downconverter to

solar cells may not require modifications to existing solar cells since they change the spectral content of the incident sunlight. A schematic representation of a downconverter attached to the front of a Si solar cell is shown in Figure 1.4(b). High energy photons are absorbed by the downconverter, thereby generating two or more lower energy photons, which are then absorbed by the Si solar cell. A maximum solar to electric conversion efficiency of 38.6% (theoretical) could be achieved for this model [10].

Downconversion is a linear optical process and therefore the efficiency is independent of the incident power. This suggests that it is possible to improve efficiency with downconversion when using un-concentrated sunlight as the illumination source. In this case, the downconverter can, for example, be mounted on top of the solar cell with a fraction of the luminescence escaping out in the direction backward to the incident sunlight. For an ideal planar downconverter with a refractive index of n = 1.5, the fraction of the converted photons lost (L_e) out through front escape cone equals ($L_e = \left[1 - \sqrt{1 - n^{-2}}\right]/2$) 12.7% [23]. It is suggested that a downconverter with external quantum efficiency[2] (EQE) greater than 115% is required to circumvent escape cone loss, assuming that emission in all directions is collected by the underlying solar cell [23]. Further explanation and analysis of the architectural configuration of a PV device is presented in Appendix A.

1.3.2 Energy transfer process

It is essential to discuss energy transfer processes before we delve into detailed mechanisms of the downconversion process. Absorption of pump light and

[2] EQE is defined as the ratio of the number of excited electrons to the number of incident photons.

emitted light can take place in a single ion or between two ions in the DC material. The same physical mechanism takes place in the downconversion process via energy transfer [24-26]. Here, we only discuss the energy transfer between two (or more) rare-earth ions; one ion is referred to as the sensitizer (S) or donor and the other ion as the activator (A) or acceptor as shown in Figure 1.5. There are several different types of energy transfer processes that can occur, which can be radiative or non-radiative. Non-radiative energy transfer can be resonant (see Figure 1.5(b)) or aided by the emission of a number of phonons to compensate energy mismatch (see Figure 1.5(c)) or only part of the energy can be transferred, which is referred to as cross-relaxation process (see Figure 1.5(d)).

The most efficient energy transfer process involves resonant overlap between the emission band and absorption band of the sensitizer and activator respectively (see Figure 1.5(a)). In this case, energy transfer occurs only if two conditions are fulfilled. Firstly, it is necessary to have spectral overlap between the sensitizer emission and the activator absorption. This condition is known as the resonance. Secondly, there should be an interaction between the two ions which can either be an exchange interaction or multipole-multipole interaction.

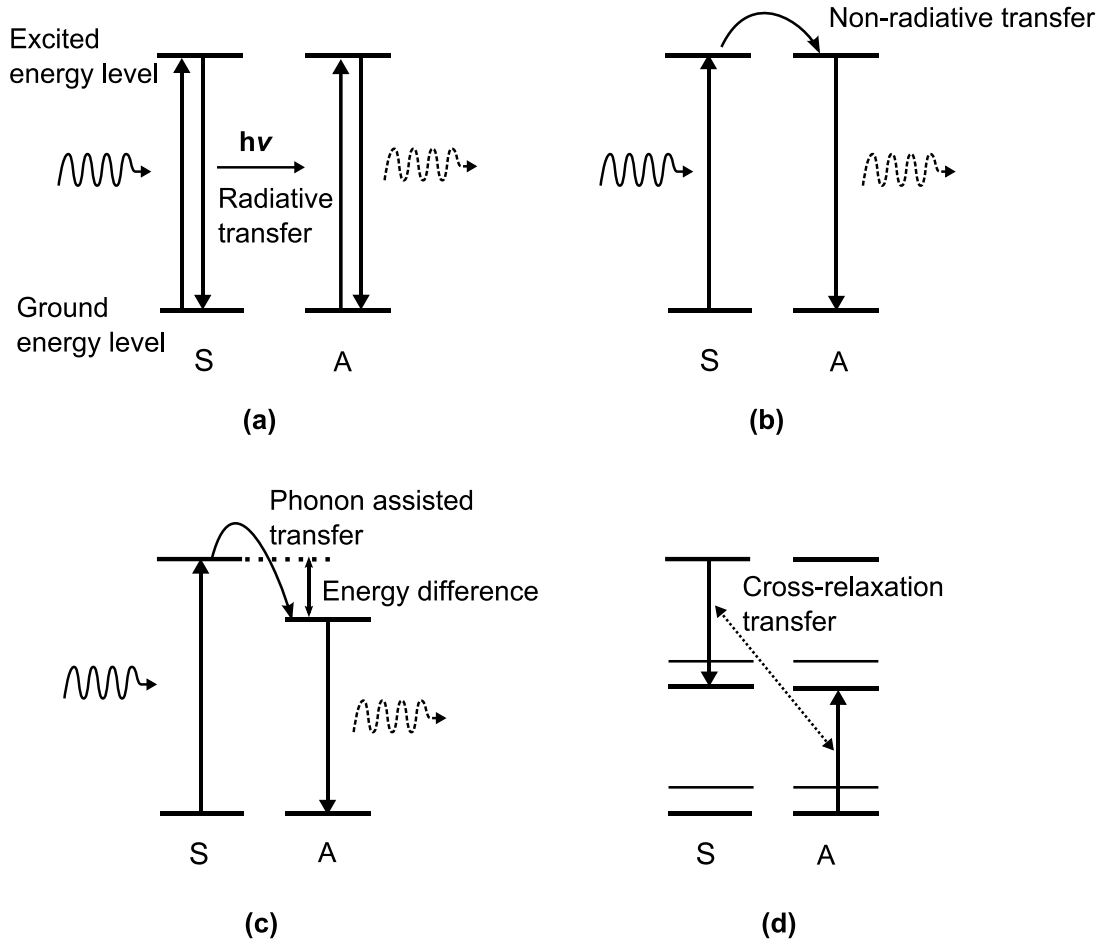

Figure 1.5: Schematic illustrations of energy transfer processes between sensitizer (S) and activator (A) ions of two energy levels (a) Resonant radiative energy transfer, (b) Non- radiative resonant energy transfer, (c) Phonon assisted non-radiative energy transfer, and (d) Cross-relaxation energy transfer process. (Solid curvy line shows the incident photon and dotted curvy line shows emitted photon, upward arrow line indicates absorption and downward arrow line indicates emission of photon)

1.4 Review of literature

Downconversion (DC) is the process where two photons of lower energy are generated upon absorption of a single high energy photon. This process is also referred to as quantum cutting (QC) or quantum splitting (QS) in the literature. The idea to obtain quantum efficiencies greater than 100% by converting a single higher energy photon into two lower energy photons was first proposed by Dexter in 1957 [27]. The suggested mechanism involved the simultaneous energy transfer from a sensitizer to two activators, each accepting half the energy of the excited sensitizer. It was not demonstrated until 1974 when experimental evidence of quantum efficiencies greater than 100% was found for the system $YF_3:Pr^{3+}$. The mechanism was not the same as proposed by Dexter, but involved two sequential emissions from the high energy level ^1S_o of Pr^{3+} ($^1S_o \rightarrow {}^1I_6$ followed by relaxation to the ^3P_o level and emission of a second visible photon from ^3P_o) [28, 29]. These emissions can be observed in Figure 1.6.

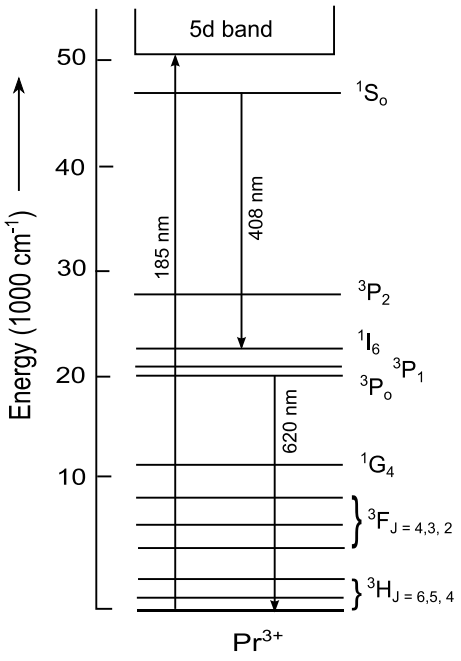

Figure 1.6: Quantum cutting upon the absorption of VUV photon (185 nm) resulting into emissions of a blue (408 nm) and red (620 nm) photons in Pr^{3+} ion.

Later in 1999, quantum cutting via two sequential energy transfer steps in rare-earth ions pair (Gd–Eu) was observed and based on the analogy with the two-step energy transfer process leading to upconversion, it was named ‘downconversion’ [30]. The experimental objective was to obtain the emission of two visible photons from a single UV photon in order to enhance the efficiency of light emitting diodes. In 2002, the potential of the downconversion scheme for increasing the efficiency of solar cells was demonstrated [10]. Several processes involved in downconversion are shown in Figure 1.7.

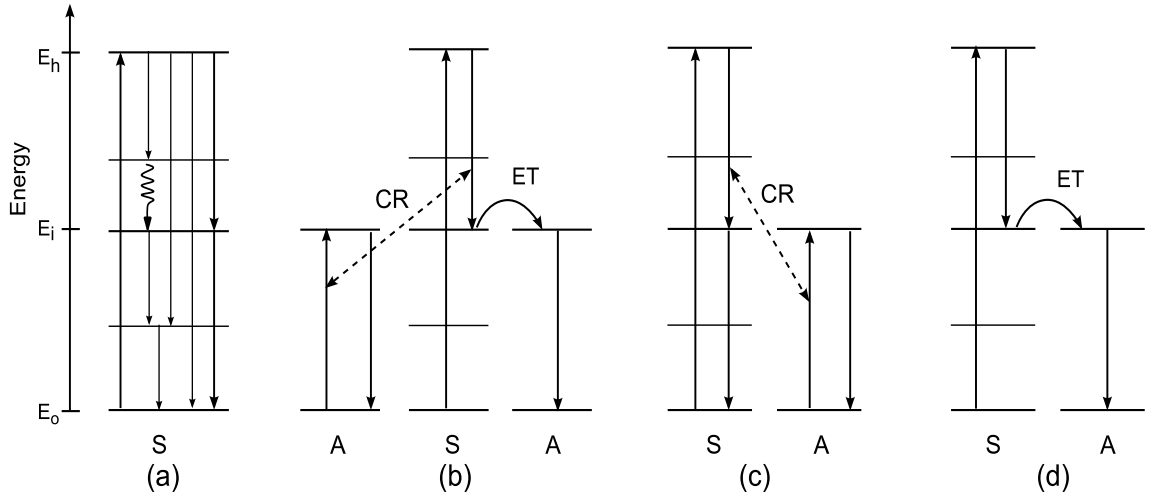

Figure 1.7: Schematic representation of several downconversion mechanisms in energy levels of sensitizer (S) and activator (A) ion; E_h, E_i, and E_o along energy axis shows higher, intermediate and ground energy levels respectively. (a) One or more emissions from a single ion S, (b) Downconversion in two ions: Cross-relaxation from ion S to ion A (1) and energy transfer (ET) from ion S to ion A (2) with emission from ion A, and (c, d) Cross-relaxation (CR)followed emissions from both ions S and A. (The upward and the downward line arrows show absorption and emission of photon respectively and the curvy line arrow represents non-radiative relaxation) [30]

The quantum cutting of a high energy photon by a single rare-earth ion is also known as photon cascade emission (PCE) as shown in Figure 1.7(a). Initially quantum cutting was found experimentally in single ions such as Pr [29, 31],

Tm [32], and Gd [33]. Downconversion between two rare-earth ions can occur via several pathways as shown in Figure 1.7(b-d). For all three mechanisms ion (S) is first excited into a high energy level. Figure 1.7(b) shows the emission of two photons via cross-relaxation between ions S and A followed by energy transfer from ion S to A, and the emission from ion A. In Figure 1.7(c, d), mechanisms showing energy transfer one step between ions S and A, and emission of a photon by both ions.

The downconversion process of the type in Figure 1.7(b) has been demonstrated for the system $LiGdF_4$: Eu^{3+}. Upon VUV excitation (202 nm) in the ^6G_J levels of the Gd ions, the energy is transferred to two Eu ions in two energy transfer steps resulting in emission, around 612 nm, with an internal quantum efficiency (IQE) of about 190% [23, 34]. Internal quantum efficiency refers to the efficiency for the photons which are absorbed by the Gd ions. The external quantum efficiency of the system is much lower, because of the weak absorption of the ^6G_J levels of the Gd ion and thus a significant part of the VUV light is not absorbed by Gd but instead by the $LiGdF_4$ host and lost non-radiatively. The experimental investigation of the $LiGdF_4$: Eu^{3+} system showed an overall quantum efficiency of 32% [35].

Another example of quantum cutting through downconversion involves $LiGdF_4$: (Er^{3+}, Tb^{3+}) with an internal quantum efficiency of 110% [36]. This system involves VUV absorption (167 nm) in Er^{3+} ion, followed by cross-relaxation with Gd^{3+} ion. Subsequently Gd^{3+} transfers its energy to the Tb^{3+} ion resulting in green emission around wavelength of 550 nm. The high absorption strength of the Er^{3+} (4f to 5d) transition may yield high quantum efficiency but this has not been found experimentally.

The first experimental evidence of NIR quantum cutting was found in Tb^{3+}-Yb^{3+} co-doped (Y, Yb)PO_4: Tb^{3+} [37]. In this system, efficient energy transfer was observed when the Tb^{3+} ion was excited into the $^5D_4$ level (~ 490 nm) as shown in Figure 1.8, thereby exciting two nearby Yb^{3+} ions. This energy transfer was based on a cooperative mechanism, where time resolved luminescence measurements were compared with simulations based on theories of phonon assisted, cooperative, and accretive energy transfer. The overall NIR quantum cutting efficiency for this system was found to be 188%.

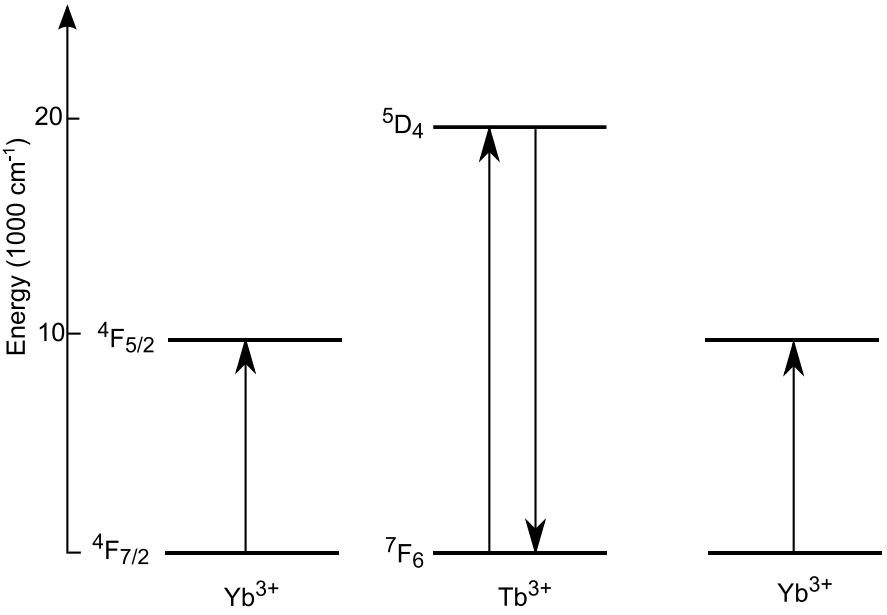

Figure 1.8: Schematic representation of cooperative quantum cutting in a Tb^{3+}-Yb^{3+} system whereby radiative emission from Tb^{3+} ion excites two Yb^{3+} ions simultaneously.

Other reports of efficient quantum cutting in different rare-earth ion systems have been published for Tm–Yb [38, 39], Tb-Yb [40, 41] and Pr–Yb [40-43]. The measured values of QC efficiencies for few of these systems are listed in Table 1.1. In all these reports, QC efficiencies were determined following the

formalism developed by Vergeer et al. [37]. However, this method of estimating the quantum efficiency does not account for concentration quenching effects. The actual NIR quantum cutting efficiency will always be lower and more work is required to determine actual or absolute value of quantum efficiency.

Table 1.1: Values of QC efficiency in different systems.

System (In glass hosts)	Excitation wavelength	QC efficiency (950 nm — 1100 nm)	Reference
Tm-Yb	467 nm	187%	[38]
Tb-Yb	489 nm	179%	[40]
Pr-Yb	482 nm	194%	[42]

1.5 State-of-the-art work

To date, luminescence properties are being exploited in various crystal materials for applications to commercial lighting devices. There has been considerable improvement in the manufacturing of efficient and robust light sources of various sizes. This has been achieved by modifying the spectral content of the emitted light spectrum, particularly from short to longer wavelengths such as in fluorescent and LED lighting.

The research work so far summarised in the preceding section indicates that the spectral conversion of vacuum ultraviolet (VUV) to visible (Vis) light through downconversion is not useful for solar cell application since VUV excitation wavelengths are not present in the terrestrial solar spectrum. However, the spectral conversion from ultraviolet through visible (UV/Vis) to near-infrared (NIR) is promising for improving silicon solar cell efficiency. In a large body of research

work for quantum cutting reported so far, mostly monochromatic light was employed for the excitation purposes. The quantum efficiencies of different conversion materials were determined from the measured luminescence decay curves and the life time measurements. Finally there has been no profound increase in the practical efficiency of the silicon solar cells using downconversion scheme to date due to mostly narrow band absorption of the materials used. An examination of the periodic table shows that rare-earth ions, possessing numerous energy levels and ability to luminesce, may be suitable candidates for modifying the wavelength of sunlight photons. Of all rare-earth ions, the ytterbium (Yb) ion is unique to be used as an activator since it has only two energy levels with emission from an upper energy level around 1.1 eV (~ 1100 nm) but the issue of broad absorption of incident light remains to be addressed.

1.6 General requirements of an optical downconverter

To meet the criteria for application to silicon solar cells, the following conditions must be fulfilled by the downconverter:

- Maximum absorption of the short-wavelength part of the solar spectrum (300 nm ≤ λ ≤ 550 nm).
- Efficient emission of light in close proximity to spectral wavelength (i.e. λ ≤1100 nm) where Si solar cells show maximum response.
- High transmittance of the spectrally shifted photons.
- High fluorescence quantum efficiency.

It is expected that these properties can be achieved by the incorporation of optical dopants (or species) in transparent host materials or matrices. These

optical dopants, with special properties, have different energy levels within the band-gap of host material, which results in the absorption and emission of light thereby resulting in spectrally converted photons. These various optical properties of a luminescent downconverter are investigated and will be described in Chapter 2.

1.7 Objectives of this work

The overall goal of this research was to explore the possibilities of improving Si solar cells efficiency, with a particular emphasis given to study the downconversion of incident solar light. In this pursuit, a downconverter is studied that converts on high energy photon into two or more low energy photons. The primary objective of this work is to use the UV to blue wavelength photons that can result in two photons in the NIR wavelength range that, in turn, can be absorbed by the Si solar cell. Along with this objective, listed below are the sub-goals that comprise this work:

i) To study the photon conversion process for improving Si solar cells.
ii) Study the configurational design of new PV device that consists of a downconverter coupled with a Si solar cell.
iii) Try to identify efficient conversion materials to be used in the downconverter.
iv) Establish an experimental technique to study the fluorescence efficiency of a downconverter.
v) Search for advanced materials that possess wide absorption band.

The way we addressed the problem was to begin with a well known materials (such as erbium and ytterbium) in the literature for solar cells application [23]. This experimental study leads us to understand the science behind a downconverter and provided insightful results through optical characteristics. Next we develop an approach to determine fluorescence quantum efficiency of glassy materials. Further to this we use results of preliminary experiment to explore advanced materials possessing wide absorption in UV to blue region of the solar spectrum. Finally we conclude with the results of initial experiment on cerium doped samples.

1.8 Thesis overview

This thesis describes the fabrication and characterization of an optical downconverter as outlined in Section 1.6, while addressing its requirements for photovoltaic applications.

This research is intended to study systematically the possibilities by exploring different energy materials to enhance solar cell efficiency. This is investigated by studying downconversion process. We have summarized the state-of-the-art work and then develop an experimental technique suitable for the investigation of the energy conversion materials. Further to this, initial materials will be examined using the designed approach. The overview of the work presented in the following three chapters is summarized below.

Chapter 2 is devoted to the experimental investigation performed on the downconverter, together with the data analysis and the discussion of the

preliminary results. Thorough experimental description and procedure for measuring fluorescence spectra and fluorescence quantum efficiency are presented. Detailed quantitative measurements are required necessarily to assess material suitability for its use at practical level.

Chapter 3 concerns with the evaluation of advanced materials that may provide possibility to obtain broad absorption of UV/blue light and efficient luminescence. Their basic structure and optical characteristics are discussed. Finally, initial experiment on cerium doped tellurite glasses is described. The suitability of cerium will be explored through results of initial experiment.

Chapter 4 concludes with the overall summary of the present work together with the future research directions. Finally, appendices provide the supporting information on the relevant sections described in the present and forthcoming chapters where indicated.

Chapter 2

Downconversion in Er/Yb Embedded Te Glass

- Introduction
- Objective
- Choice of host and doping ions
- Fabrication procedure
- Absorption measurements
- Measurement of fluorescence spectra
- Fluorescence quantum efficiency
- Summary of the chapter

This chapter describes the experimental work carried out on a preliminary downconverter made of Er/Yb co-doped tellurite glass. In order to evaluate the optical downconverter, different optical properties such as absorption and fluorescence spectra are explored. A detailed description of the optical materials used and the experimental design is presented, with special emphasis placed on the developed experimental method to determine the fluorescence quantum efficiency. The sections overlap somewhat as different experiments may use part of the same equipment.

2.1 Introduction

The research contained within this thesis is aimed at developing and characterizing downconverters which can potentially be applied to silicon solar cells. In order to fully characterize a downconverter, three optical properties are required to be measured: (i) the absorption spectrum, (ii) the fluorescence spectrum, and (iii) the fluorescence quantum efficiency.

This study deals with the energy conversion materials and classifies them into two components. One of the components is the host material and other is the doping species. The combination of these two components is necessary for developing a downconverter. In this regard host materials serve as basis to which doping species are embedded to obtain luminescence, therefore the selection of the proper host material is crucial. There are different kinds of host materials e.g., phosphors, polymers and oxide based glasses. Of all these, glass materials have best optical and physical properties (see Section 2.3). Glass can be molded and shaped into small or large pieces or even in the form of thin sheets with far greater ease than crystals. Thus, glass is of particular interest, and is considered as a host material. In contrast, crystal materials, such as phosphors, limit near-infrared emission due to adverse light scattering. Based on these key points, we chose glass as a preferred initial host for use in the fabrication of a downconverter.

Within the scope of this thesis it was not possible to carry out research on a large range of materials due to the time and high cost involved. Instead we focused on developing the concept and techniques required to evaluate the suitable energy conversion materials as well as the preliminary materials chosen. The study in

this chapter will explore the downconversion scheme within rare-earth ions. This initial experimental investigation focuses on the use of rare-earth ions for exploring downconversion luminescence, in particular, between erbium (Er) and ytterbium (Yb) ions. These well known rare-earth ions were embedded in tellurite glasses and their optical properties are studied. Further details on these trivalent rare-earth ions are explained in the Section 2.3.

The work described here is divided into mainly three parts. First we describe the choice of materials, the fabrication procedure and the methodology for characterization of samples. Then we present a detailed description of equipment and experimental techniques to characterize the samples in relevant sections and provide analysis of the experimental data acquired. We describe the experimental approach which has been chosen for the measurement of fluorescence efficiency.

2.2 Objective

The aim of the work in this chapter is to develop and demonstrate experimental techniques for characterizing a spectral downconverter. The downconverters were fabricated using tellurite glass co-doped with Er/Yb ions. Absorption and emission measurements of samples are described in Section 2.5. Then Section 2.6 describes an experimental technique for measuring the fluorescence quantum efficiency together with the data analysis procedure. Finally, Section 2.7 concludes with the experimental results and the overall summary of the chapter.

2.3 Choice of host and doping ions

At the commencement of this project to improve the conversion efficiency of silicon based solar cells, we chose to investigate readily available materials as a preliminary investigation. We thus examined the rare-earth complexes or ions which are also known as lanthanides. The reason for selecting rare-earths from the elemental table is that this group of elements luminesce over a wide range of wavelengths, from the near-infrared through the visible to the ultraviolet region and are thus potentially promising for downconversion. Further the lanthanide 4f (intra) transitions are independent of the local environment of the host [25].

To begin with, two rare-earth ions erbium (Er^{3+}) and ytterbium (Yb^{3+}) are chosen because of their well known energy levels that can potentially be useful in photovoltaic applications. The Er^{3+} ions can absorb the short-wavelength part of solar spectrum and fluoresce at longer wavelengths. The Yb^{3+} ions fluoresce in the near-infrared wavelength range where Si solar cells exhibit maximum response.

2.3.1 Er and Yb ion energy level diagram

A simplified representation of the energy level diagram for both erbium (Er^{3+}) and ytterbium (Yb^{3+}) is shown in Figure 2.1. The energy levels are designated with their corresponding spectroscopic (Russell-Saunders) notations [44].

Er^{3+} has higher energy levels in the ladder form with roughly equal spacings which allow possible transitions suitable for the downconversion process. In addition, the transitions from the excited levels of Er^{3+} overlap with the UV and

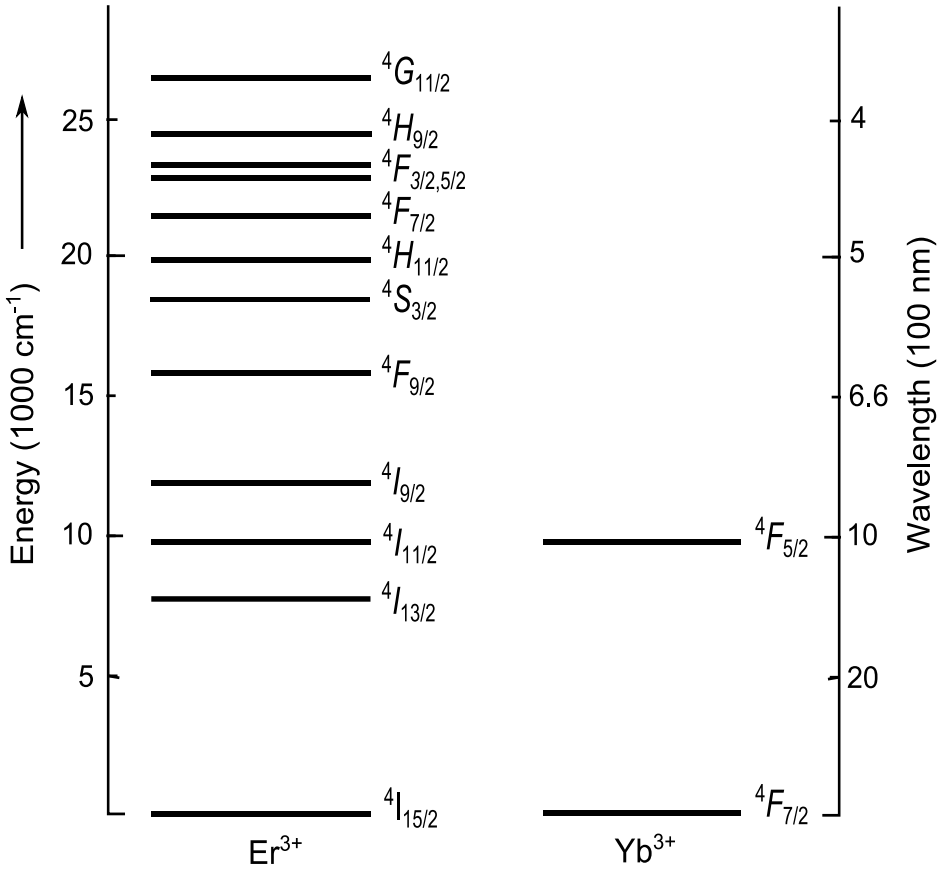

Figure 2.1: Schematic energy level diagram of Er^{3+} and Yb^{3+} ions. (Energy levels are designated with their corresponding notations) [44]

visible regions of the solar spectrum. The choice of Yb^{3+} is based on the following considerations: Yb^{3+} ion has a single excited level ($^4F_{5/2}$) approximately 10000 cm^{-1} above the ground level ($^4F_{7/2}$) as shown in Figure 2.1. Further the absence of other energy levels permits Yb^{3+} ions to absorb photons of 10000 cm^{-1} (~1000 nm) exclusively from other co-doped lanthanide ions and re-emit at a wavelength of about 1000 nm.

Now moving on to the search of the initial host material, tellurite glass was chosen primarily due to both its properties and the availability from an in-house glass fabrication facility. Among the numerous glass hosts, tellurite glass is

particularly interesting, scientifically and technologically, because of its attractive physical properties, some of which include high glass stability, high refractive indices and wide transmission wavelength range, larger rare-earth ion solubility and relatively low phonon energy. Lower phonon energies are an important attribute for minimising non-radiative losses [45]. A comparison of the selected properties of tellurite and silica glass is presented in Table 2.1 [46].

Table 2.1: Optical and physical properties comparison between tellurite and silica glass.

Properties	**Tellurite glass**	**Silica glass**
Optical properties		
Refractive index (n)	1.9 – 2.3	1.46
Transmission range (nm)	400 – 5000	200 – 2500
Highest phonon energy (cm^{-1})	800	1000
Band-gap (eV)	~ 3	~ 10
Physical properties		
Glass transition temperature (^oC)	300	1000
Density (gcm^{-3})	5.5	2.2
Thermal expansion ($\times 10^{-7o}C^{-1}$)	120 – 170	5
Dielectric constant (Ɛ)	13 – 35	4

These properties of tellurite glass are favourable in the design of high optical quality fibres, fibre lasers, and fibre amplifiers [46]. Therefore, its properties can be tailored for the light absorption into the photovoltaic solar cells.

2.4 Fabrication procedure

To observe the luminescence of various transitions of lanthanide ions in the glass based host through optical study, we fabricated luminescent samples by doping Er and Yb ions in tellurite glass. Glass preparation was performed through conventional melt and quench procedures [47]. In the present study, glasses were melted using gold crucibles at a temperature of 900°C in furnace and casting was performed in rectangular brass molds. Then, the annealing furnace was turned off to allow the glass samples to cool down to room temperature. Finally, thin samples were made from the blocks of glass for optical measurements. A detailed description of glass fabrication process is presented in earlier work [48].

The Er^{3+} concentration was chosen to be low between 0.2×10^{20} ions/cm^3 and 1×10^{20} ions/cm^3 to minimize energy migration among Er^{3+} ions and the Yb^{3+} concentration was chosen as 9×10^{20} ions/cm^3 and 9.8×10^{20} ions/cm^3 in order to achieve maximum energy transfer from erbium ions [47]. It is pertinent to mention that energy transfer is essential for near infra-red luminescence in the longer wavelength range as discussed in Chapter 1. The Er doped and Er/Yb co-doped tellurite glasses were characterized by optical measurements of absorption and fluorescence emission spectra.

2.5 Optical characterization

Different spectrophotometers and spectrofluorometers were used to measure the optical properties of the host tellurite glass and the dopants. As noted in the introduction to this chapter; absorption and emission spectra were measured.

Moreover, a separate experiment was designed to determine fluorescence quantum efficiency of the samples. Each measurement and experimental results are presented with an explanation of the relevant underlying physics followed by a detailed description of the experimental technique and results obtained.

2.5.1 Absorption measurement

Absorption measurements were performed using a UV/Vis/NIR spectrophotometer (Cary 5000). This is a dual beam instrument capable of measuring absorption and transmission over the wavelength range from 200 nm to 3300 nm. It is equipped with deuterium and tungsten lamps as excitation sources and the detectors used are made of silicon (Si) and indium gallium arsenide (InGaAs). The light from the excitation sources is guided to a monochromator for wavelength selection and scanning. Subsequently, the light is passed through the sample and the transmitted signal is detected. The working principle of the instrument can be found in texts [25, 49]. Although software (Cary WinUV) controlling the device is capable of calculating the “absorption coefficient” directly, it was not initially clear whether it was Decadic or Napierian type (see below). Thus the spectrophotometer was always used in transmission mode to measure the fractional transmission of all luminescent samples and calculations were performed manually to determine an absorption coefficient.

There is often confusion in the literature about the type of absorption coefficient that is being referred to, whether it is of Decadic or Napierian type. Decadic coefficients are based on using the power of 10 in the Beer-Lambert law [50, 51], while Napierian coefficients use the power of *e* instead [52]. To avoid ambiguity, all absorption coefficients in this work are Napierian unless otherwise mentioned.

Thus by measuring the transmission of the glass samples, it is possible to use the Beer-Lambert law directly to calculate the absorption coefficients of single and co-doped samples.

The calibration of the instrument was always performed prior to conducting any absorption measurement. In order to perform a calibration, first hundred percent (100%) transmission spectrum was recorded without a sample in the path of light beam so as to obtain a maximum signal, followed by a zero percent (0%) transmission spectrum by blocking the light beam to obtain the minimum signal of the spectrophotometer. The spectral bandwidth of the spectrophotometer was set to 1 nm through software.

Er doped and Er/Yb co-doped glass samples with different concentrations were used in this study. All doping concentrations are in units of ions/cm^3. The physical characteristics together with designations of samples investigated in this work are listed in Table 2.2. These samples were made from rectangular blocks of glass weighing between 30 gm and 50 gm. The thickness of each sample was 1.0 ± 0.1 mm. All samples were polished before the absorption measurements to avoid surface irregularities that might scatter the light.

The reflection of light from the sample, referred to as Fresnel reflection loss '$R(\lambda)$' [53], was removed by using Equation 2.1. These losses occur due to different refractive index media in the path of beam, such as air and glass.

$$R(\lambda) = \left[\frac{n(\lambda) - 1}{n(\lambda) + 1}\right]^2, \tag{2.1}$$

where 'n(λ)' is the refractive index of the glass and is a function of wavelength. The reflection of light from the sample thus varies with wavelength.

Table 2.2: Physical characteristics of Er/Yb samples used in this study.

Serial No.	**Sample designation**	**Conc. (ions/cm^3)**	**Dopants & Host Comp.**
1	Er0.2	0.2×10^{20}	Er –Te-Zn-Na-La
2	Er1	1×10^{20}	Er –Te-Zn-Na-La
3	Er0.2Yb9.8	0.2×10^{20}, 9.8×10^{20}	(Er, Yb) –Te-Zn-Na-La
4	Er1Yb9	1×10^{20}, 9×10^{20}	(Er , Yb) –Te-Zn-Na-La

To measure the refractive index of tellurite glass we could have measured the values of refractive index of each sample, by using an ellipsometer, at the same wavelengths as was chosen in the sample's transmission measurement within same spectral range. However, this option was not pursued In the present case, we used the well known Sellmeier index relation [54], given by Equation 2.2, to determine refractive index value in the wavelength range from 300 nm to 1100 nm as shown in Figure 2.2. The Sellmeier expression for refractive index '*n*' is

$$n^2 = A + \frac{B}{1 - {C}/{\lambda^2}} + \frac{D}{1 - {E}/{\lambda^2}}, \tag{2.2}$$

where *A, B, C, D and E* are Sellmeier coefficients and λ is the wavelength. In the case of tellurite glass, the used values are A= 2.42489, B= 1.5004, C= 0.0525775, D= 2.32884, and E= 225, taken from reference [54].

The refractive index curve was used with the experiment data later to compensate for reflection losses. Any remaining loss observed is ascribed to the scattering of light from the impurities (such as metal ions or crystals) or bubbles present in the glass. These impurities may have been produced during the glass

fabrication process. Finally, an absorption coefficient 'α(λ)' of all samples was calculated using the Beer-Lambert law [50,51].

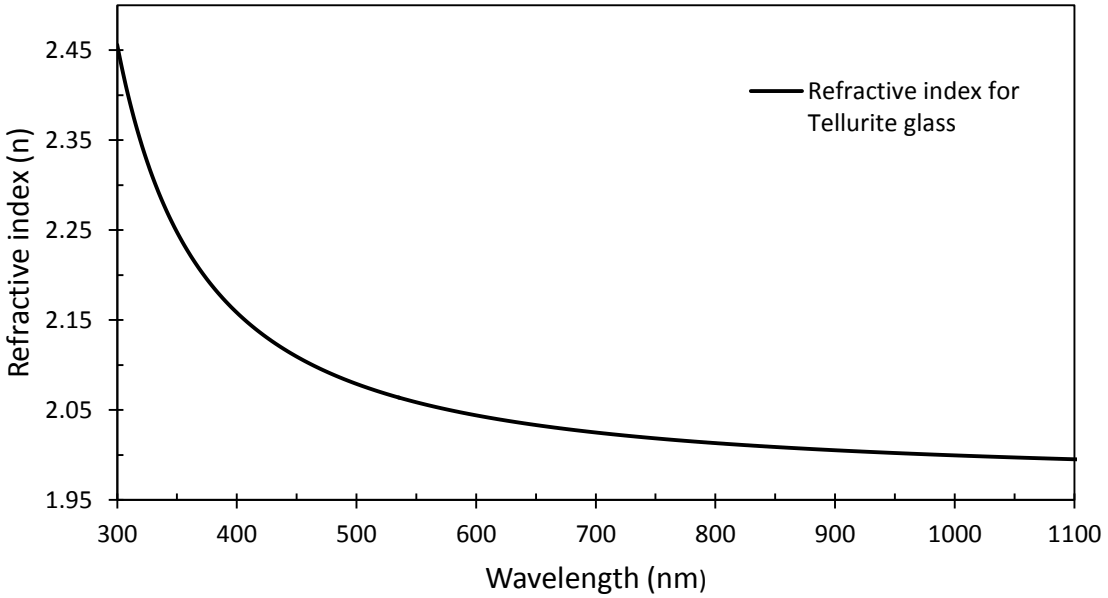

Figure 2.2: The calculated refractive index curve for tellurite glass.

Let I_o and $I(\lambda)$ be the intensity of incident and transmitted light through a medium of thickness 'd', then

$$I(\lambda) = I_o\, e^{-\alpha(\lambda)d}. \tag{2.3}$$

After reflections from the front and rear interface of a medium or sample, the transmission will be

$$T(\lambda) = \frac{I(\lambda)}{I_0} = (1-R)^2 e^{-\alpha(\lambda)d}. \tag{2.4}$$

Using Equations 2.3 and 2.4, we find:

$$\alpha(\lambda) = -\frac{1}{d}\ln\left[\frac{T(\lambda)}{(1-R)^2}\right], \tag{2.5}$$

where T is the transmission light, R is the reflection of light, d is the sample thickness and λ is the wavelength. The absorption coefficient thus depends on

the nature of a medium and is measured in units of per millimetre (mm^{-1}) in the present work.

The absorption coefficient of different samples is plotted over the wavelength range from 350 nm to 1100 nm as shown in Figure 2.3(a) and (b). All these measurements were performed at room temperature.

For comparison of results, the absorption spectrum of un-doped tellurite glass is measured and plotted separately as shown in Figure 2.3(a). Further, the absorption spectra of Er/Yb co-doped tellurite glass samples are shown in Figure 2.3(b). These measured results are comparable to earlier reported work [55] which shows similar spectral transitions around peak wavelengths. Several absorption features of the samples can be seen from the present absorption spectra such as transparency and absorption peaks caused by doped optical ions etc. In Figures 2.3(a) and (b), the small distortion around 800 nm corresponds to an instrument artefact due to detector changeover.

One of the fundamental features of the glass samples is the wavelength range over which they are transparent as can be seen in Figure 2.3, from the near-UV, through visible to NIR region for incident light. Additionally, the sharp increase of absorption coefficient around 350 nm represents intrinsic ultraviolet absorption due to electronic vibrations. This intrinsic absorption could be due to the Rayleigh scattering exhibiting a wavelength dependence of ~ λ^{-4} [56]. Rayleigh scattering is caused by the local structural fluctuations such as density and concentration fluctuations.

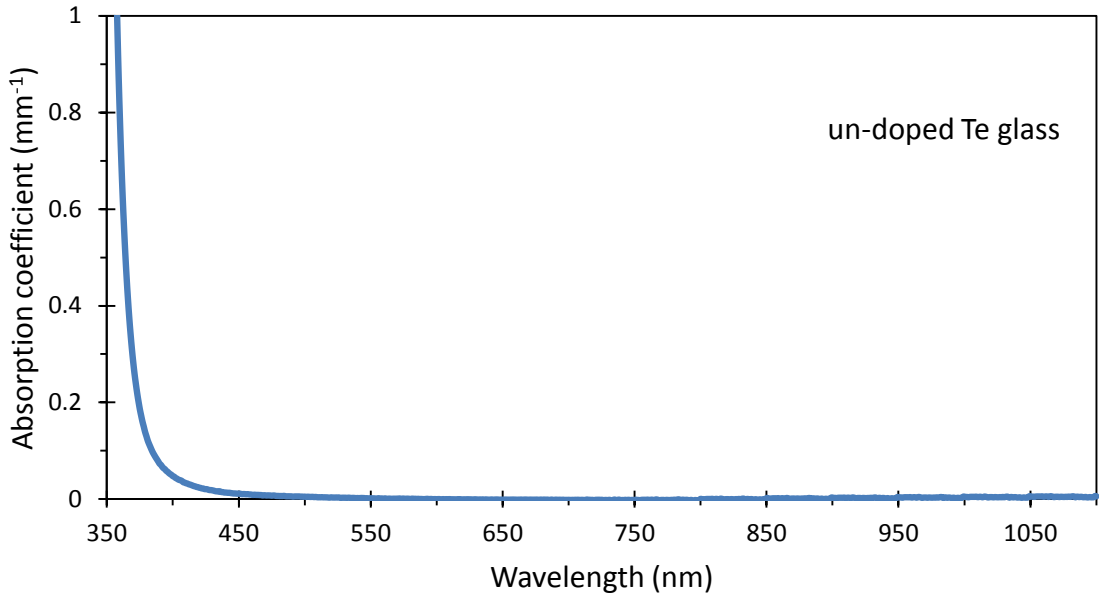

(a)

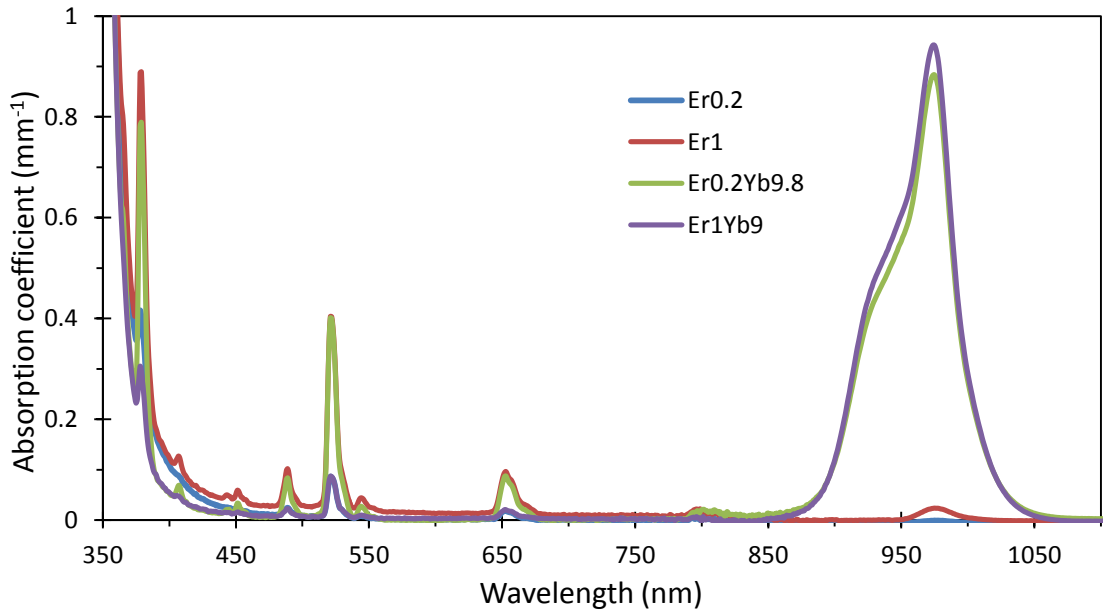

(b)

Figure 2.3: (a) Optical absorption spectrum for (a) un-doped Te glass, and (b) Er/Yb co-doped Te glasses. (Absorption peaks are tabulated in Table 2.3)

Further, Er^{+3} ions show a series of spectral absorption bands in the wavelength range from 350 nm to 550 nm which overlap with the high energy portion of the solar spectrum. The peak wavelengths of all absorption bands are assigned according to the energy levels diagram shown in Figure 2.1. The peak values of absorption bands along with spectral transitions are listed in Table 2.3.

Table 2.3: Spectral transitions with their corresponding peak wavelengths.

Spectral Transitions	**Peak Wavelengths (nm)**
$^4I_{15/2}$-$^4G_{11/2}$	379 nm
$^4I_{15/2}$-$^2H_{9/2}$	405 nm
$^4I_{15/2}$-($^4F_{3/2}$, $^4F_{5/2}$)	450 nm
$^4I_{15/2}$-$^4F_{7/2}$	488 nm
$^4I_{15/2}$-$^4H_{11/2}$	525 nm
$^4I_{15/2}$-$^4S_{3/2}$	550 nm
$^4I_{15/2}$-$^4F_{9/2}$	660 nm
$^4I_{15/2}$-$^4I_{11/2}$	980 nm

From Figure 2.3b, it can be also noticed that relatively wide (~ 1000 nm) and narrow (~ 980 nm) bands corresponds to the transitions of Yb^{3+} ions ($^2F_{7/2}$-$^2F_{5/2}$) and Er^{3+} ions ($^4I_{15/2}$-$^4I_{11/2}$) respectively. The transition around 1000nm indicates the ability of Yb^{3+} ions to serve as acceptor for energy transfer from excited Er^{3+} ions. Additionally, Yb^{3+} ions emission band around near-infrared wavelength corresponds to the energy band-gap of the Si solar cell (see Figure 1.1).

2.5.2 Measurement of fluorescence spectra

Initially a commercial spectrofluorometer was used to measure the fluorescence emission spectra of different samples[3]. During the course of the measurement, a new experiment design was built on the optical table where different light sources together with the available optics were used, according to the experiment requirement, with an optical spectrometer in order to acquire emission spectra.

The response to the excitation wavelength of the optical properties (fluorescence spectrum and fluorescence quantum efficiency) of a downconverter containing luminescent species was studied. The fluorescence spectra were measured using excitations in the wavelength range from 350 nm to 550 nm by employing broadband blue and UV light emitting diodes. The detailed specifications of both LEDS are provided in Appendix B. Excitation below the wavelength of 350 nm was limited due to the intrinsic absorption of light by the host glass. Fluorescent samples were excited with different excitation sources corresponding to measured absorption peaks (see Section 2.5.1).

The samples used were the same as described in Section 2.5.1. Emission of light from samples was collected with a lens and guided to the commercial spectrometer (SpectraPro 2300i, Princeton Instruments) with the help of an optical fibre bundle (ARC-LG-455-020-3). The light signal was dispersed by a diffraction grating blazed at 500 nm inside the spectrometer. This dispersed light was detected using a silicon charge-coupled detector (Acton Research Corp., SI-440). Different edge filters (or long-pass filters) were used to block the excitation light reaching the detector to prevent saturation. A schematic diagram of the optical

[3] The reason for using this instrument here is to take quick measurements.

layout of the experiment is illustrated in Figure 2.4. The spectra were obtained after the wavelength calibration of the spectrometer with the line source (Acton Research Corp., Model: USB-Hg-Ne/Ar). Further details of spectral calibration and the line source are provided in Appendix C.

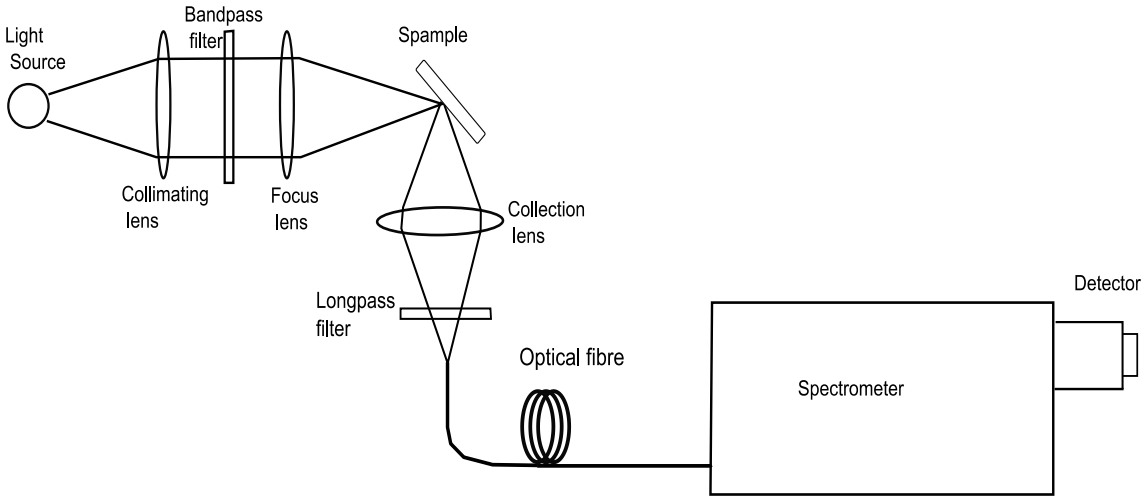

Figure 2.4: Optical layout of fluorescence experiment setup

At the start of each experiment, the fluorescence spectra were measured using an excitation wavelength of 488 nm. The excitation light was obtained by a combination of a band-pass filter (488 nm, Ealing Inc.,) and a blue LED source (Model M455L2, THOR LABS). Different excitation wavelengths were chosen from Er^{3+} ion transitions observed in absorption spectra as explained in Section 2.5.1. To observe optical transitions at longer wavelengths, the fluorescence spectra were recorded in the spectral range from 480 nm to 1100 nm as shown in Figure 2.5. All the emission measurements were carried out at room temperature.

The specifications of the optical spectrometer used in this study are listed in Table 2.4.

Table 2.4: Spectrometer specifications[4] (Model: SpectraPro 2300i)

Optical design	**Focal length**	**Scan range**	**Resolution**	**Sample speed**	**Reproducibility**
Czerny-Turner	300 mm	0 – 1400 nm	0.1 nm @ 435.8 nm	100 nm/min	±0.05 nm

Several emission bands corresponding to Er^{3+} and Yb^{3+} ions can be observed in Figure 2.5, which are attributed to 4f-4f optical transitions as a result of exciting electrons from the ground level to the excited ($^4F_{7/2}$) level of Er^{3+} ion. The electrons de-excite rapidly through non-radiative relaxation by phonon emission to $^4H_{11/2}$ level with subsequent radiative emissions resulting in different spectral bands. The observed spectral bands can be distinguished as visible and near-infrared emissions.

Under the excitation of 488 nm light, a series of visible emission bands centred at 525 nm, 550 nm, and 660 nm can be seen (Figure 2.5), which are assigned to the electronic transitions from excited levels $^4H_{11/2}$, $^4S_{3/2}$, and $^4F_{9/2}$ to the ground level $^4I_{15/2}$ respectively as illustrated in Figure 2.6 which is the schematic energy level diagram with radiative and non-radiative decay for Er^{3+} and Yb^{3+} ions.

[4] Source: User's manual from Acton Research Corporation.

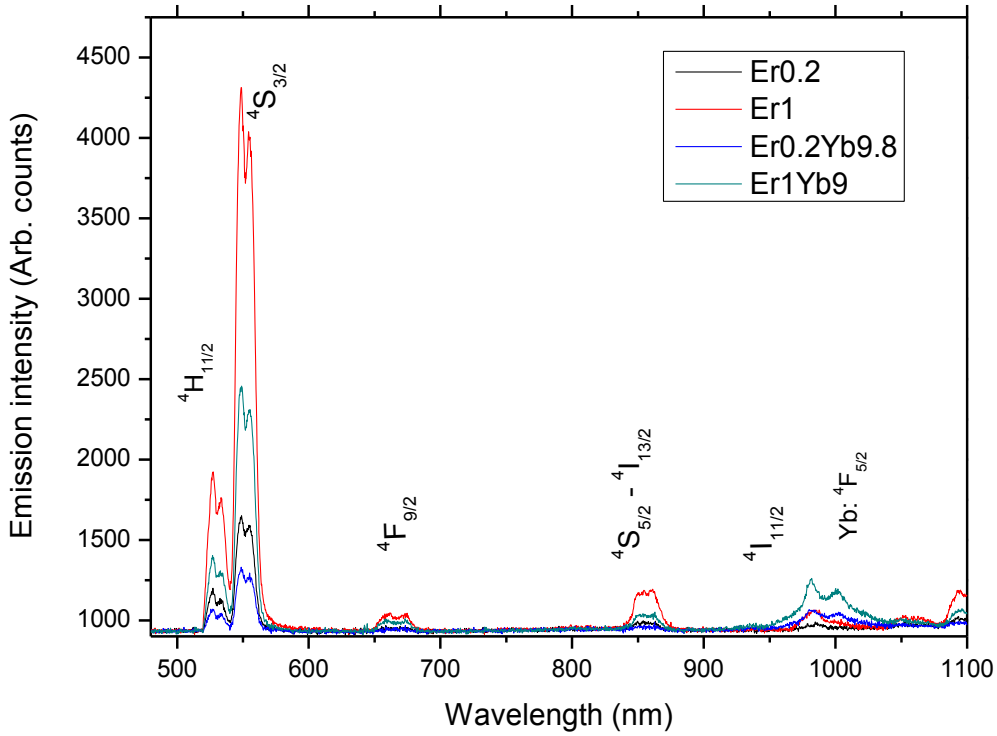

Figure 2.5: Fluorescence spectra of Er/Yb co-doped Te glasses using 488 nm excitation. (Spectroscopic notation denotes the energy levels of Er ions except for Yb ion)

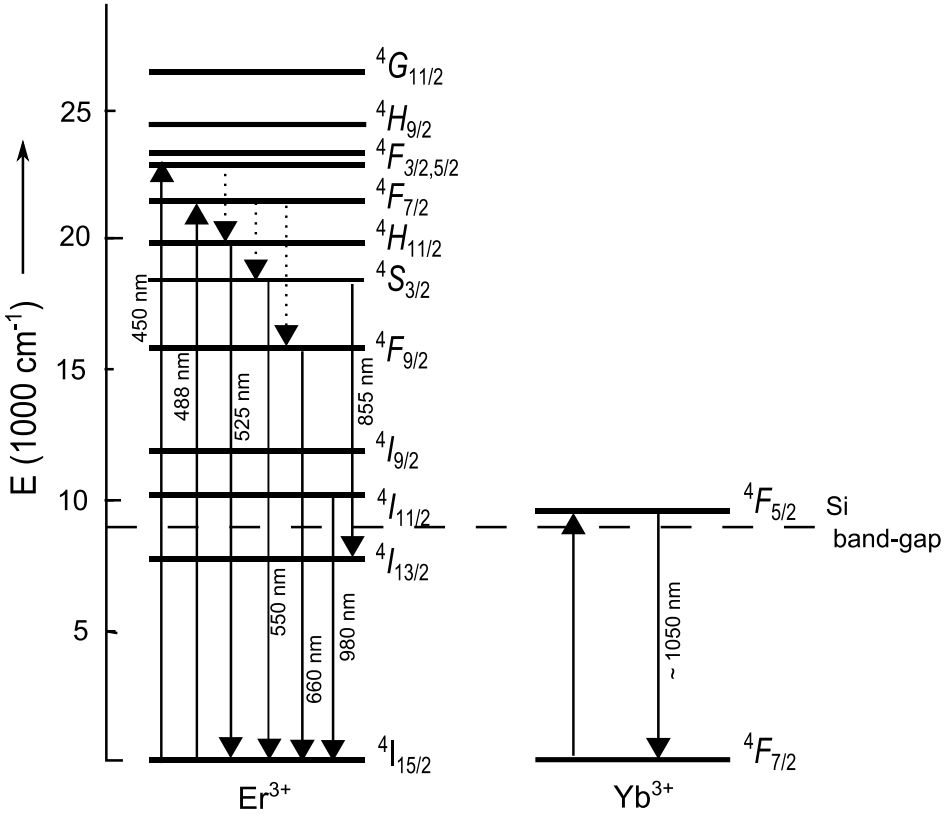

Figure 2.6: Optical transitions from energy levels of Er^{3+} and Yb^{3+} ions with labelled wavelengths. (Up and down arrows show excitations and radiative emissions, respectively, while dotted arrows show non-radiative emissions)

Further looking into the emission spectra (Figure 2.5), the most intense spectral transition thus arises from the $^4S_{3/2}$ level around 550 nm, which indicates that despite the energy gap between $^4F_{7/2}$ and $^4H_{11/2}$ being ~ 1200 cm^{-1}, non-radiative phonon relaxation (NPR) to $^4S_{3/2}$ dominates over a radiative decay. The non-radiative relaxation rate (W_{npr}) strongly depends on host constituents and follows the energy law [57] (i.e. $W_{npr} = \alpha\, e^{-\beta \Delta E}$, where α and β are constants and ΔE is the energy gap between the 4f energy levels of the rare-earth ions).

In the near-infrared range, the spectral band around 850 nm is ascribed to $^4S_{3/2} \rightarrow {}^4I_{13/2}$ transition [58] in Er^{3+} ion as shown in Figure 2.6. Further broad emission peak around 1000 nm is due to Yb^{3+} ion ($^2F_{5/2}$ level) along with Er^{3+} slight emission ($^4I_{11/2}$ level) near 980 nm is observed. Similar emission transitions have been reported for Er/Yb co-doped $NaYF_4$ previously [59] and it was proposed an inefficient visible to near-infrared downconversion emission because of fast non-radiative relaxation occurring in the Er^{3+} from $^4F_{7/2}$ to $^4S_{3/2}$ energy level, instead of the energy transfer:

$$Er^{3+}\,(^4F_{7/2}) + Yb^{3+}\,(^4I_{15/2}) \longrightarrow Er^{3+}\,(^4I_{11/2}) + Yb^{3+}\,(^2F_{5/2}). \qquad (2.6)$$

The inefficient energy transfer among Er^{3+} and Yb^{3+} ions could be due to the following reasons: first, Er^{3+} ion transitions have a narrow absorption band due to parity and spin forbidden spectroscopic rules, and second, the emitted energy migrates within Er^{3+} ions which is released from Yb^{3+} ions.

For a more rigorous examination of luminescence decays and analysis of downconversion scheme among Er and Yb ions, further emission spectra were acquired, with more energetic photons using an excitation of wavelength 450 nm as shown in Figure 2.7.

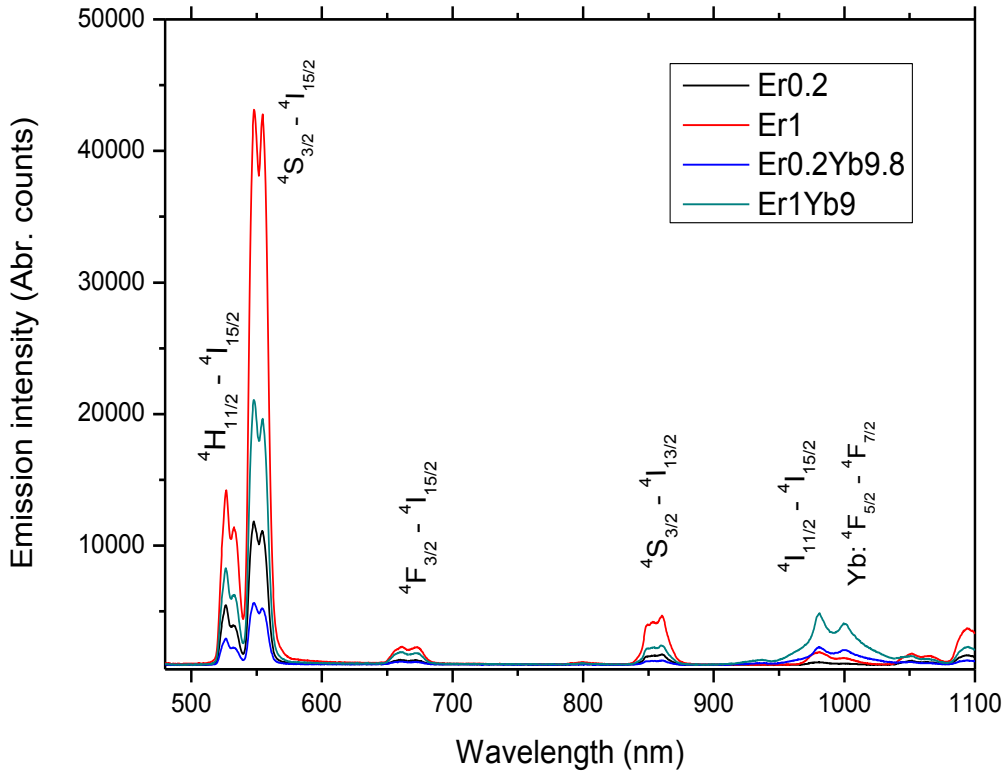

Figure 2.7: Fluorescence spectra of Er/Yb co-doped Te glasses using 450 nm excitation (Spectroscopic notation denotes the energy levels of Er ions except for Yb ions)

The emission spectra were measured under identical conditions and using the same setup, allowing us to make comparisons with those results as previously discussed using the 488 nm excitation.

In this case, the emission spectra were scanned in the wavelength range from 480 nm to 1100 nm as shown in Figure 2.7. A closer examination of the spectra shows that emission bands were observed at the same wavelengths, but with different emission intensity. In the present experiment 4f electrons were excited to the higher energy level ($^4F_{5/2}$) of the Er^{3+} ion in luminescent samples as can be seen in Figure 2.6. After an excitation, electrons rapidly de-excite to level $^4H_{11/2}$ through non-radiative phonon relaxation (NPR) thereby emitting a photon of

wavelength 525 nm as indicated in Figure 2.6. This photon excites two nearby Yb ions simultaneously which may result in emission of two photons in the near-infrared wavelength range of ~ 1050 nm. These emitted photons fall ($\lambda \leq 1.1$ μm) just within the spectral response of the silicon solar cell which may create additional electron-hole pairs thereby enhancing the efficiency.

The results shown in Figure 2.7 indicate inefficient energy transfer which is from $^4F_{9/2}$ level of Er^{3+} ions to the $^4F_{5/2}$ level of Yb^{3+} ions. Based on a rule of thumb, the radiative decay and non-radiative phonon relaxation can compete when the energy gap is less than five times the phonon energy, and that for a larger gap radiative decay dominates [60]. Therefore it can be inferred that $^4S_{3/2}$ and $^4F_{9/2}$ levels of Er^{3+} ions are populated through non-radiative phonon relaxation as shown in Figure 2.6. The decrease in the emission intensity from $^4S_{3/2}$ level for sample Er1 can be attributed to energy transfer when Yb ions are co-doped with Er ions for the sample (Er1Yb9) however it remains inefficient. Further, the present results reveal that the transition from the $^4I_{11/2}$ (Er^{3+}) level has slightly higher peak intensity than intensity of $^4F_{5/2}$ (Yb^{3+}) level which shows limited emission from Yb^{3+} ion. Overall these results suggest that the conversion of blue photons to NIR photons is weak which is not very useful for solar cells application.

2.6 Fluorescence quantum efficiency

The most important characterization of a solar downconverter is the quantitative measurement of a parameter referred to as “fluorescence quantum efficiency”

(abbreviated as FQE). This parameter plays a vital role in determining the practical suitability of a downconverter to photovoltaic applications.

The fluorescence quantum efficiency is defined as “the ratio of the number of emitted photons and the number of incident photons” i.e.

$$\eta(\lambda) = \frac{number\ of\ emitted\ photons\ in\ the\ desired\ band}{number\ of\ incident\ photons\ in\ the\ excitation\ band}. \quad (2.7)$$

Some authors use the ratio of the energy released and the energy incident on the sample to determine the quantum efficiency and terms such as “luminescence quantum efficiency” (LQE), “photoluminescence quantum efficiency” (PLQE), and “fluorescence quantum efficiency” (FQE). These different terminologies are used interchangeably in literature [61-63]. In this work we use Equation 2.7 to measure FQE “$\eta(\lambda)$”.

In order to measure the efficiency of luminescent samples we need a method capable of measuring reliable values of quantum efficiency. Experimental methods for the measurement of quantum efficiencies were reviewed comprehensively by Demos and Crosby [64]. Samples used in these methods were in the liquid phase. These methods are based on the comparison of the fluorescence sample with a fluorescence standard to measure quantum efficiency. However, even after further improvements to these comparison methods, different values of quantum efficiency of same samples were found. For calibration purposes, a known light source was used always to correct instrumental response of the system whose response varies from one instrument to the other. Some researchers have used other methods namely an integrating sphere [65] and thermal lens effect [66]. We only discuss method based on integrating sphere and subsequently explain our experimental approach.

The use of an integrating sphere for quantum efficiency measurement was first discussed by DeMello [65]. The method was used to study quantum yield of polymer samples. This procedure was further investigated by Pälsson [67]. In this approach, an integrating sphere was used in conjunction with a commercial spectrometer and a detector. The measurement of emission was performed in two steps. First, the emission was measured with empty integrating sphere and then emission was recorded with the sample inside integrating sphere. Subsequent data analysis was performed to calculate the quantum efficiency value. However, this experimental method has a number of drawbacks. First, the geometry of the sample will tend to obscure or reabsorb some of the fluorescence. Second, baffles employed inside integrating sphere reduce the fluorescence signal before reaching to the CCD. Third, the signal is not equal to the total sample's emission, and only represents a proportion of emission for a given sample geometry. Finally, an inner surface of the sphere should be highly diffusive reflective for the better utilization of this method. In addition to this, a fluorescence standard is used for the accurate calibration of the throughput of the sphere.

Quantitative measurement of fluorescence efficiency of solid samples is complex owing to difficulty in measuring emission, transmission and absorption; however, it is essential to determine for practical use. We have developed an experimental set-up which is simple, rapid, and accurate and characterized luminescent samples containing Er and Yb ions to measure quantum efficiency. This method utilizes a commercial spectrometer and readily available optics. Our method has several benefits, as pointed out below, over the experimental approach discussed above.

Our experimental technique:

i) generates overlap between pump and fluorescence volume,

ii) the total fluorescence, in illuminated solid angle and the detected, independent of sample geometry, and

iii) is self calibrating in principle, however it can be calibrated by using un-doped samples or by choosing incident wavelength away from the sample's absorption band.

The objective of this part of work is to explain and investigate the potential utility of this experimental technique.

2.6.1 Experimental setup

We used the setup shown schematically in Figure 2.8 to measure fluorescence quantum efficiency. The validation of our experimental technique is provided in Appendix D. A light emitting diode was employed as a pump source to excite the samples containing rare-earth ions. The excitation wavelength was chosen from the absorption spectrum at the peak value of a transition ($^4G_{11/2}$) in the near ultra-violet range as shown in Figure 2.3(b). The incident light from pump was collimated and focused on to the sample. Subsequently emission from the sample was directed to the spectrometer. An optical spectrometer (Princeton Instruments, Model SP-2300*i*) equipped with an air cooled charge-coupled device (CCD, Model PIXIS 256BR) was employed to record the fluorescence signal.

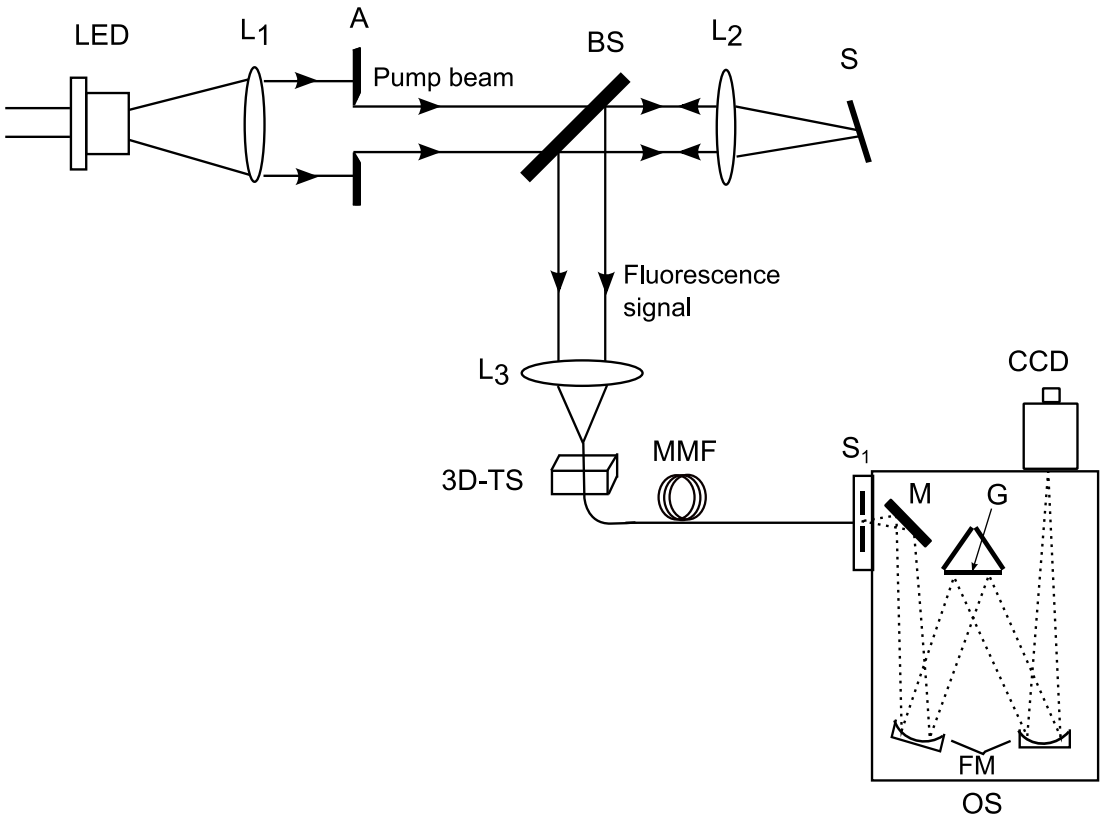

Figure 2.8: Schematic representation of an experimental setup used for determining the fluorescence quantum efficiency.

Legend: LED (Light emitting diode), L_1 (Collimating lens), A (Aperture), BS (Beam splitter), L_2 (Focusing lens), S (Sample), L_3 (Collection lens), 3D-TS (XYZ translation stage), MMF (Multimode optical fibre), S_1 (Slit), M (Mirror), FM (Focusing mirror), G (Grating), CCD (Charge-coupled detector) and OS (Optical spectrometer)

A major challenge in measuring the fluorescence quantum efficiency of solid samples is the presence of impurities within the sample. This causes scattering of both the incident beam and the fluorescence. In our approach, a broadband UV LED of centred wavelength 379 nm (Model 380L, THOR LABS) with bandwidth of 12 nm was used to represent the UV component of the solar spectrum. The excitation beam is focused on a sample under study with the aid of collimating and focusing lens as shown in Figure 2.8. An aperture (with varying diameter) is placed between these two lenses to control the solid angle of the incident light by adjusting the diameter of an aperture. The size of aperture was decreased until controlled output was observed at the CCD detector. While decreasing the diameter of an aperture, the emitted light (of sample) was coupled into the optical fibre bundle (19 fibres, each has diameter of 200 μm without cladding) mounted on a XYZ translation stage as shown in Figure 2.8.This way the size of aperture matched with the acceptance angle of the spectrometer.

In the thesis, bulk samples used were made of tellurite glass. Both sides of samples were cleaned with acetone prior to taking measurements. A sample was held using a small clip in the path of the excitation beam in a tilted position (angle ~ 10°) to prevent specular reflection reaching the detector and to avoid interference with fluorescence signal (see Figure 2.9).

Our experimental setup was designed in such a way that it ensures accurate overlap of the volume being illuminated to that being probed for fluorescence (see Figure 2.9). This means that the fluorescence observed should be directly proportional to the illumination absorbed; both of which are measureable as shown in Figure 2.8. The beam splitter (BS) was used to separate the fluorescence signal from the incident beam and directed to the collection lens.

The collection lens (L_3) was mounted on an L-shaped bracket attached to a translation stage while an optical fibre bundle was held on a XYZ translation stage (see Figure 2.8).

A long-pass filter can be inserted between sample and collection lens to distinguish excitation and the emission of a sample. However, using the long-pass filter reduces the strength of measurable light signal. Furthermore, it was difficult to measure any sample for which the luminescence is comparable to the filter fluorescence. It is for this reason no long-pass filters were used in this experiment. We used various neutral density filters of different optical densities (ODs). They were used in front of the collection lens to check the linearity of the experimental setup over a long wavelength range. Further the fluorescence signal in illuminated solid angle was focused onto the optical fibre bundle which was held using SMA905 connector and the emitted light was guided to the spectrometer where light is dispersed by a diffraction grating (1200 grooves/mm blazed at 500 nm) and the final signal was recorded on the CCD detector. Finally the spectrometer was controlled by custom software (WinSpec 32) to observe the features of emitted light. This method provides a simple and rapid estimation of fluorescence quantum efficiency.

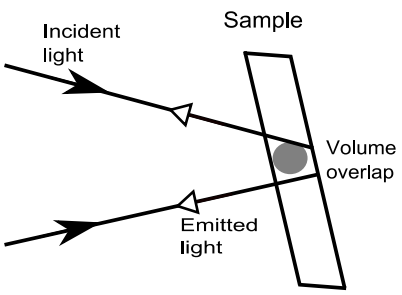

Figure 2.9: Side cross-sectional view of sample showing overlap between pump and the fluorescence. (A circle inside sample represents volume)

2.6.2 Procedure and data analysis

Using the experimental setup drawn schematically in Figure 2.8, measurements were performed following a procedure consisting of two simple steps: the emission spectrum was measured first with the sample in place and then without the sample in the holder. Subsequently optical power was measured for each step and data was acquired. The measured emitted power was proportional to the signal recorded at the detector. Both measurements were performed under identical experimental conditions. The spectrum measured without a sample serves as a background spectrum which accounts for both dark counts detection and the reflection of pump light from the optics employed in the experimental setup. The above experimental steps were performed in a dark room to avoid stray light.

An alternative way is to use an un-doped sample to measure the spectrum which serves as background and then subtract it from the fluorescence spectrum measured using the doped sample. However, this was not used due to the presence of different amount of impurities even if both samples were prepared under identical conditions.

The data analysis was performed by determining the area under peaks of measured emission spectra. The area under the curve of a sample fluorescence spectrum is proportional to the amount of light emitted and scattered from the sample. The area of the spectrum recorded without a sample is proportional to the background (or loss). Finally we obtained difference fluorescence spectrum (of a sample) by subtracting a spectrum recorded without sample from the fluorescence spectrum recorded with the sample placed in the path of incident

light beam. Thus, an area under the curve of difference fluorescence spectrum of a sample away from the excitation peak is proportional to the amount of light emitted by the sample. Next calculations were performed manually to determine the fluorescence efficiency '$\eta(\lambda)$' using Equation 2.9. Detailed calculations for a sample are presented in Appendix E. The incident beam power was measured at the sample place and emitted light power was measured at the input of the optical fibre by using an optical power meter (Newport Corp., Model: 2936-C) equipped with a detector (Newport Corp., Model: 918D-UV-OD3). Since a single detector is used while measuring powers so it response effect cancels out eventually when we take the ratio as will become evident below. Then we developed a simple mathematical Equation 2.8, as given below, to determine the fluorescence power emitted by the sample.

$$P_{f'} = \frac{(P_{meas}) \times (Area\ under\ the\ curve\ of\ difference\ fluorescence\ spectrum)}{Total\ area\ under\ the\ curve\ of\ fluorescence\ spectrum}, \qquad (2.8)$$

where 'P_{meas}' is the measured emitted power from the sample and '$P_{f'}$' is the calculated fluorescence power.

In a subsequent step, the total emitted power was calculated by assuming an isotropic emission from a sample. If '$P_{f'}$' is the detected power over a solid angle 'Ω', the total emitted power 'P_f' is given by the expression $P_f = \frac{P_{f'}}{\Omega/4\pi}$, where 'Ω' depends on the geometry of experimental setup and is given by $\Omega = \frac{\pi r^2}{l^2}$ (where 'l' is the distance between sample and the focusing lens and 'r' is the radius of the focusing lens). In our experiment, for given values of l and r (see Appendix E), the collected solid angle is then 2.27×10^{-2}. Finally, the fluorescence efficiency was calculated using Equation 2.9:

$$\eta(\lambda) = \frac{P_f(\Delta\lambda)}{P_i(\lambda)}, \tag{2.9}$$

where 'P_f' is the total amount of power emitted by the sample in the spectral range of interest and 'P_i' is the amount of incident power from the excitation light source.

Using UV excitation (379 nm), fluorescence spectra of samples were measured for further investigation of emission and efficiency. The fluorescence spectra were recorded in the spectral range from 350 nm to 1100 nm. All the fluorescence measurements were performed at room temperature. The measured fluorescence spectra are plotted in the form of difference fluorescence spectra which was obtained after subtracting the background as discussed above and is shown in Figures 2.10(a) and (b).

For the purpose of comparison, fluorescence spectra of two samples doped with and without Yb ions are plotted separately as shown in Figures 2.10(a) and (b). The concentrations of Er and Yb ions are mentioned in Table 2.1. Samples were excited by pumping Er ions to a level ($^4G_{11/2}$) and subsequent emission was measured. The spectral transitions in the emission spectra are attributed to radiative decays i.e. [$^4H_{11/2}$ - $^4I_{15/2}$], [$^4S_{3/2}$ - $^4I_{15/2}$], [$^4F_{9/2}$ - $^4I_{15/2}$], [$^4S_{3/2}$ - $^4I_{13/2}$], and [$^4I_{11/2}$ - $^4I_{15/2}$] as shown in energy levels diagram (see Figure 2.11). The peaks at 379 nm and 760 nm correspond to the excitation and the second order of source light respectively.

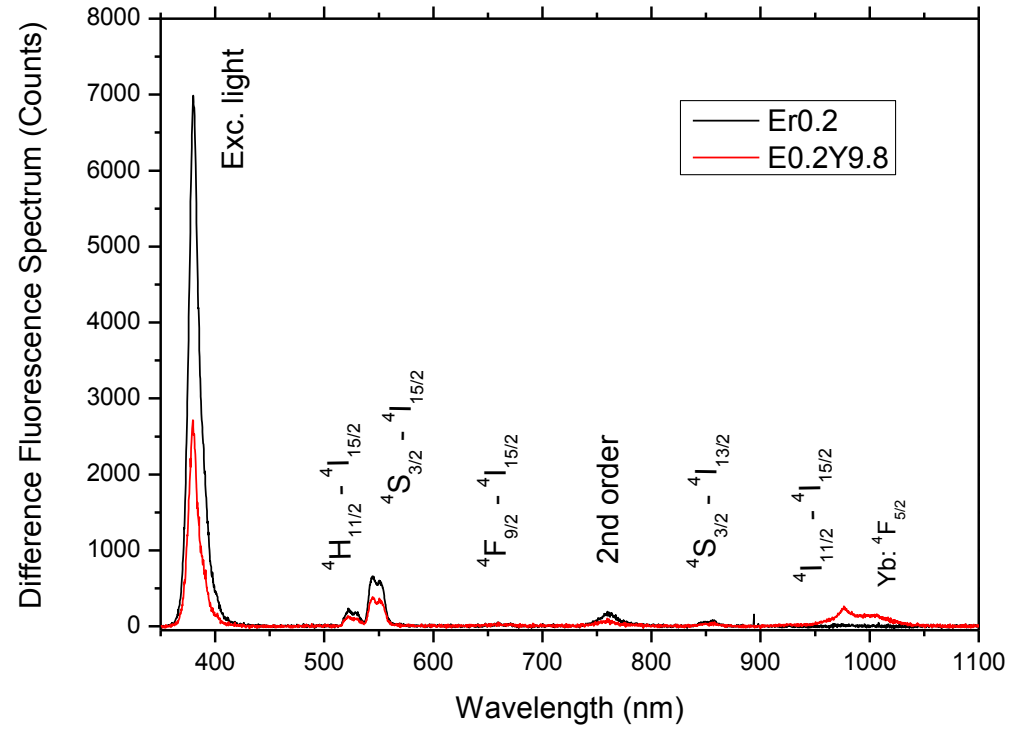

(a)

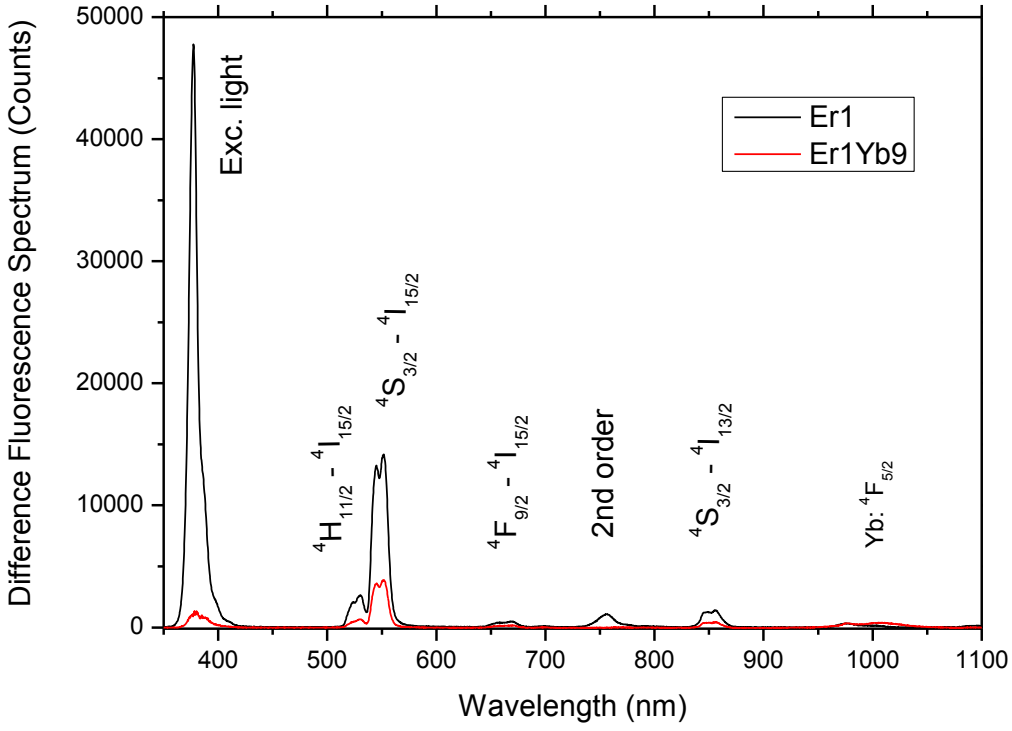

(b)

Figure 2.10: Difference emission spectra of Er/Yb co-doped Te glasses using 379 nm excitation for (a) Er0.2 and Er0.2Yb9.8, and (b) Er1 and Er1Yb9. (Spectroscopic notation denotes the energy levels of Er ions except for Yb ions)

Figure 2.11 shows the absorption, emission transitions and the cross-relaxation energy transfer process between Er and Yb ions. Cross-relaxation has been reported in a few systems such as Tm-Yb, Er-Yb, and Tb-Yb [38, 59, 68]. Based on the energy levels and luminescence properties, the following photon conversion mechanism can be observed as shown in Figure 2.11. An absorbed near ultraviolet (379 nm) photon is converted into two photons of wavelength ~ 1050 nm and 660 nm, represented by 1 and 2, respectively in Figure 2.11.

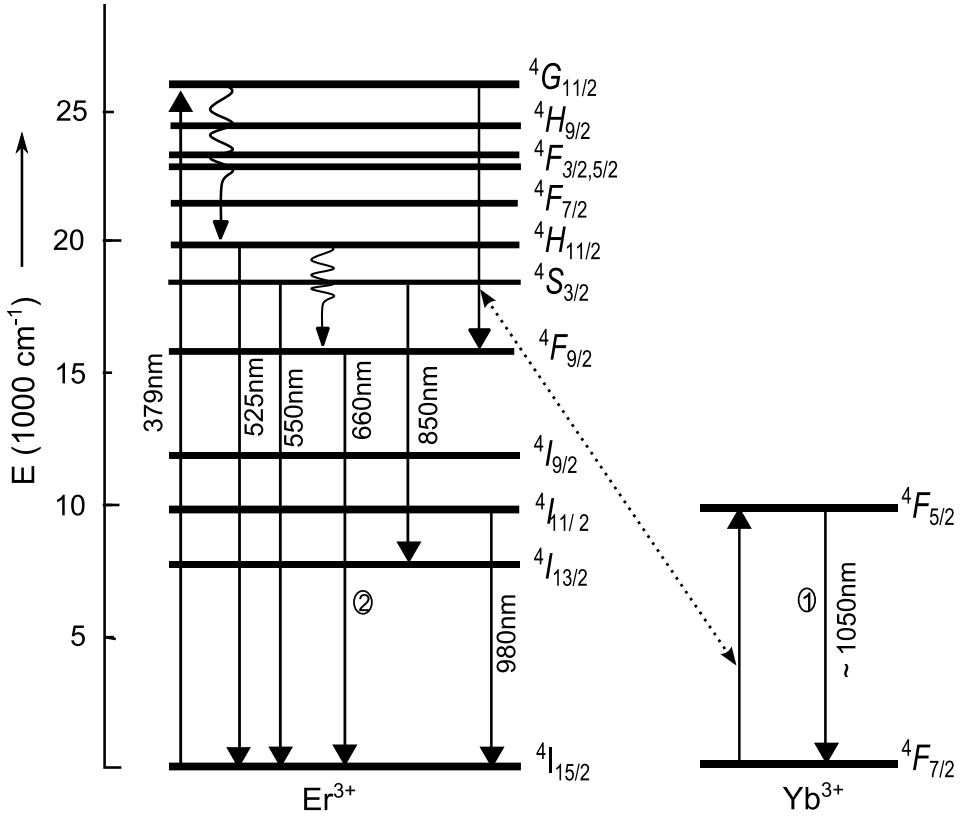

Figure 2.11: Energy level diagram of Er^{3+} and Yb^{3+} ions in close proximity showing various possible transitions. (Up and down arrows represent excitations and emissions, respectively; where the dotted arrow represents cross-relaxation transfers, while the wavy arrows represent non-radiative relaxations)

They are ascribed to the following transitions: Yb ($^2F_{5/2}$ - $^2F_{7/2}$) and Er ($^4F_{9/2}$ - $^4I_{15/2}$). Thus both of these photons can possibly create electron-hole pairs inside the silicon solar cells and may results in efficiency gain.

After accumulating all measurements and then performed data analysis, we thus obtain values of fluorescence quantum efficiency '$\eta(\lambda)$' for different samples by using Equation 2.10.

$$\eta(\lambda) = \frac{Total\ fluorescence\ in\ the\ spectral\ range\ (950\ nm\ to\ 1100\ nm)}{Total\ incident\ pump\ light\ (379\ nm \pm 12\ nm)}. \qquad (2.10)$$

The values of fluorescence efficiency for each sample are tabulated in Table 2.5. These values show low efficiency exhibited by the Er/Yb co-doped Te glass samples. Note that these efficiency values correspond to the near-infrared region (950 nm to 1100 nm), which is referred to as the region of interest (ROI). This is the region where silicon solar cells show maximum response to incident light. All the steps and calculations leading to the final value of quantum efficiency, for a sample (Er0.2Yb9.8) as an example, are described in Appendix E.

Table 2.5: Efficiency of Er/Yb samples in near-infrared region.

Samples	Efficiency (ROI: 950 nm — 1100 nm)
Er0.2	(0.1 ± 0.1)%
Er0.2Yb9.8	(2.6 ± 0.2)%
Er1	(0.9 ± 0.1)%
Er1Yb9	(4.3 ± 0.3)%

2.7 Summary of the chapter

We have presented an experimental investigation to evaluate optically a solar downconverter. The particular downconverter used for investigation was made of tellurite glass co-doped with Er and Yb ions. Further, the possibilities for downconversion of single visible or ultraviolet photon into two near-infrared photons are explored using rare-earth ions.

Different samples of varying erbium and ytterbium concentrations were examined by optical characterization. Optical absorption measurements revealed wide transparency range of the host material to the sunlight and multiple narrow absorption peaks of Er ion ranging from 350 nm to 550nm. A simple experimental technique has been developed and demonstrated for the determination of fluorescence quantum efficiency. This chapter has successfully described and tested the equipment and experimental approach to characterize a downconverter.

We describe in the next chapter the evaluation of more advanced materials for the purpose of broad absorption of UV/blue solar photons for a practical downconverter, based on the knowledge of preliminary experimental results explained in this chapter.

Chapter 3

Advanced Materials for Downconversion

- Introduction
- Objective
- Evaluation of advanced materials
- Fluorescent dyes
- Semiconductor quantum dots
- Rare-earth ions
- Initial experimental investigation
- Summary of the chapter

This chapter introduces a range of advanced materials for possible use in PV applications. First, it discusses their basic structural properties and suitability for downconversion purposes. Then, the initial work performed on the Ce doped tellurite glasses is presented. A description of instruments and experiment designs is given followed by the results obtained through UV/Vis and FTIR absorption spectra measurements. Some of the details of the equipment used for this part of research were explained in Chapter 2.

3.1 Introduction

From the preliminary knowledge gained in Chapter 2, we now extend the investigation towards more efficient energy conversion materials. The experimental results of the Er/Yb system showed narrow absorption band materials. The absorption measurement of Er ions showed a multitude of absorption peaks in the short-wavelength range of the solar spectrum, but exhibited low values of absorption coefficient. In the literature of solar downconverters, there are many examples of materials with narrow absorption profiles that cannot contribute substantially to the overall problem of improving efficiency of solar cells, with the core issue related to the absorption property of the materials.

This chapter presents the general description and the evaluation of the opportunities for the advanced materials from both light absorption and downconversion aspects. These materials are expected to satisfy the requirement of efficient broad absorption of sunlight between near-ultraviolet to blue/green region when employed in the development of a downconverter. Thus, while the fundamental idea and development of the necessary measurement techniques have been established, it is necessary to identify and evaluate a particular material (containing sensitizers) with a broad absorption spectrum. One possible way to achieve this goal is to examine other rare-earth ions such as cerium (Ce) which appear promising. As a potential sensitizer Ce ions could harvest UV/blue spectral photons within the wavelength range of 300 nm to 550 nm and then transfer the energy to a nearby activator (such as Yb) to give rise to intense NIR emission. We will also look at other types of fluorophores such

as fluorescent dyes and semiconductor quantum dots, if possible, which are known to have wide absorption band and efficient fluorescence properties.

Prior to implementing new materials in the development of a downconverter, it is essential to understand the structural and optical properties of the materials. The properties of a particular material are determined by the collective behaviour of the constituents of that material. For example, in order to understand the overall absorption of the material there are at least two factors that need to be considered: what is the absorption property of the material and what concentration of doping species should be used? The work in this chapter will study the basic characteristics of different luminescent materials.

3.2 Objective

The objective of this chapter is to discuss advanced materials and present a description of the initial experimental work. It begins by assessing advanced materials in Section 3.3, followed by the introduction and discussion of luminescent species in Sections 3.4, 3.5 and 3.6. Then it describes the initial experiments performed on Ce doped tellurite glass samples. Finally, this chapter concludes with the results obtained using Ce samples.

3.3 Evaluation of advanced materials

In this section, we outline the main results found in Chapter 2, followed by an evaluation of advanced materials. Experimental investigation on the Er/Yb co-doped tellurite glass revealed the following:

- Er ions show narrow absorption peaks in the UV/blue spectral region.
- Overall low absorption coefficients.
- Less intense NIR emission from Yb ions.
- Low quantum efficiency.

A wide range of fluorescence materials have been employed for spectral conversion through different processes suitable for PV applications and we evaluate their feasibility particularly for downconversion purposes. Based on the above experimental findings, this section highlights various contributing factors which may determine the practical suitability of a downconverter. Considering both optical and practical aspects, important factors are: i) broad absorption range of high energy solar photons, ii) efficient emission and high quantum efficiency, iii) transparency to Vis/NIR photons, iv) long stability, and v) low cost. Energy conversion materials also need to consider these factors and in this chapter are referred to as ‘advanced materials’. These materials are evaluated here to determine to what extent they fulfil the purpose of downconversion. In this pursuit, the principal strategy is to discuss host materials and luminescent species separately.

3.3.1 Host materials

The host materials serve as base materials in which luminescent ions are embedded. Their physical and chemical properties play a fundamental role in determining the overall response of a solar cell device. For example, any change in the chemical structure of the host material dramatically changes the optical characteristics of a downconverter.

Host materials may be broadly grouped into crystalline solids (such as phosphors) and non-crystalline solids (such as glasses). Generally for the host materials, there are five different properties that result in efficient performance [23]. First is the high transmittance of spectrally converted photons over the desired wavelength range. Second is the ability to dissolve luminescent species, while maintaining high optical quality and high quantum yield, which is important for luminescence properties of the downconversion process. Third, they should be ideally free of impurities or having minimal impurities in order to avoid undesirable light absorption. Fourth, host materials with lower phonon energy lead to maximum radiative emission. Finally, they should be highly resilient to the thermal exposure of sunlight and can operate in the severe conditions.

3.3.2 Luminescent species

Luminescent species are of fundamental importance because their role is to absorb photons of short-wavelengths and emit in the Vis/NIR range [69, 70]. A range of commonly available luminescent species can be broadly categorised into types such as organic and inorganic listed below:

- Fluorescent dyes (Organic).
- Semiconductor quantum dots (Inorganic).
- Rare-earth ions (Inorganic).

The characteristics of both organic and inorganic luminescent species are discussed separately and the impact of their structural and optical properties on the downconverter design is described.

3.4 Fluorescent dyes

Fluorescent organic dyes, such as Dicyanomethylene (DCM), Coumarin, and Rhodamine 6G, were originally developed for use in dye lasers, [71, 72]. Organic dyes may also be used as an optical dopant in the fabrication of a downconverter as they can be dissolved in a range of organic polymers, such as polymethlmethacrylate (PMMA), which are then cast or shaped in the form of a sheet. However, it is a challenging task to find a host material for organic dyes which is stable and long lasting. In the past, dyes have also been used in the fabrication of luminescent solar concentrator (LSC) [73, 74]. An LSC is a device that is used for capturing sunlight and concentrating it onto a solar cell for generating solar power. The device operates on the principle of total internal reflection (TIR) by collecting solar radiation over a large area and then directing the sunlight to the solar cell attached to it.

Before describing the optical properties of an organic dye molecule, it is important to discuss its basic structure. The energy level (Jablonski) diagram [50] of an organic dye is shown in Figure 3.1. Upon absorption of a photon, an electron is excited from a ground state (S_o) to one of the vibrational levels of the first excited state (S_1). It then decays non-radiatively by internal conversion to the lowest vibrational level of state (S_1). Further, it decays to one of the vibrational levels in the ground state (S_o) by emitting a fluorescence photon of longer wavelength.

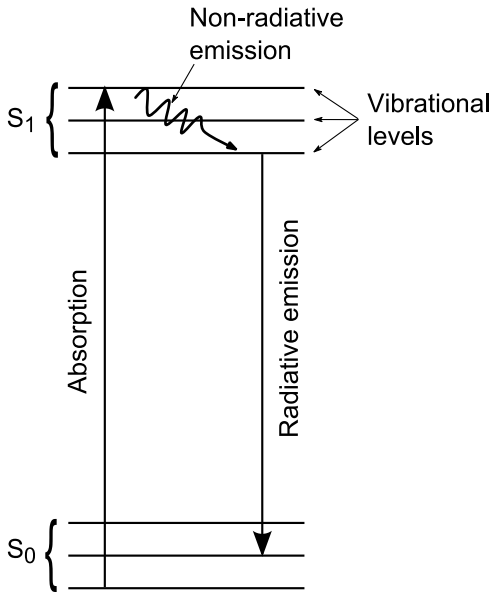

Figure 3.1: Jablonski energy level diagram of an organic dye.

Organic dyes exhibit fluorescence and high quantum efficiency. Most dyes have been demonstrated to be stable in a polymethylmethacrylate (PMMA) host incorporating a UV absorber [75]. Despite their high quantum efficiency, they absorb only a limited range of wavelength (typically ~ 70 nm) and show significant reabsorption losses. To absorb broadband sunlight incident on the solar cells, a mixture of several dyes can be used which may be costly. For example, an organic dye of a single type (Lumogen F) from BASF manufacturer roughly costs an average of US$ 15 per gram [76]. We make rough estimate of cost for the dye to be used in a sheet of 1 m^2. Consider the thickness as 1 μm, based on ~ 60% absorption allowing maximum emission using 2 μM dye concentration, which gives the volume of 1 cm^3. Thus the total amount required would be 1 g/cm^3. Since dye modules thickness ranges from 1 μm to 10 μm [73], we take the minimum thickness to be 1 μm. Based on prices from BASF catalog [76], the estimated cost (minimum) of dye would be US$ 15/m^2.

Additionally, there remains an issue of significant reabsorption losses and finding a suitable host for the incorporation of dyes. Finally, their photostability is the most important limiting factor under the sunlight exposure over longer periods of time. Thus, in consideration of the above properties, luminescent dyes may not be most suitable for downconversion purposes.

3.5 Semiconductor quantum dots

Different from the above described organic materials, another promising luminescent materials are semiconductor quantum dots (QDs). These materials are capable of converting UV/blue photons to NIR photons. In the literature, the term nanocrystal is used interchangeably with QD. From recent research investigations, they are also considered as effective light harvesters in solar cells [77]. They are strongly luminescent with high quantum efficiency. They exhibit enhanced optical properties which can be tuned by controlling their shape and size. They are known to have wide absorption bands and efficient emission intensity as well as good photostability [77]. Moreover, the use of QDs provides additional energy levels that are suitable for the application of the downconversion process. Another key point is that different preparatory methods can be employed in order to control the size of QDs as a result of quantum confinement [78]. However there is an issue of the significant reabsorption of the light. This poses a challenge for researchers to reduce the overlap between absorption and emission bands that results in reabsorption losses [79]. Some recently investigated QDs together with their challenges are discussed below.

Examples of typically used QDs are lead sulphide (PbS) and lead selenide (PbSe) which have broad absorption spectra, high absorption coefficients and emission wavelengths which can be tuned from 800 nm to 1800 nm by simply varying their size [80]. They have high fluorescence quantum efficiency of up to ~ 80% in the near-infrared range but are mostly produced in laboratory setup [81]. QDs of such high quantum efficiency are not commercially available. They have good optical quality and stability; however, they are more expensive than dyes [82, 83].

In a further example of nanocrystals, the observation of downconversion using silicon nanocrystals embedded in a SiO_2 matrix has recently been reported [84]. In this work, Er ions were used as receptors to accept emitted energy from silicon nanocrystals. It was found that the downconverted photons were transferred to co-doped Er ions in the SiO_2 matrix through photoluminescence, exhibiting low efficiency. In reference [84], it was proposed that the efficiency of the downconversion process can be improved by decreasing the separation between individual nanocrystals.

As described above, examples show limited success of using different QDs. While research continues in developing efficient nanostructure materials however, significant efforts to reduce their cost are also required. These materials could be a long term approach for downconversion solar cells.

3.6 Rare-earth ions

Before investigating rare-earth ions, the idea of using metal ions was also considered. For example metal ion ‘chromium (Cr)’ was treated as a sensitizer

since it shows broad absorption of light. However, its emission wavelength is roughly 693 nm which further cannot generate two NIR photons of wavelength ~ 1000 nm. Therefore we focused on rare-earth ions due to their numerous energy levels offering multiple radiative emissions. The energy levels of rare-earth ions arise from the 4f inner shell configuration which enables their use in photonic applications such as lasers, optical fibres and amplifiers [26]. They are also easily dissolvable in various host materials and have generally high luminescence quantum efficiency.

This study concentrated on using rare-earth ions as an intermediate approach due to both the above mentioned attractive properties and their availability in our laboratory. The rare-earth ions are described by an electronic configuration of $[Xe]4f^n$ (where n=0-14) and their corresponding energy level diagrams are displayed in Appendix F. The rare-earth ions may be classified into two groups. One group of rare-earth ions (Er, Dy, Gd, Ho, Tm, Tb, Nd, Sm, Pr, Pm) displays narrow line emissions, while a second group (Ce, Eu, Yb) exhibits broadband emission. Chapter 2 presented the use of narrow absorption material (sensitizer); while in this chapter we focus on investigating a broadband sensitiser.

Two possible candidates are europium (Eu) and cerium (Ce) which show broad and strong absorption between their 5d to 4f levels in the desired spectral range. However, they can exist in different valence states depending on the host environment and the fabrication method [26, 69]. Eu with valence state +2 shows a broad excitation spectrum in the vacuum ultraviolet region due to the $4f^7 \rightarrow 4f^6 5d$ transition. The energy of this transition is more than twice the band-gap energy of silicon but unfortunately that part of the spectrum is absent in the solar radiation

reaching the Earth surface On the other hand, Ce ions could be considered as a broadband sensitizer because of its high absorption coefficient and large absorption cross-section. Moreover, its spectral transition can be tuned by the appropriate selection of the host [26].

Of all rare-earth ions, Ce ion has been widely characterized and applied in research and development areas such as in the lighting industry due to its broad luminescence as will be discussed below. Thus, this was the practical reason to investige Ce doped tellurite glass as an intermediate step towards a broadband downconversion for Si solar cells.

The 5d to 4f level radiative emission of Ce-based phosphors has attracted considerable attention for possible use in fluorescent lamp, LED, and scintillator applications. For example, Ce is used in $Y_3Al_{12}O_5$: Ce (YAG: Ce) for white LEDs and $Lu_3Al_{12}O_{12}$:Ce (LuAG: Ce) as scintillators. The first work on Ce doped YAG as a new phosphor material for cathode ray tube was reported by Blasse and Grabmaier [61]. The combination of high luminescence efficiency and a relatively long wavelength (visible) emission made this material ideally suitable for this application. In recent years, Ce has been investigated for light sources as a colour converter in (In, Ga)N-based LED [85]. The combination of blue and yellow colour gives a bright white light source with an overall efficiency approaching that of fluorescent lamps.

3.6.1 Choice of Ce

Cerium is the second element in the lanthanide group, with an atomic number 58, and is characterized by electronic configuration of $[Xe]4f^15d^16s^2$. The Ce ion has a simple energy diagram with two energy bands 4f and 5d, separated by energy

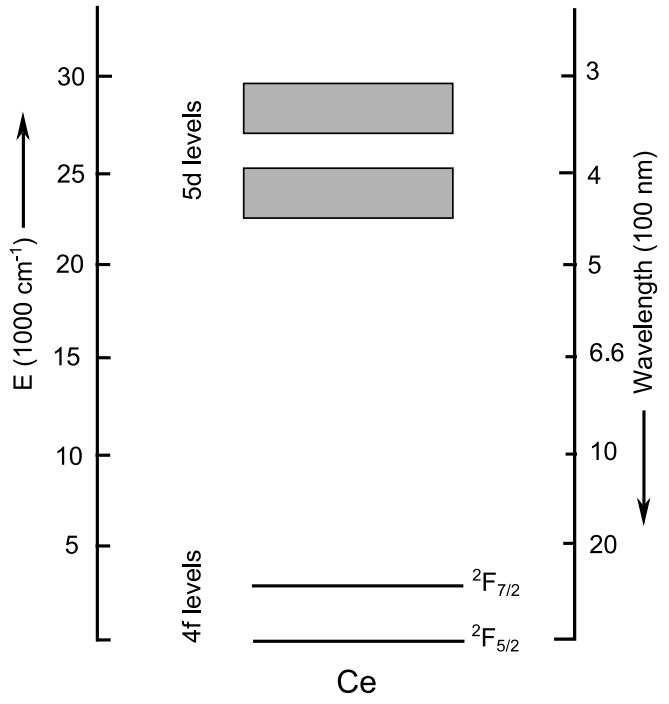

Figure 3.2: Energy level diagram of Ce ion. (Energy levels are labelled with their corresponding spectroscopic notations)

difference of around 30000 cm^{-1}, as shown in Figure 3.2. The 4f ground state configuration yields two energy levels, $^2F_{5/2}$ and $^2F_{7/2}$, separated by a width of ~ 3000 cm^{-1}.

As a potential sensitizer, Ce ion could harvest UV/blue spectral photons for absorption of high energy photons. Unlike other rare-earth ions, Ce ions generally absorb a wide band of light due to large absorption cross-section (σ ~10^{-18} cm^2) and spin allowed transition [86]. The absorption of Ce ion can be tuned between 300 nm and 550 nm, with the exact value depending on the host material [87].

3.6.2 Fabrication of Ce doped Te glass

The tellurite glass of chemical composition, $73TeO_2–20ZnO–5Na_2O–2La_2O_3$, was prepared for this study. Host raw materials with 99.99% or higher purity were

used as received from commercial suppliers. Two different compounds [CeO_2, $Ce_2(CO_3)_3$] of cerium were used. We selected tellurite glass which enabled us to make comparison with the preliminary work presented in Chapter 2. The bulk glasses were fabricated by a conventional melting and quenching method. Further the glass samples were cut to the thickness of 1.0 ± 0.1 mm from blocks of dimensions 15×10×30 mm^3 for spectroscopic measurements. The physical description of un-doped and Ce doped samples is provided in Table 3.1.

Table 3.1: The physical description of Ce doped Te samples.

Samples	**Doping concentration (ions/$cm^{3)}$**	**Raw oxide materials**
un-doped Te	–	TeO_2, ZnO, Na_2O, La_2O_3
Ce–34	0.1×10^{20}	TeO_2, ZnO, Na_2O, La_2O_3, CeO_2
Ce–66	0.1×10^{20}	TeO_2, ZnO, Na_2O, La_2O_3, $Ce_2(CO_3)_3$

The samples were designated as un-doped Te, Ce-34, and Ce-66. The difference between two Ce doped samples was that, in each sample, different compounds of cerium were used. All spectroscopic samples were polished on both sides in order to reduce surface irregularities prior to the optical measurements.

3.6.3 Issues with Ce

In solid materials, Ce ions can exist in a trivalent (+3) or a tetravalent (+4) state by losing its two 6s electrons and one or both of its 4f electrons [88]. Ce^{3+} ions may be excited to a 5d state by optical pumping directly or indirectly. In the first case, the excited Ce ion will emit a photon (5d to 4f) via $(Ce^{3+})^* \rightarrow Ce^{3+} + h\upsilon$. In the second case, the Ce ion may lose its 4f electron to form Ce^{4+}, either optically

or by capturing a hole created in the valence states of for example, oxygen via the process $Ce^{3+} + h\upsilon \rightarrow Ce^{4+}$. The charge transfer in the latter process may complicate the downconversion process. It has been shown that the absorption spectrum of Ce^{4+} peaked at a wavelength of ~ 250 nm, whereas for Ce^{3+}, it peaked around a wavelength of 350 nm [88]. Therefore, it is necessary to address the issue of Ce ion valence state in a particular host material before a spectral converter could be developed.

3.7 Initial experimental investigation

The Ce doped tellurite glass samples were characterized by measuring the UV/Vis absorption and the FTIR absorption spectra. These measurements assisted to observe the optical features of samples, such as the absorption of light by the Ce ions, intrinsic host absorption, and the wavelengths over which the sample is transparent. The experimental methods and results obtained through both UV/Vis and FTIR absorption spectroscopy are explained below.

3.7.1 UV/Vis absorption spectroscopy

Absorption measurements were performed using the optical spectrophotometer (Model: Cary 5000) similarly to the measurements described in Chapter 2. The fractional transmission of each luminescent sample was recorded. The fractional transmission is the ratio of transmitted intensity through the sample to the incident intensity of light. Subsequently, the absorption coefficient was calculated for each sample using the transmission and sample thickness, as was explained in Section 2.4.1.

The resulting absorption spectra of Ce doped samples together with an un-doped sample, corrected for surface reflection loss, are shown in Figure 3.3. Two remarkable features can be pointed out as follows. First, both samples show wide transparency to the incident light from visible region to NIR region. Second, Ce ions show wide band absorption in the UV/blue region ranging from 350 nm to 440 nm. This absorption of light is attributed to the spin allowed transition from 4f to 5d levels of Ce ion [87, 89]. The absorption edge around 345 nm is due to the host constituents and electronic vibrations which can be observed from the absorption trend of an un-doped Te glass sample.

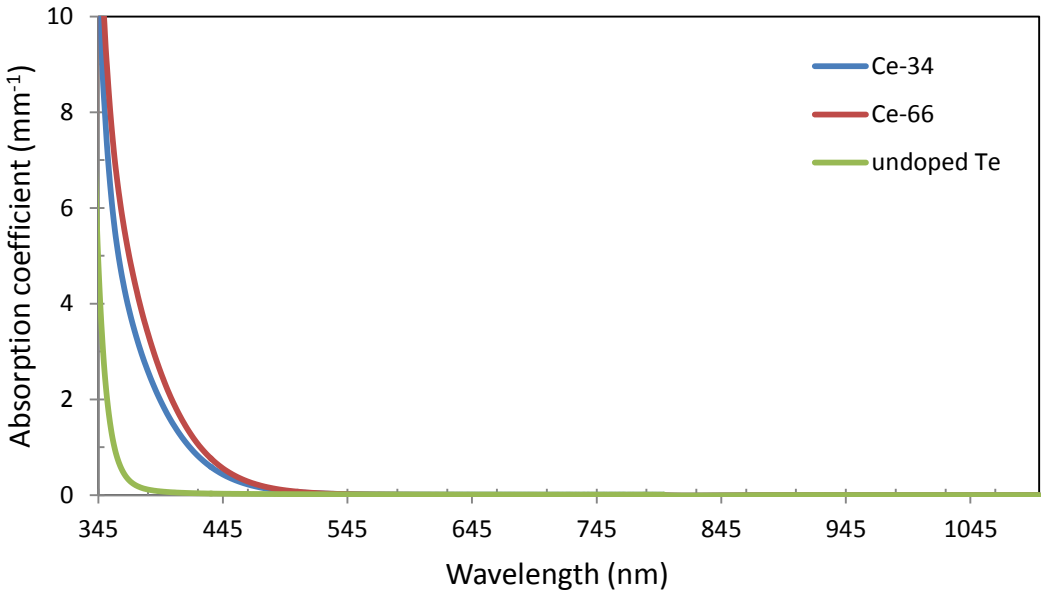

Figure 3.3: Optical absorption spectra of un-doped and Ce doped Te glasses.

Both samples show similar absorption band which reflects same amount of Ce doping as tabulated in Table 3.1. From Figure 3.3, it is difficult to identify the presence of Ce ions in a particular valence state such Ce^{3+} or Ce^{4+}. Because the full absorption band is invisible to observe the peak absorption by Ce ions and this was limited due to the intrinsic UV absorption of host tellurite glass. The UV

edge absorption of Te glass samples under investigation could be ascribed to Rayleigh scattering [56]. Thus, this study will further examine the FTIR spectra to determine the valency of Ce ions, as discussed in the following section. It is expected that Ce^{3+} show absorption bands in the infrared range (3 μm to 5 μm).

3.7.2. Infrared absorption spectroscopy

Fourier Transform Infrared (FTIR) absorption spectroscopy is one of the advanced spectroscopic techniques. This technique helps to identify the presence of any functional groups (such as OH^- ions) in solid materials and allows probing the low frequency vibrations of a solid. One can also use the collection of absorption bands and the detection of specific impurities in the infrared region to explore the properties of a solid.

The purpose of this section is to study infrared characteristics of Ce doped Te glasses in order to find out valence state of Ce ions. Thus FTIR spectra measurements[5] will be taken and it is expected that a peak in the FTIR absorption spectra around wavelength of 4 μm will show presence of Ce^{3+}.ions [90]. The determination of the Ce^{3+} ions enables us to make an optimal choice for use in the preparation of a downconverter.

This study recorded infrared absorption spectra of samples using a commercial PerkinElmer FTIR spectrometer (Model: Spectrum 400). This spectrometer is capable of measuring absorption and transmission over a wavelength range from 1 μm to 10 μm. Generally, FTIR instruments consist of three main components: a light source, interferometer, and a detector. A simplified optical layout of a typical

[5] Another option was to use electron spin resonance technique (EPR) to analyse the valence state of Ce ions, however, this was out of our capability due to unavailability of the instrument. Therefore, we used Fourier transform infrared spectroscopy to study Ce ions.

FTIR spectrometer is illustrated in Figure 3.4. This Figure is divided into two parts: A and B. Figure 3.4(A) shows a light source and a detector with a sample holder in between while Figure 3.4(B) shows a Michelson interferometer which is explained later together with the description of the technique. The samples investigated were the same as those described in Section 3.6.2. The FTIR spectra were scanned in the wavelength range from 2 μm to 7 μm with a resolution of 4 cm^{-1} through software.

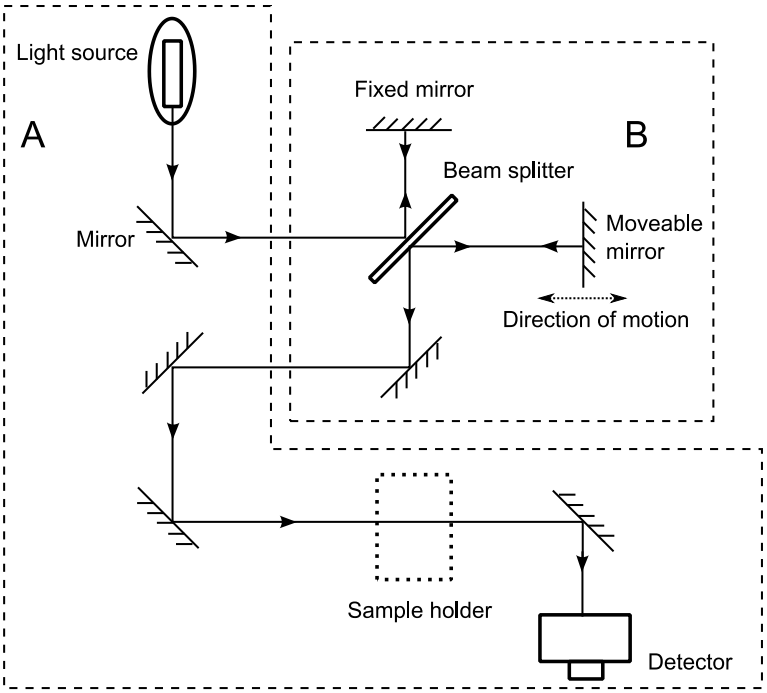

Figure 3.4: A schematic representation of an instrument for measuring FTIR absorption spectra[6].

The FTIR spectrometer was used in transmission mode and the transmission measurement was performed via the following steps. First, a background spectrum was recorded with an empty sample holder. Second, the sample was placed in a holder and the resulting spectrum was measured, which was

[6] Source: Modified and redrawn picture of Perkin Elmer instrument which can be found at www.perkinelmer.com/FTIR/usermanual.

proportioned against the background spectrum to eliminate features introduced by the instrument components. The commercial software ‘Spectrum’ [91], was used to operate the spectrometer and record spectra.

In FTIR spectroscopy, the Michelson interferometer is the central part of the spectrometers. It consists of three optical components i.e. a beam splitter, a fixed mirror and a moveable mirror shown schematically in Figure 3.4(B). The collimated beam of light from the source reaches the beam splitter, where it is divided into two halves. One half of the light beam is transmitted to the movable mirror and the other is reflected to the fixed mirror. These two beams reflect back from the mirrors and subsequently recombine at the beam splitter, resulting in a new beam that passes through the sample and is further steered towards the detector as shown in Figure 3.4(A). The resulting intensity signal is referred to as an “interferogram”, which is recorded at the detector as a function of path difference.

For the sake of simplicity, first consider an IR beam emanating from a monochromatic light source of wavelength, λ, which passes through an empty interferometer. If both mirrors (moveable and fixed) are at the same distance, L (x=0), from the beam splitter, the two reflected beams that recombine at the beam splitter travel the same distance (x=2L) resulting in constructive interference, so that a maximum is recorded at the detector. Now if the moving mirror is displaced from the beam splitter by a distance, λ/2, the reflected beam from the moving mirror will travel an extra distance (x=2(λ/2)=λ) and constructive interference will again be observed.

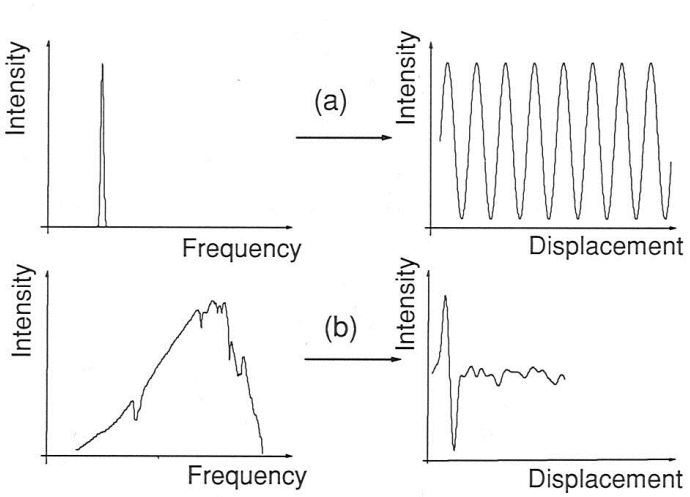

Figure 3.5: (a) A spectrum of a monochromatic IR beam source (left) and its corresponding interferogram (right), and (b) A spectrum of a broadband lamp (left) and its corresponding interferogram (right) [92].

However, if the moving mirror is displaced by a distance, λ/4, the beam reflected will now travel an extra distance (x=2(λ/4)=λ/2). Subsequently, two halves of the beam that recombine at the beam splitter cause destructive interference so that a minimum is recorded at the detector.

Thus, for a monochromatic light source of a given wavelength, one finds an interferogram (right) as shown in Figure 3.5(a). In general, if a moveable mirror is displaced the following distance (x=nλ) or (x=(n+1/2)λ), where n is an integer, then constructive or destructive interference takes place, respectively. Now consider an infrared lamp as the incident light source. In this case, a large number of wavelengths are emitted and the intensity is measured at the detector. Figure 3.5(b) shows a typical shape of the spectrum of a lamp (left) and its corresponding interferogram (right). For usual data acquisitions with an FTIR spectrometer, the interferogram is measured and then must be converted by means of a Fourier transformation [92] to give the final signal as an output.

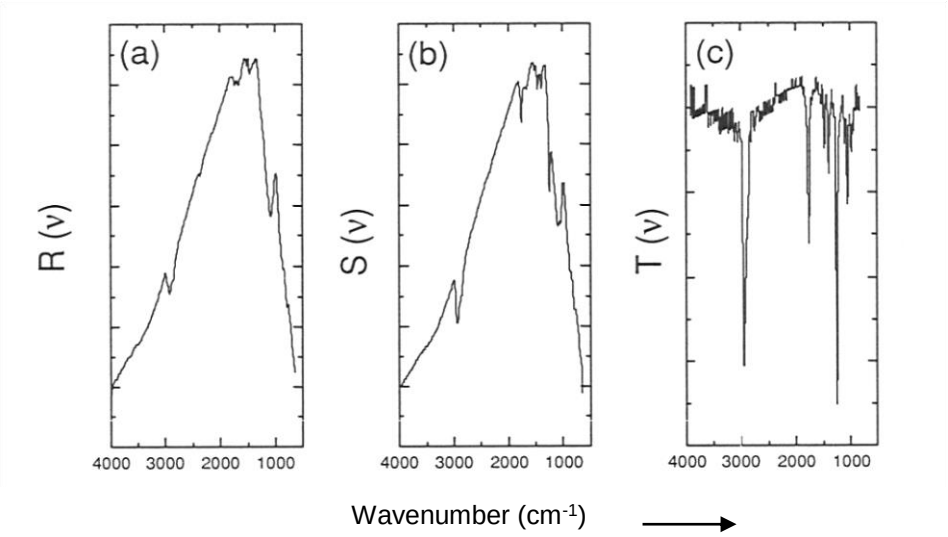

Figure 3.6: (a) A reference spectrum of a lamp measured through an empty spectrometer, (b) A spectrum measured with a sample, and (c) The final transmittance spectrum of the sample [92].

FTIR spectrometers generally provide transmittance spectra 'T(ν)' via the following three simple steps: i) An interferogram is measured with the empty spectrometer (without a sample). It is then Fourier transformed to give the reference spectrum 'R(ν)' as shown in Figure 3.6(a), ii) In the second step, an interferogram is measured when the sample is placed in the path of light beam. A sample spectrum 'S(ν)' is obtained after Fourier transformation (see Figure 3.6(b)), and iii) Finally, the transmittance spectrum of the sample in the form of Fourier transform spectrum is obtained through relation T(ν) = S(ν)/R(ν), (i.e. the ratio of the sample and reference spectra) as shown in Figure 3.6(c).

The measured FTIR absorption spectra of all our samples are shown in Figure 3.7. The absorption coefficient of each sample was calculated from the Beer-Lambert law in units of per millimetre. It is evident from FTIR spectra that all samples show similar features over the wavelength range from 2 μm to 6 μm.

The minor peaks present around a wavelength of 3.5 μm show the instrument artifact for all the samples. Initially, these measurements were performed using two different compounds with Ce ions in different oxidation states to determine +3 valence state.

Qualitative analysis of the FTIR spectra reveals two general features; first is the location of multi-phonon edge in mid infrared region and the other is the amount of hydroxyl (OH) groups or ions present in the tellurite glass samples. The tellurite glass samples under investigation were prepared in an open atmosphere. Accordingly all FTIR spectra show the presence of water contents in the form of broad peaks i.e. strong vibrations of OH groups at wavelengths around 3.5 μm and 4.5 μm as shown in Figure 3.7.

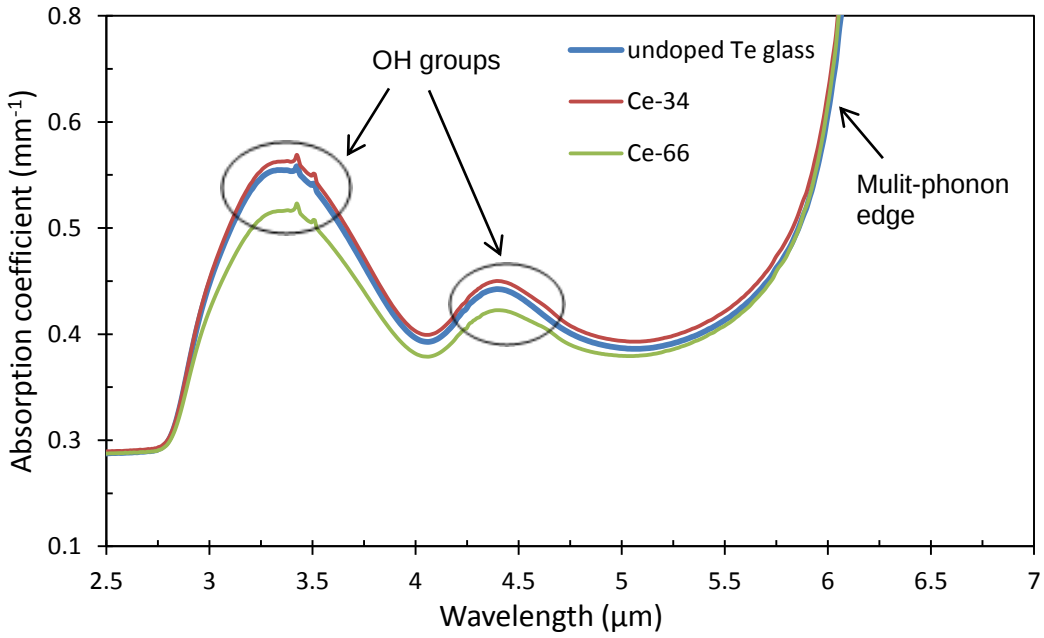

Figure 3.7: FTIR absorption spectra of un-doped and Ce doped Te glass. (Samples specifications were listed in Table 3.1)

Furthermore, the sharp rise in absorption can be noticed around the wavelength of 6 μm where combinations and overtones of the fundamental lattice vibrations occur and hence represents IR multi-phonon edge [56]. These results show the absence of a strong absorption peak around 3.8 μm which would correspond to the Ce^{3+} transition between levels $^2F_{7/2}$ and $^2F_{5/2}$ [61, 90]. This could be due to the following two reasons. First, the Ce^{3+} peak is superimposed by the strong absorption of OH groups as shown in Figure 3.7, however, maximum resolution of the FTIR instrument was chosen so as to observe Ce^{3+} ions presence. Second, this may be due to the lower concentration of Ce ions (0.1×10^{20} ions/cm^3) doped in Te glasses since the detection of peak Ce^{3+} was observed by varying Ce concentration [90, 93]. Therefore, comparing FTIR result with literature [90], the minimum concentration of Ce content should be used as 2×10^{20} ions/cm^3 in order to detect Ce^{3+} ions. Thus, it can be suggested that the emission from Ce ions was suppressed due to the presence of OH content. The OH ions/content related absorption could be controlled by employing dry raw materials or by melting glass in nitrogen atmosphere. Hence it will reduce the OH content in tellurite glass and Ce^{3+} may be detectable from the FTIR measurement. Further, fluorescence measurement using these samples may enable us to make a final remark on the Ce valence state.

3.8 Summary of the chapter

In this chapter, we have discussed advanced materials by evaluating to what extent they are suitable to be used in the preparation of spectral converters. Their

basic structures and properties are described hence to determine the absorption and luminescence.

Initial investigation was completed using Ce doped tellurite glass system. The UV/Vis absorption spectra showed broad absorption. Further, FTIR investigation was performed to find Ce^{3+} ions presence in the samples. While the initial experiment demonstrated, the evaluation was inconclusive due to presence of OH content in the samples. Subsequent step would be to perform experiments once new samples with different concentrations of Ce are obtained. Additionally, it remains to be determined that over what wavelength range the samples investigated above show fluorescence. The emission measurement of these samples was not performed due to the time limitation. Overall, the application of rare-earth ions (cerium) offers opportunity to some extent to be used for energy conversion materials. However, semiconductor QDs might be promising materials for downconversion scheme.

Chapter 4

Summary and Conclusion

- Chapters summary
- Future work directions

This thesis was concerned with the study of advanced approaches to improve efficiency of Si solar cells. In particular, a key approach 'downconversion scheme' was studied which aims to generate at least two useful low energy photons from one high energy incident photon. To accomplish this goal, the solar downconverters were fabricated and then evaluated primarily by determining their optical characteristics. The major contributions of this work are summarized in Section 4.1 and some future work directions are given in Section 4.2.

4.1 Chapters summary

This thesis presents an investigation of solar downconverters that convert UV/blue-green photons to near-infrared photons which can be absorbed by silicon solar cells. In this work, we developed the methodology required and used it to study downconverters experimentally. This involved determining the optical properties such as UV/Vis absorption spectra, fluorescence spectra, FTIR spectra, and FQE.

As introductory material for this investigation, various approaches aiming to increase the efficiency of Si solar cells were reviewed. The discrepancy of 8% between theoretical and laboratory efficiency of Si solar cell led this study to examine the potential of the downconversion approach. Consequently we studied solar converters in terms of whether they exhibit downconversion phenomenon. It was necessary to understand the luminescent materials used and their optical properties.

A detailed description of an experimental technique to examine the downconveters by means of FQE was described in Chapter 2. This technique is simple, portable, accurate, and low cost because it utilizes readily available optics and a commercial spectrometer. Our experimental technique is a useful contribution for measuring the quantum efficiency of different glass samples or thin-films samples. In addition, this technique can measure a range of samples available either in solid or liquid form. The experimental technique was verified by measuring efficiency of a reference Rh-B sample. The results obtained were then compared with the currently accepted efficiency values in the literature.

The FQE was used to assess the practical suitability of downconverters. It was found that tellurite glasses doped rare-earth ions (Er/Yb) are not viable for

practical application because they exhibited only narrow band absorption of sunlight and very low efficiency but were useful to establish the experimental technique.

Chapter 3 presented an overview of advanced materials evaluated in the context of broad absorption of high energy part of solar spectrum. The basic structures of the constituent units of a particular material determine the required property of new photonic device. The cerium doped tellurite glasses were studied initially by exploring their UV/Vis absorption and the FTIR spectra. The purpose of initial study was to investigate the valency of Ce ions present in the material. Initial FTIR results were inconclusive for the Ce^{3+} ions presence in our tellurite glasses. However future experiments based on this work would resolve this problem. We also began investigating suitable architectures, a subject that has not been treated thoroughly in the literature

4.2 Future work directions

During the course of this project, a few promising areas emerged that require further investigation. For example, investigated rare-earth ions absorb light in narrow absorption bands despite the fact that they possess numerous energy levels. If a significant improvement in Si solar cells performance is to be achieved, it must come from doping species-RE ions or hybrid materials which exhibit wide band absorption and subsequently emit light around the optimal point where silicon solar cell shows maximum efficiency.

Further work is needed to ascertain energy transfer pathways and the actual number of NIR photons emitted per UV/blue photon. More characterization for

example, fluorescence measurement is required to make conclusive decision for the choice of cerium ion as sensitizer.

However, semiconductor QDs seemed to be promising avenue of research for future perspectives, particularly, for the purpose of harnessing UV through blue to green solar photons available in the solar spectrum. It is due to the fact that they posses abundant energy levels that can be tuned according to the incident sunlight and have small structures at the scale of approximately 10 nm. Therefore a whole new set of QDs as advanced energy conversion materials will be required for the downconverter. Alternatively, the QDs material may be deposited on the top or injected inside the silicon solar cells to obtain the potential use of downconversion scheme. The experimental approach developed in this thesis will be very suitable for investigating downconverters making use of QDs.

Appendix A

Architectural configuration of a PV device: Analysis

Conversion of solar energy to useful electrical energy is becoming ever more important in the PV research. A plethora of work reported in the literature focuses on studying the downconversion scheme. The key parameter ‘quantum efficiency’ is measured to determine the characteristics of the spectral converter. The research in the field of sunlight conversion is in progress, however, there is no report to the best of our knowledge, describing the analysis of the architectural design of a PV device i.e. downconverter with a silicon solar cell. In this section, we describe the structural design when the downconverter is attached to a solar cell as was schematically shown in Figure 1.4(b) (see Page 11). The downconverter alters the spectral content of the incident sunlight before entering the Si solar cell. The addition of a downconverter to a solar cell can be beneficial in obtaining efficiency gain by utilizing high energy photons that otherwise create thermalization losses. The reduction of these spectral losses is imperative to improve efficiency for practical use.

A large part of spectral loss is related to the reflection of incident light. When the incident light impinges normally, for example, on a bare Si solar cell, a significant amount of light is reflected from the front interface between air (n=1) and Si solar cell (n=4.10) which results in 36% of the incident light being reflected. The

addition of a downconverter which is made up of glass such as soda-lime (n=1.5) on the top of a Si solar cell introduces reflection loss of 21% due to the interface between glass and Si. Note that above refractive index values correspond to a wavelength of 550 nm since solar spectrum has maximum intensity around this wavelength. As seen above, these reflection losses result due to the large difference of refractive indices between two media. One possible way to avoid reflection losses is to use anti-reflection coating (ARC). An ARC is made up of a specific material which exhibit special characteristics to counter the reflection of light [94]. In an ideal case, zero percent (0%) reflection can be obtained for monochromatic incident light if the refractive index of ARC is equal to

$$n = \sqrt{(n_1 * n_2)}, \tag{A.1}$$

and the thickness ‘d’ of the ARC must follow the relation

$$d = \lambda / 4n, \tag{A.2}$$

where ‘n’ is the refractive index of the ARC material and ‘λ’ is the wavelength of incident light.

The thickness of the ARC can be controlled in order to produce destructive interference (if the thickness is equal to one-quarter of a wavelength). The criteria outlined above for zero percent reflection is valid only for the light of a single wavelength ‘λ’, however, an ARC to cover the whole solar spectrum is not possible utilising this approach in isolation. Thus we explain a modified model of a PV device as was discussed in Section 1.3.1 in order to counter the reflection losses. A prototype model of a PV device together with the chosen ARC’s is schematically shown in Figure A.1.

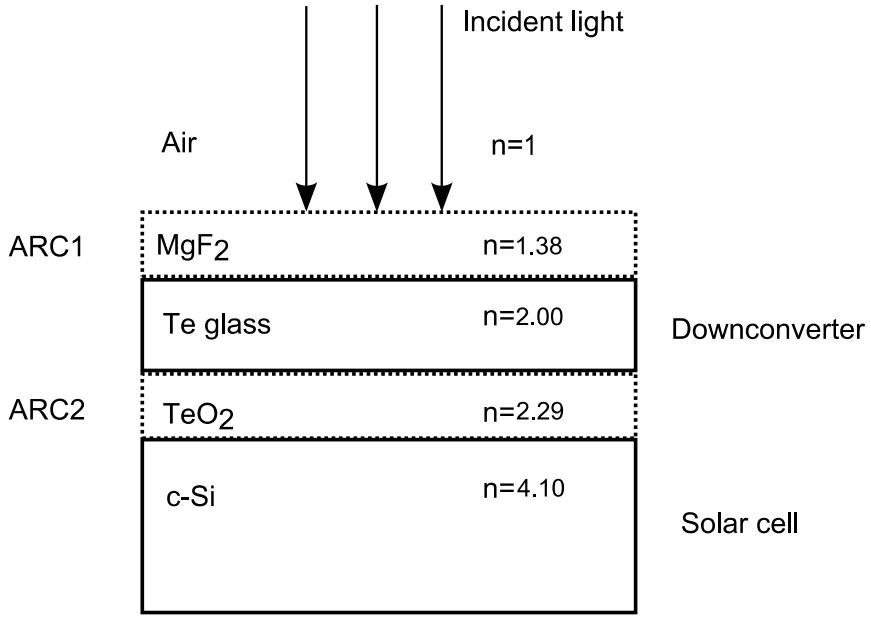

Figure A.1: Schematic optical configuration of a PV device consisting of a downconverter with AR coatings on both sides and a silicon solar cell.

This model consists of three components i.e. ARC's, downconverter, and a solar cell. A downconverter made from tellurite glass and a c-Si solar cell is considered. Two ARC's are chosen according to the refractive indices based on the Expression (A.1). The purpose of these ARC's is to reduce reflection losses.

Consider a simple scenario when incident light falls perpendicularly on a system as shown in Figure A.1. The best possible chosen ARC's based on above criteria are made up of MgF_2 (n=1.38), and TeO_2 (n=2.29) labelled as ARC1 and ARC2. The idea for using MgF_2 is to reduce the large refractive index difference between air and a downconverter and for TeO_2 is to produce index matching medium between a downconverter and a c-Si solar cell (see Figure A.1). The ARC1 is placed at the top of a downconverter while ARC2 is sandwiched between a downconverter and a c-Si solar cell as shown in Figure A.1. The sunlight falling on this system thus passes through four different interfaces i.e. air/MgF_2,

MgF_2/Te glass, Te glass/TeO_2 and TeO_2/c-Si before it enters the Si solar cell. Accordingly, the reflection from these interfaces is 2.4%, 3.3%, 0.4%, and 9% respectively. These calculations were performed by choosing best thicknesses of the two ARC's (ARC1 and ARC2) as 90.6 nm and 54.6 nm to minimize reflection losses. So the maximum (~ 85%) of incident light reaches the Si solar cell prior to absorption.

The inclusion of a downconverter as described above (see Figure A.1), causes different optical losses which are: 1) front surface reflection, 2) escape cone loss of emitted light, 3) unabsorbed light or transmitted light, 4) non-radiative decay, 5) re-absorption losses, and 6) host absorption as shown in Figure A.2. The latter three losses are intrinsic which can be avoided only by choosing a high quality host and luminescent ions.

The reflection from the front surface occurs due to the large refractive index of host material which can be reduced by using anti-reflection coating as was discussed above. However, there remains a challenge to circumvent escape cone losses (ECL).

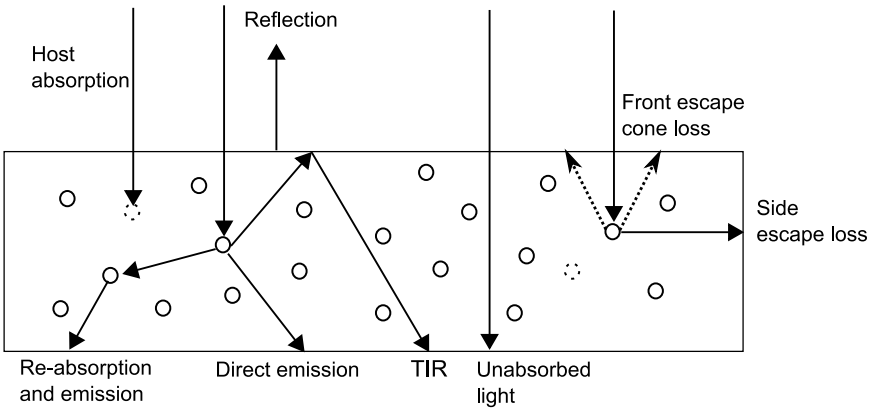

Figure A.2: A 2D cross-sectional view of a downconverter showing possible optical processes. (Solid and dotted circle represents luminescent ions and impurity ions respectively)

Escape cone losses occur due to the isotropic nature of the emitted light. Generally the photons are emitted uniformly in all directions of a sphere (4π steradians). The photons emitted towards the Si solar cell need to cross two interfaces only i.e. Te glass/TeO_2 and TeO_2/c-Si as shown in Figure A.1. The reflection from the interface between TeO_2/c-Si is high which can be further reduced by using light trapping structures [95]. The loss of emitted light in the cone shape results only if the emitted light strikes to internal surface with an angle less than critical angle 'θ_c' given by ($Sin\theta_c = n_{air}/n_{glass}$). In the case where a sole downconverter is coupled to the solar cell, the critical angle 'θ_c' will be 30° between air ($n_{air}=1$) and tellurite glass ($n_{glass}=2$). This loss can be reduced by using a proper reflective coating which is selectively reflective at the wavelengths where luminescent impurity emits. The total fraction of downconverted solar radiation and reaches the Si solar cell into 2π steradians is 45.3%. However, this reflective coating may hinder the incident light. To overcome this issue, we propose a new design which is explained below.

A.1 Proposed architecture design

One possible approach to avoid escape cone losses is to consider an architectural design that uses a downconverter in a different way. The proposed architectural design is shown schematically in Figure A.3. This model will not only reduce escape cone losses but also help to reduce other losses such as reflection loss, unabsorbed light, and the side escape losses. We explain the particular chosen design of a device followed by the advantages over the approach described above.

This configuration consists of three components i.e. solar cell, downconverter, and a rear reflector. In this architectural design we consider a thinfilm solar cell made of Si material with a downconverter attached on the rear side as shown in Figure A.3. The purpose of using a rear reflector (perfectly reflecting mirror) is to reflect all the emitted photons escaping the downconverter back into the solar cell. Additionally, this approach helps to make use of incident photons leaving the solar cell which are subsequently absorbed by the downconverter. For the sake of simplicity, we consider a simple case where the incident sunlight falls perpendicularly on the proposed device as shown in Figure A.3.

There will be a significant amount of reflection loss due to the large difference of refractive index between air and Si which can be reduced by using trapping techniques such as texturing the front surface of the Si solar cell, as shown in Figure A.3, so as to obtain more light into the semiconductor of the solar cell for maximum absorption purposes. In this way incident light remains trapped, until it

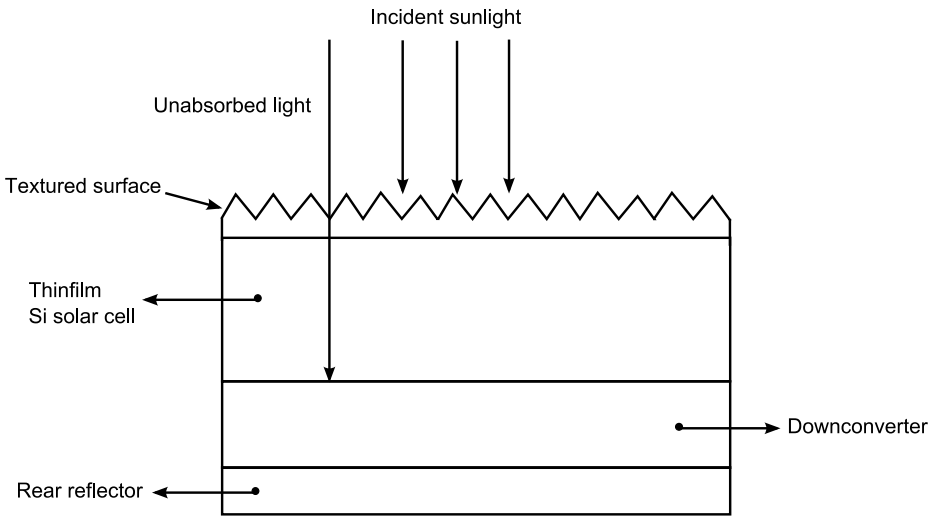

Figure A.3: Schematic representation of a proposed architectural design.

is either absorbed or scattered. Thus this design reduces the front reflection losses, and increases the absorption of light by the thinfilm Si solar cell [96].

Finally side escape losses from the downconverter can be avoided by using an ARC of proper thickness or painting by a white colour. This approach looks promising, however further work is needed to ascertain its practicality.

APPENDIX: A

Appendix B

Light sources specifications

The specifications and performance ratings of blue and UV light emitting diodes, as provided by the manufacturer, are listed in Table B.1. Both these light sources were obtained from THOR LABS Inc.

Table B.1: Specifications of Blue and UV light emitting diodes.

Parameters	**Blue LED**	**UV LED**
Model	M455L2	LED38L
Wavelength	455 nm	375 nm – 380 nm
Bandwidth (FWHM)	50 nm	12 nm
Optical power	400 mW	8.1 mW
LED current (max)	1600 mA	100 mA
LED forward voltage	3.5 V	3.7 V
Lifetime	>50,000 hrs	---

Appendix C

Spectral calibration of the spectrometer

There are different ways to calibrate the whole experimental setup, depending on how data is processed later on.

The spectral calibration of the spectrometer is always required. It is an easy process and is necessary in order to observe the spectral transitions at correct wavelengths. Various sources e.g., dual mercury and helium/neon lamp (Model: USB-Hg-Ne/Ar, Acton Research Corp.; pen type lamp inside a cuvette shaped glass) were employed in conjunction with the spectrometer to record the spectral peaks at the charge-coupled detector (CCD). Subsequently, observed spectral peaks were compared with the NIST standard data. This process enabled wavelength calibration of the spectrometer and ensured the validity of the experimental results.

The emission spectrum of the ordinary white fluorescent lamp is shown in Figure C.1.

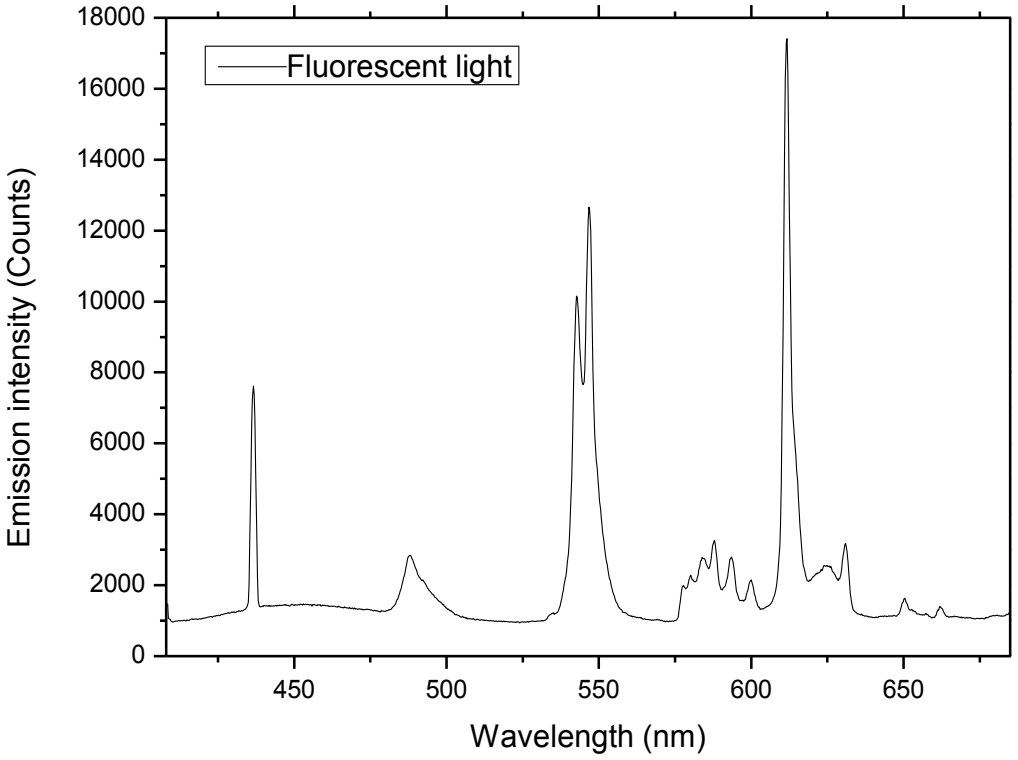

Figure C.1: Emission spectrum of fluorescent white light.

Appendix D

Verification of experimental method

This appendix describes the verification of the experimental method that was demonstrated in Section 2.6.1. We performed measurements using a reference fluorescence sample. Subsequently the experimental data was analysed and compared with the accepted value of a reference sample in the literature.

D.1 Reference fluorescence sample

Generally, the requirements for a reference fluorescence sample are quite specific. It should have the following properties [97]:

1) a broad fluorescence spectra
2) as small an overlap as possible between absorption and emission spectra
3) a known quantum efficiency
4) be able to absorb and emit in the desirable wavelength regions as that of the sample under study.

Fluorescent dyes can be used as the reference sample for experiment verification purposes. There are several well known fluorescent dyes for example Quinine sulphate dehydrates (QSH), Coumarin, Rhodamine-B, 3B, 6G, 101, and 110.

We selected Rhodamine-B (Rh-B) as a reference fluorescence sample for our experiment because of its availability in chemistry laboratories and its properties

are well known in the literature. For sample preparation, there is a range of solvents available for example, butanol, propan-2-ol, acetone, ethanol and methanol. We chose ethanol (abbreviation: EtOH) as a solvent since it showed excellent transparency in the visible wavelength range[7]. Another reason of preference to choose ethanol is that it is the main solvent used in most fluorescence databases, thus allowing for comparisons to be drawn. Finally, Rh-B was dissolved in ethanol, both of being spectroscopic grade.

It is a challenging task to check experimental setup over an extended range of wavelengths since we recorded emission spectra of tellurite glass samples in the spectral range from 350 nm to 1100 nm. It is impossible to find any single reference compound that fluoresces over a wide wavelength range, however, a mixture of standard dyes or samples can be used which limits the accuracy of the measurement. For this reason, we chose a single reference fluorescence sample which fluoresces over a limited wavelength range.

D.2 Experimental

A schematic representation of the experimental setup is shown in Figure D.1. The experimental setup for verification is similar to that described previously in Section 2.6.1 with minor modifications in the excitation part.

A cw laser (class III-b) of wavelength 533 nm was used to illuminate samples. The excitation wavelength was chosen from the measurement of the absorption spectrum of Rh-B. A solution of Rh-B and ethanol contained in a quartz cell (Width ~ 10 mm), from Beckman Inc., was placed in the path of excitation light. A

[7] The measurement was made using a Cary spectrophotometer at our laboratory.

variable ND filter was placed in the path of a beam emanating from the laser to avoid the damage of the detector.

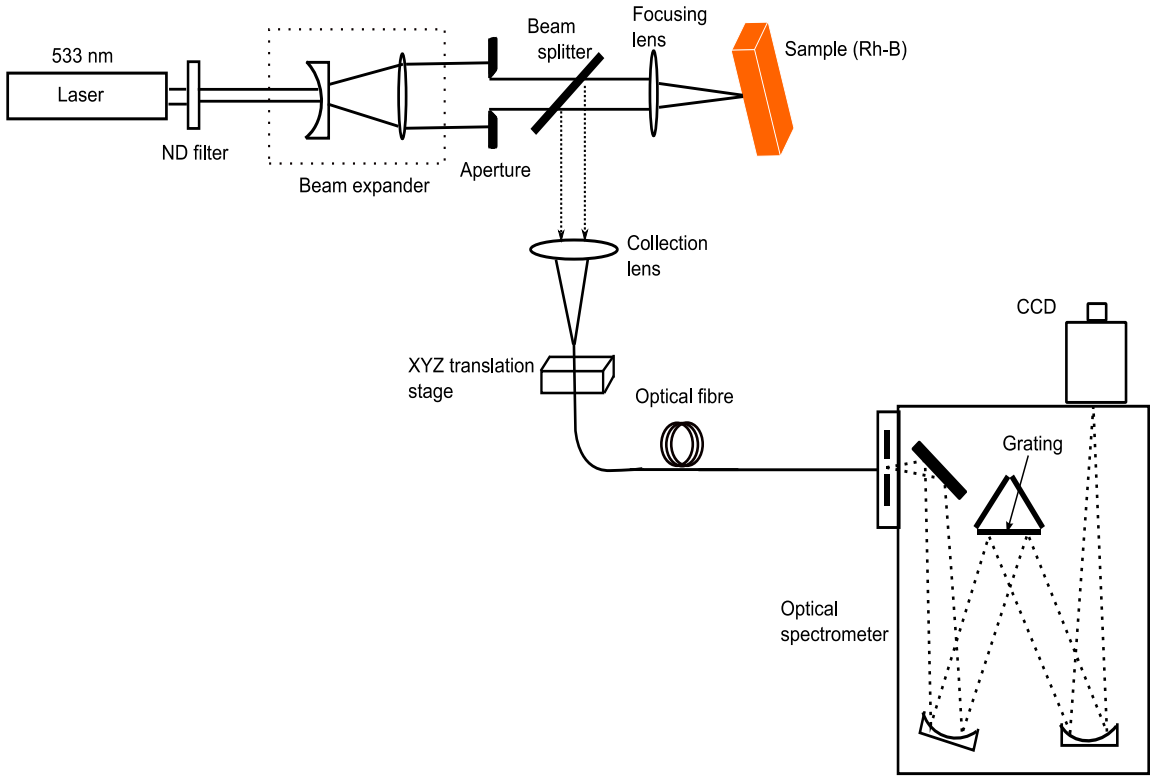

Figure D.1: Schematic representation of experimental setup for verification. (The actual physical setup is shown in Figure D.2)

A beam expander (a combination of concave and convex lens) was used to expand and collimate the pump beam and then send it onto the aperture as shown in Figure D.1. The size (diameter) of the aperture was decreased until the fluorescence signal was collected by the optical fibre as was described in Section 2.6.1. An optical fibre mounted on a XYZ translation stage was used that guided fluorescence signal to the spectrometer. Finally, the fluorescence signal was recorded at the CCD detector.

In this experiment, the fluorescence signal was collected in the opposite direction to incident light (see Figure D.1), thus ensuring accurate overlap of the excited sample volume and the volume used in measuring fluorescence. The fluorescence of a sample was separated with the aid of a beam-splitter and was directed to the collection lens focusing on to the tip of an optical fibre. The fluorescence signal was scanned over the wavelength range from 500 nm to 1100 nm. A photograph of actual experimental setup is shown in Figure D.2.

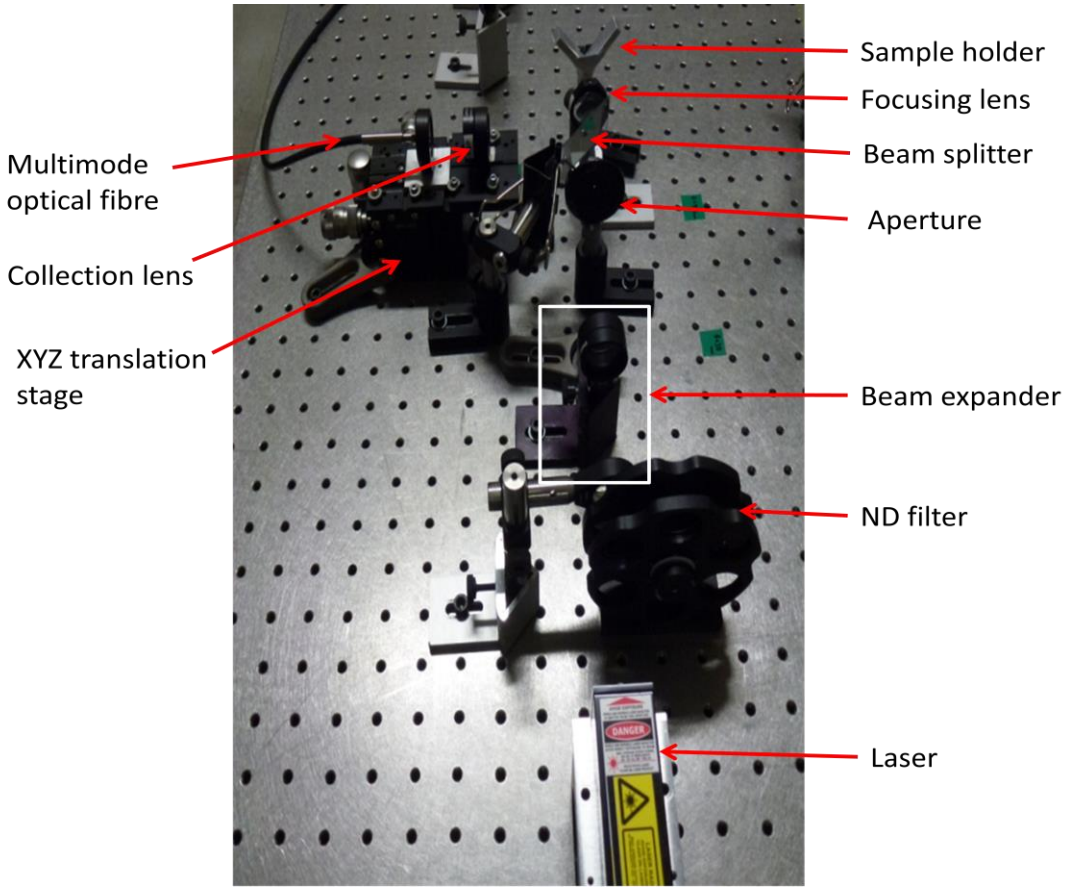

Figure D.2: The photograph of an experimental setup. (Top side view)

D.3 Data analysis

Using the experimental setup drawn schematically in Figure D.1, the experimental data was accumulated. The reference sample (Rh-B) was used with the concentration of 1 μM. The data analysis involves two experimental steps and the measured values as explained below.

Step 1:

Firstly, the background of experimental setup was measured in the form of spectrum using a sample cell, filled with ethanol only, as shown in Figure D.3

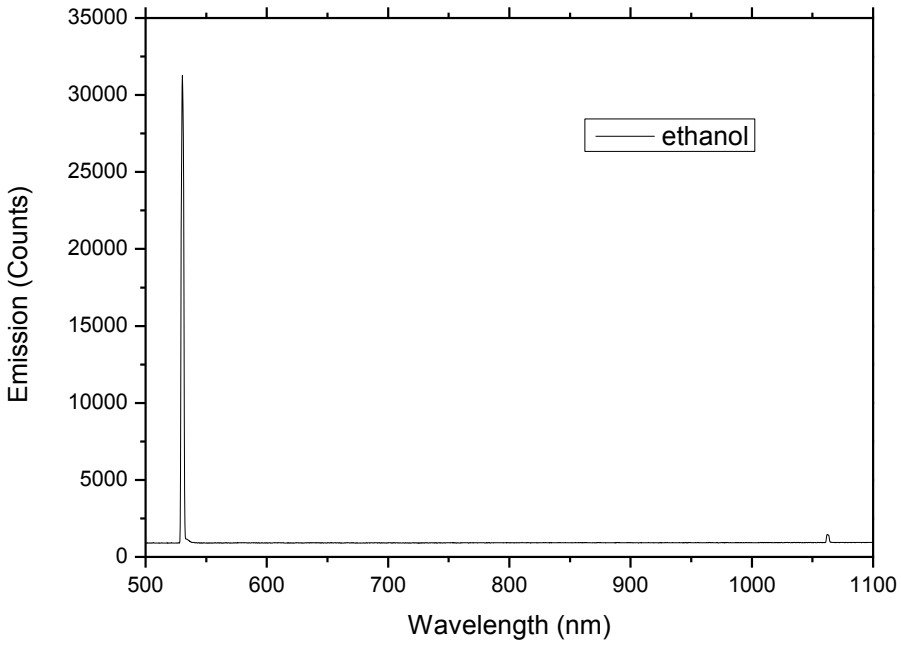

Figure D.3: Background spectrum of experimental setup using a sample cell containing ethanol only.

Step 2:

Then, the emission spectrum was recorded using a sample cell filled with the solution of Rh-B and ethanol, as shown in Figure D.4.

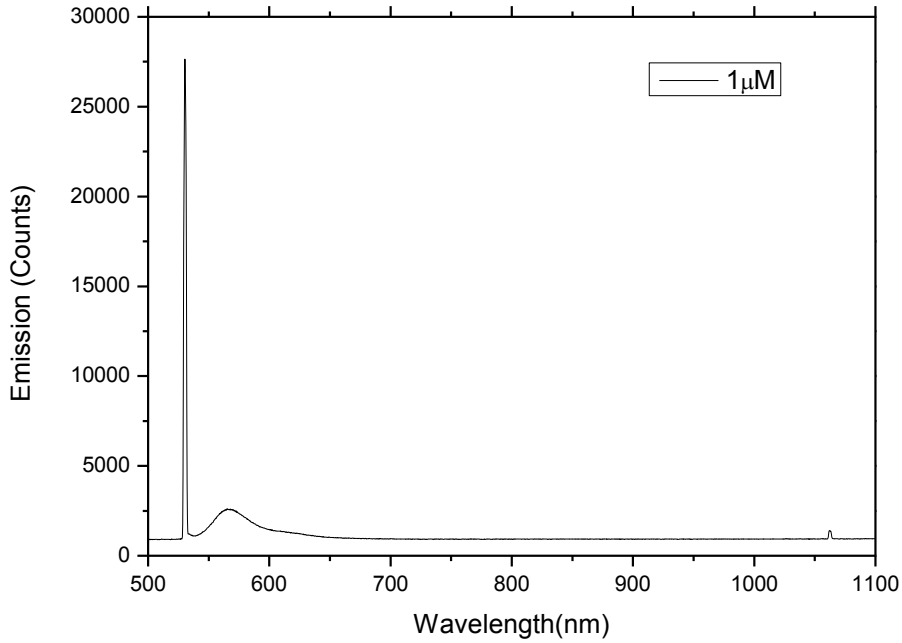

Figure D.4: Emission spectrum of a sample cell containing solution of Rh-B and ethanol.

Step 3:

Finally, the difference emission spectrum is obtained after subtracting step 1 from step 2. The resulting spectrum is shown in Figure D.5.

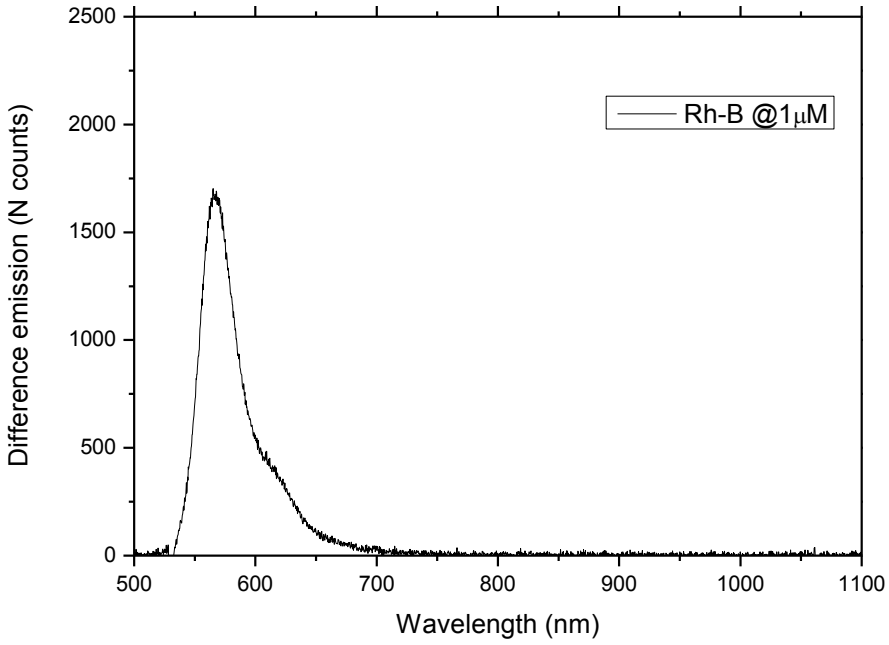

Figure D.5: Difference emission spectrum of Rh-B sample. (The broad peak of the spectrum shows the characteristic fluorescence of Rh-B).

After acquiring emission spectra and experimental data (measured power values listed below), subsequent calculations were performed in order to determine the fluorescence efficiency of Rh-B sample. The calculation procedure is presented below.

Incident power 'P_i' = 37.0 ± 0.6 μW,

Transmitted power 'P_t' = 24.0 ± 0.6 μW, and

Measured emitted power 'P_{meas}' = 32.0 ± 1.2 nW.

The measurements were repeated with the same excitation source and the power meter in order to find uncertainties, thus reflecting the reproducibility, after the experiment was performed. The statistical analysis was performed on the data obtained for 10 sample values. The above quoted values are indicative of $P_{ave} \pm 2\sigma$. The uncertainties were calculated by considering level of confidence as 2σ being conservative. The power measurements were repeated both by blocking the beam emanating from the laser and by moving the detector away from the beam path and bringing back detector to measure the optical power. The repeated measurements were consistent with the previous measurement except not taking multiple readings.

The fluorescence power '$P_{f'}$' at a detector position was calculated using Equation (2.8) i.e.

$$P_{f'} = \frac{(P_{meas}) \times (Area\ under\ the\ curve\ of\ difference\ fluorescence\ spectrum)}{Total\ area\ under\ the\ curve\ of\ fluorescence\ spectrum}.$$

$$P_{f'} = \frac{(32\times10^{-9})\times(148184)}{751640} = 6.3\ \text{nW}.$$

Next we used the following parameters to calculate the value of a fraction of solid angle ‘Ω’ as given below

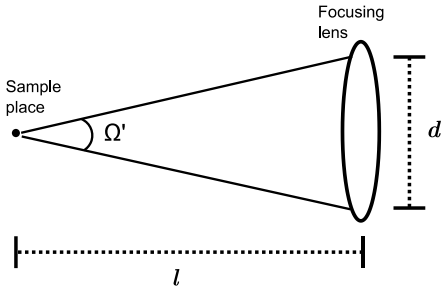

d = 1.50 ± 0.06 mm, and

l = 50.0 ± 0.4 mm,

where ‘d’ is the diameter of the aperture and ‘l’ is the distance between the sample and the focusing lens.

The diameter ‘d’ was measured using vernier calliper while the distance ‘l' was measured using a small ruler. Note that the uncertainties in the measurements are two times standard deviation (2σ) of 10 sample values. The distance ‘l’ is measured from the side (along the diameter) of the focusing lens to the sample position.

Since emission from the sample is isotropic, i.e. in the form of a sphere, the total emitted power will be calculated in the following way. Suppose power P_f, is detected over a solid angle Ω', then the total emitted power P_f will be given by

$$P_f = P_{f'}(\frac{4\pi}{\Omega'}).$$

Now first calculate the value of a fraction of solid angle ($\Omega = \Omega'/4\pi$) is

$$\Omega = \frac{\pi d^2}{4l^2} = 7.07 \times 10^{-4}.$$

Then the value of total fluorescence poweremitted by the sample is

$$P_f = 9\ \mu W.$$

Finally, the efficiency ‘η’ was calculated by expression (2.9) i.e.

$$\eta = \frac{P_f}{P_i}.$$

Using values of P_f and P_i in above formula, we obtain

$$\eta = 0.69. \text{ or } \eta\ (\%) = 69\%.$$

In above expression the value of absorbed power is used in order to compare with the literature value of efficiency as explained below.

D.4 Error estimation

The total estimated uncertainty was calculated by following the error propagation approach. The uncertainty ($\Delta\eta$) in efficiency measurement is determined by using the following expression

$$\frac{\Delta\eta}{\eta} = \frac{\Delta P_f}{P_f} + \frac{\Delta P_i}{P_i}, \tag{D.1}$$

where η, P_i, and P_f is the efficiency, incident and the total fluorescence power whereas $\Delta\eta$, ΔP_i, and ΔP_f is corresponding associated errors.

The value of each quantity in above expression is known except 'ΔP_f', which we find by performing the following calculations:

Writing Equation (2.8) in compact form as

$$P_{f'} = \frac{P_{meas} \times A_{DS}}{A_S},$$

where A_{DS} and A_S correspond to the areas under the curve of difference fluorescence spectrum and the total area under the curve of fluorescence spectrum respectively, P_{meas} is the measured emitted power and $P_{f'}$ is the calculated fluorescence power at a certain position.

To find the error in '$P_{f'}$' following the simple error propagation, we can write

$$\frac{\Delta P_{f'}}{P_{f'}} = \frac{\Delta P_{meas}}{P_{meas}}, \tag{D.2}$$

$$P_{f'} = \left(\frac{\Delta P_{meas}}{P_{meas}}\right) P_{f'}.$$

The total fluorescence power (P_f) was calculated by

$$P_f = P_{f'}\left(\frac{4\pi}{\Omega'}\right), \tag{D.3}$$

where Ω′ is the solid angle, which is given by

$$\Omega' = \frac{\pi r^2}{\ell^2}. \tag{D.4}$$

From Equations (D.3) and (D.4), we have

$$P_f = P_{f'}\left(\frac{16\ell^2}{d^2}\right).$$

We can then write

$$\frac{\Delta P_f}{P_f} = \frac{2\Delta \ell}{\ell} + \frac{2\Delta d}{d} + \frac{\Delta P_{f'}}{P_{f'}}.$$

Now using Equation (D.2) in above expression, then

$$\frac{\Delta P_f}{P_f} = \frac{2\Delta \ell}{\ell} + \frac{2\Delta d}{d} + \frac{\Delta P_{meas}}{P_{meas}}, \tag{D.5}$$

The total uncertainty ($\Delta\eta$) in the efficiency value was calculated by combining Equations (D.1) and (D.5), we then obtain

$$\frac{\Delta \eta}{\eta} = \frac{\Delta P_i}{P_i} + \frac{2\Delta \ell}{\ell} + \frac{2\Delta d}{d} + \frac{\Delta P_{meas}}{P_{meas}}. \tag{D.6}$$

Substituting values in above expression

$$\frac{\Delta\eta}{\eta} = 0.0167 + 0.0160 + 0.0800 + 0.0387.$$

$$\Delta\eta = 0.151 \times \eta$$

$$\Delta\eta = 0.104$$

The final value of fluorescence efficiency of Rh-B is

$$\eta\ (\%) = (69 \pm 10)\%.$$

Now we compare our experimental fluorescence efficiency with the known value of efficiency for the Rh-B in the literature [97], thus finding the relative difference. The experimental and the known quantum efficiency of Rh-B are 0.69 and 0.65 respectively. Our experimental value of efficiency is consistent with the known value and is found to be within 1σ.

D.5 Analysis and discussion

The knowledge of possible effects on fluorescence and efficiency measurement is essential to exploit the use of experimental technique at its maximum potential. The accurate measurement of efficiency is much more difficult than it first appears because of the limitations of instruments used (see below) and the presence of potential external influences.

We first discuss the excitation light source (laser) and the fluctuations associated with its beam. The laser beam can be affected by a number of factors both internal and external to the laser itself. These contributing factors may include the physical motion of the laser, intrinsic losses in the laser cavity medium (instability), heat build-up, air currents, and the presence of external light (stray light). The stray light was avoided by conducting an experiment in the dark laboratory. The instability of the laser beam was minimized by both running the

laser for 10 to 15 min prior to measurement, allowing it to reach the maximum stability (±2% - as quoted by manufacturer), and performing the statistical averaging of multiple measurements. The other error (random) was related to the power measurements such as moving an optical fibre away and trying to bring back to exactly the same position to measure the power. Finally, the largest source of error being the relative error, as can be seen in calculations, was in the measurement of diameter (d) of the aperture the accuracy of which was limited by systematic errors related to the use of vernier calliper. The second largest error is the absolute error in the measured value of the emitted power. While we have shown that the method used will work, it can be refined to gain more accurate results in later experiments if needed.

Appendix E

Fluorescence quantum efficiency calculations

As was explained in Section 2.6.2, a simple data analysis approach was used to determine the fluorescence quantum efficiency FQE. Four samples with concentrations were investigated in this study. The experimental steps performed to obtain the FQE are described. We provide all spectra and measured value for a sample (Er0.2Yb9.8), which is given below. FQE of all other samples was calculated by following a similar procedure.

In the present case, the calculations performed on the sample (No. 3 as labelled in Table 2.2) are presented together with the measured emission spectra.

Sample: Er0.2Yb9.8

Step1:

Firstly, the background of the experimental setup was measured in the form of spectrum without a sample as shown in Figure E.1

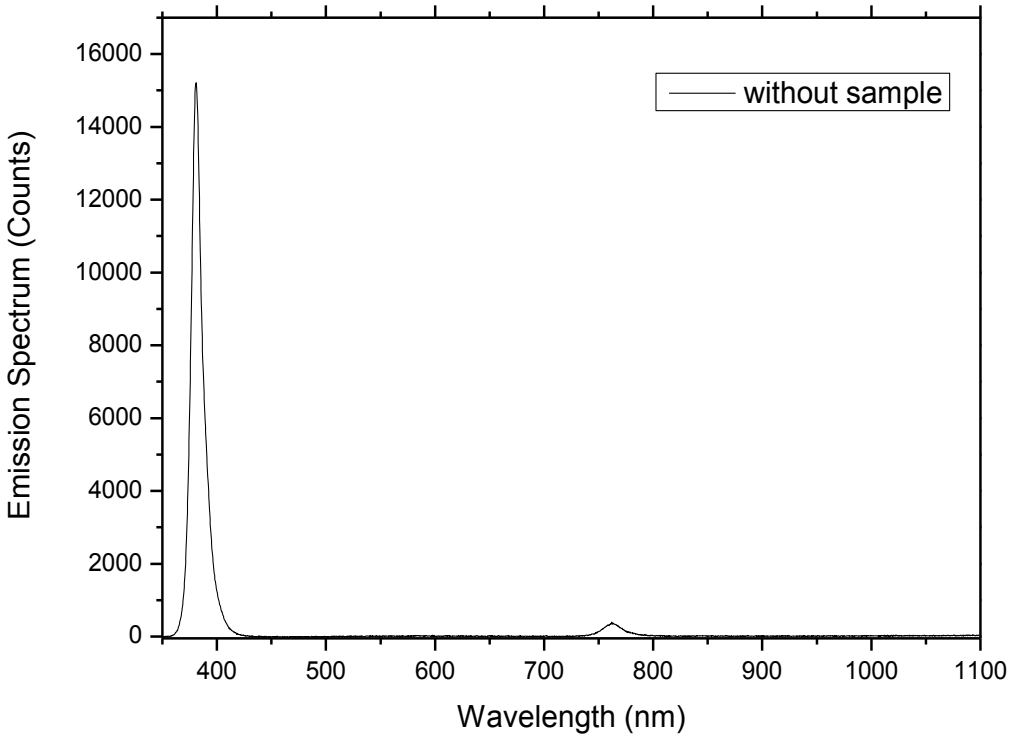

Figure E.1: Background spectrum of the experimental setup recorded without sample. (Spectral peak around 380 nm indicates the pump light while a peak around 760 nm indicates the second order of the pump light)

Step 2:

Then, the emission spectrum was recorded with a sample placed in the path of the incident pump beam as shown in Figure E.2.

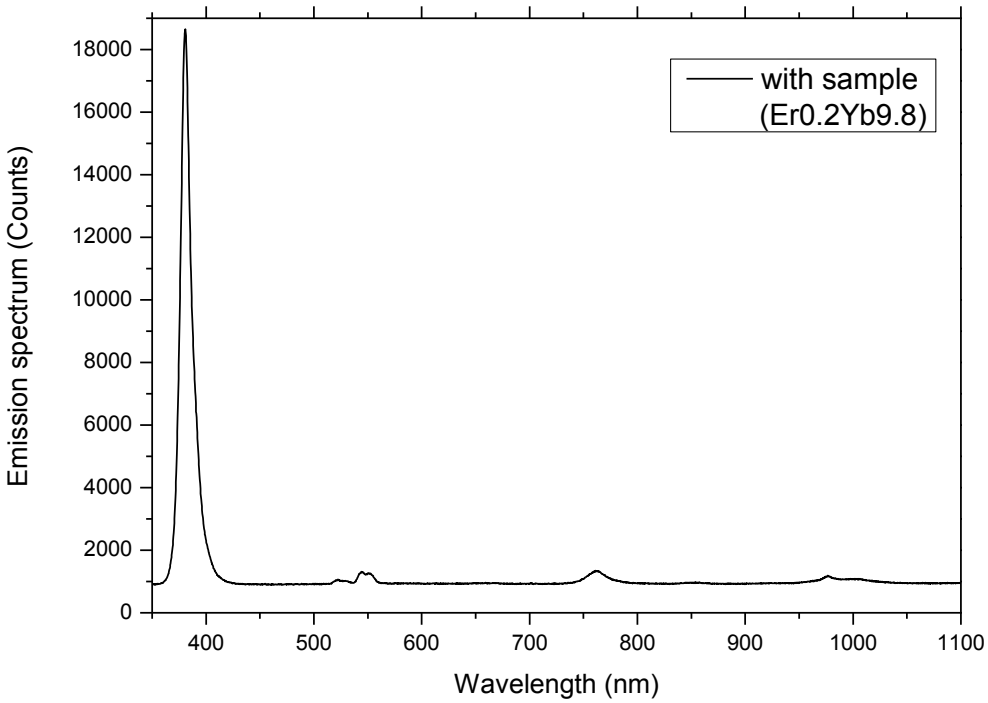

Figure E.2: Emission spectrum of a sample. (Spectral peaks other than pump (380 nm) and its 2nd order (760 nm) correspond to the dopants present in the sample)

Note that the above steps were taken using an identical setup but with different integrating time which results in different counts on the detector. For an accurate result, the two spectra should have been normalized for the same total count prior to subtraction. This was not done for these preliminary results since the emission was very low. Normalization will be performed for later experimental results once new samples are obtained.

Step 3:

Finally, the difference fluorescence spectrum was obtained by subtracting spectrum recorded in step 1 from the spectrum recorded in step 2, which is plotted in Figure E.3.

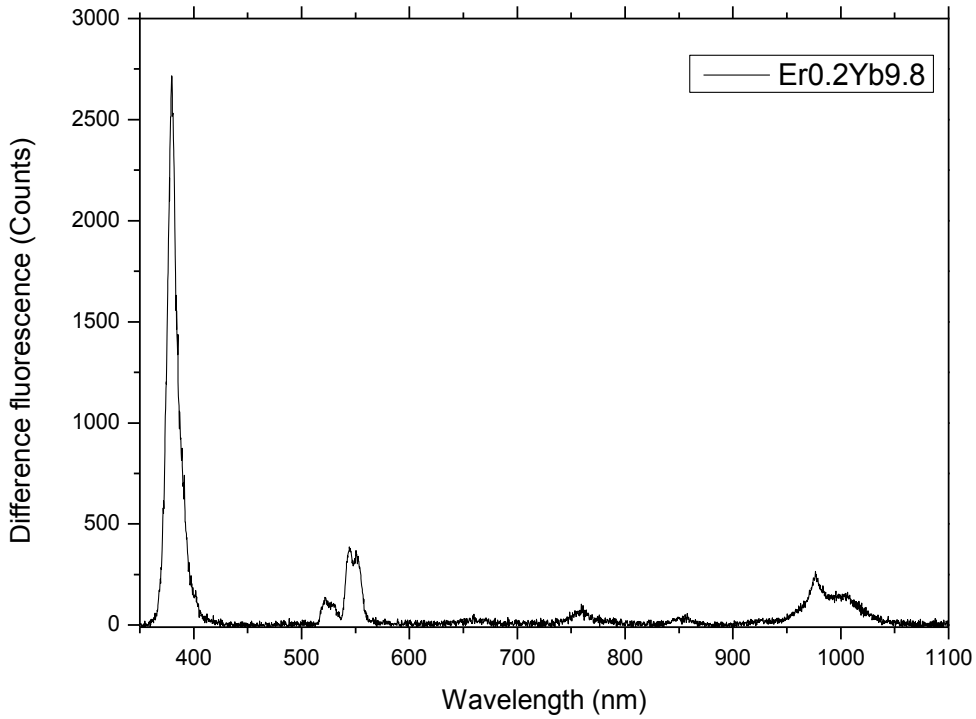

Figure E.3: Difference fluorescence spectrum of a sample. (Spectral peaks around 525 nm, 550 nm, 660 nm, 850 nm, and 960 nm correspond to the dopants present in the sample)

The measurement of quantum/fluorescence efficiency is highly prone to experimental errors; all power measurements listed below were measured by using a single power meter in order to minimize experimental errors.

Incident power 'P_i' = 31.0 ± 0.6 μW,

Transmitted power 'P_t' = 19.5 ± 0.6 μW,

Reflected power 'P_r' = 4.5 ± 0.6 μW, and

Measured emitted power 'P_{meas}' = 51.0 ± 1.2 nW.

Note that the measurement uncertainties quoted above were obtained from the statistical analysis of multiple measured power values using a single optical power meter.

The fluorescence power at a certain position was calculated by using Equation (2.8), following the same procedure outlined in Appendix D, we obtain

$$P_{f'} = \frac{(51 \times 10^{-9}) \times (23307)}{298016},$$

$$P_{f'} = 4.0\, nW.$$

Now we calculate the fraction of solid angle 'Ω' to find out the total fluorescence power 'P_f' emitted by the sample. Considering the geometry of the experimental setup, we measured the following parameters as given below. For more information, please refer to Sections 2.6.1 and 2.6.2.

Determining the solid angle:

Diameter 'd' = 8.50 ± 0.07 mm, and

Distance 'l' = 50.0 ± 0.4 mm.

The value of a fraction of solid angle ($\Omega = \Omega'/4\pi$) is

$$\Omega = \frac{\pi d^2}{4l^2} = 2.27 \times 10^{-2}.$$

The total fluorescence power emitted by the sample into 4π steradians is thus

$$P_f = \frac{P_{f'}}{\Omega} = 0.18\, \mu W.$$

Since we were interested in the near-infrared (NIR) range which we defined as the region of interest (ROI) ranging from 950 nm to 1100 nm, the fluorescence quantum efficiency (FQE) will be

$$P_{f'} = \frac{(51 \times 10^{-9}) \times (9874)}{298016}.$$

$$P_{f'} = 1.7\ nW.$$

So, the total fluorescence power into 4π steradians is

$$P_f = 0.80\ nW.$$

Finally the efficiency was calculated using value of P_f and P_i as

$$\eta = \frac{P_f}{P_i} = 0.026.$$

Or,

$$\eta(\%) = 2.6\%.$$

Now to find out the error '$\Delta\eta$' in the efficiency value, the simple error propagation is followed as was discussed in Appendix D. We write Equation (E.6) again,

$$\frac{\Delta\eta}{\eta} = \frac{\Delta P_i}{P_i} + \frac{2\Delta\ell}{\ell} + \frac{2\Delta d}{d} + \frac{\Delta P_{meas}}{P_{meas}}.$$

Substituting the values, we obtain:

$$\Delta\eta = 0.0755 \times \eta.$$

$$\Delta\eta(\%) = 0.2\%.$$

So the final value of efficiency for the sample (Er0.2Yb9.8) is

$$\eta\ (\%) = (2.6 \pm 0.2)\%.$$

Appendix F

Energy levels diagram of rare-earth ions

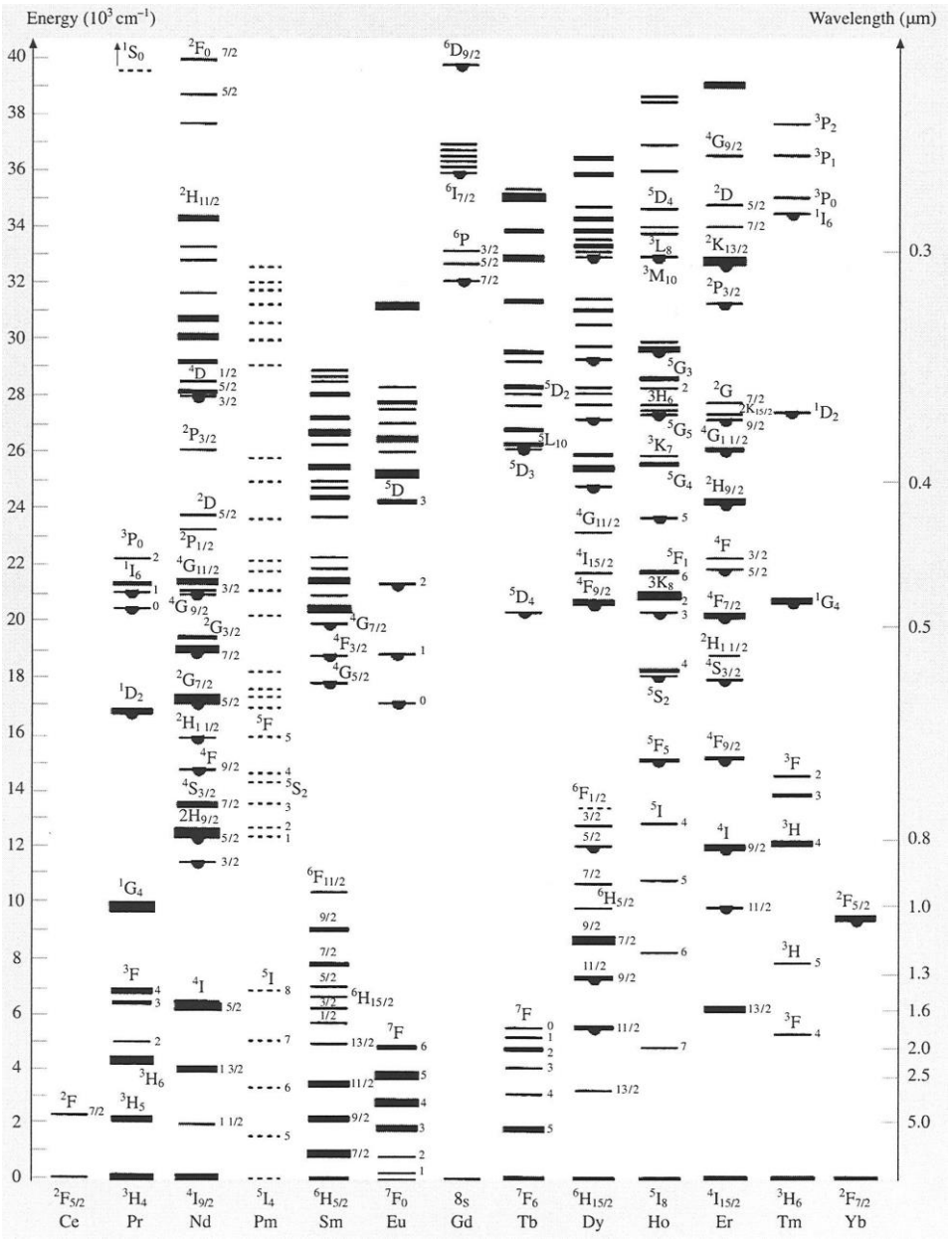

Figure F.1: Dieke's energy levels diagram of rare-earth ions[8]

[8] Figure adopted from reference [98]

APPENDIX: F

Bibliography

[1] P. Bosshard, W. Herman, E. Hung, R. Hunt, and A.J. Simon, An assessment of solar energy conversion technologies and research opportunities, GCEP Technical Report, 2005

[2] Energy flow charts: 2.7 YJ solar energy each year for two billion years vs 1.4 YJ non-renewable resources available, 2012, http://gcep.stanford.edu/ research/exergycharts.html

[3] National Renewable Energy Lab., Reference solar spectral irradiance: Air mass 1.5, ASTM Standard G173-03, 2011, http://rredc.nrel.gov/ solar/spectra/ am1.5/ASTMG173/ASTM173.html

[4] A. Goetzberger, C. Hebling, and H.W. Schock, Photovoltaic materials, history, status, and outlook, Mater. Sc. Engg. R, 40 (2003) 1

[5] A. Luque and S. Hedegus, Handbook of Photovoltaic Science and Engineering, John Wiley & Sons Ltd., 2003

[6] N. Gupta, G.F. Alapatt, R. Podila, R. Singh, and K.F. Poole, Prospects of nanostructures-based solar cells for manufacturing future generations of photovoltaic modules, Inter. J. Photoenergy, 154059 (2009) 1

[7] M.A. Green, Third Generation Photovoltaics: Advanced Solar Energy Conversion, Springer-Verlag, 2003.

[8] W. Schockley and H.J. Queisser, Detailed balance limit of efficiency of p-n junction solar cells, J. Appl. Phys., 32 (1961) 510

[9] M.C. Beard, K.P. Knutsen, P. Yu, J.M. Luther, Q. Song, W.K. Metzger, R.J. Ellingson, and A.J. Nozik, Multiple exciton generation in colloidal silicon nanocrystals, Nano Lett., 7 (2007) 2506

[10] T. Trupke, M.A. Green, and P. Wurfel, Improving solar cell efficiencies by down-conversion of high energy photons, J. Appl. Phys., 92 (2002) 1668

[11] N. Hamelin, P.G. Kik, J.F. Suyver, K. Kikoin, A. Polman, A. Schoneckner, and F.W. Saris, Energy back transfer and infrared photoresponse in erbium-doped silicon p-n junction diodes, J. Appl. Phys., 88 (2000) 5381

[12] P. Wurfel, Solar energy conversion with hot electrons from impact ionisation, Sol. Energy Mater. Sol. Cells, 46 (1997) 43

[13] A. Luque and A. Marti, Increasing the efficiency of ideal solar cells by photon induced transitions at intermediate levels, Phy. Rev. Lett., 78 (1997) 5014

[14] T. Trupke, M.A. Green, and P. Wurfel, Improving solar cell efficiencies by up-conversion of sub band-gap light, J. Appl. Phys., 92 (2002) 4117

[15] B.S. Richards, Enhancing the performance of silicon solar cells via the application of passive luminescence conversion layers, Sol. Energy Mater. Sol. Cells, 90 (2006) 2329

[16] A. Marti and A. Luque, Next Generation Photovoltaics: High Efficiency through Full Spectrum Utilization, IoP Publishing, 2004

[17] M. Wolf, Limitations and possibilities for improvement of photovoltaic solar energy converters, Part - I, Proc. IRE, 48 (1960) 1246

[18] A. de Vos, Photovoltaic solar energy conf., (Ispra: European Commission), Proc., E.C., 5 (1983) 186

[19] A.S. Brown and M.A. Green, Impurity photovoltaic effect: Fundamental energy conversion efficiency limits, J. Appl. Phys., 92 (2002) 1329

[20] R. Ross and A.J. Nozik, Efficiency of hot-carrier solar energy converters, J. Appl. Phys., 53 (1982) 3813

[21] G. Conibeer, M.A. Green, R. Corkish, Y. Cho, E.C. Cho, C.W. Jiang, T. Fangsuwannarak, E. Pink, Y. Huang, T. Puzzer, T. Trupke, A. Shalav, and K.L. Lin, Silicon nanostructures for third generation photovoltaic cells, Thin Sol. Films, 511 (2006) 654

[22] T. Justel, H. Nikol, and C. Ronda, New developments in the field of luminescent materials for lighting and displays, Angew Chem., Int. Ed., 37 (1998) 3048

[23] B.S. Richards, Luminescent layers for enhanced silicon solar cell performance: Downconversion, Sol. Energy Mater. Sol. Cells, 90 (2006) 1189

[24] F. Auzel, Up-conversion and anti-stokes processes with f and d ions in solids, Chem. Rev., 104 (2004) 139

[25] B. Henderson and G.F. Imbusch, Optical Spectroscopy of Inorganic Solids, Oxford University Press, 1989

[26] G. Liu, Spectroscopic Properties of Rare-earths in Optical Materials, Springer-Verlag, 2005

[27] D. Dexter, Possibility of luminescent quantum yields greater unity, Phys. Rev., 108 (1957) 630

[28] J.L. Sommerdijk, A. Bril, and A.W. de Jager, Two photon luminescence with ultraviolet excitation of trivalent praseodymium, J. Lumin., 8 (1974) 341

[29] W. Piper, J. DeLuca, and F. Ham, Cascade fluorescent decay in Pr^{3+} doped fluorides: achievement of a quantum yield greater than unity for emission of visible light, J. Lumin., 8 (1974) 344

[30] R.T. Wegh, H. Donker, K.D. Oskam, and A. Meijerink, Visible quantum cutting in LiGdF:Eu^{+3} through downconversion, Science, 283 (1999) 663

[31] J.L. Sommerdijk, A. Bril, and A.W. de Jager, Luminescence of Pr^{3+} - activated fluorides, J. Lumin., 9 (1974) 288

[32] R. Rappalardo, Calculated quantum yields for photon-cascade emission (PCE) for Pr^{3+} and Tm^{3+} in fluoride hosts, J. Lumin., 14 (1976) 159

[33] R.T. Wegh, D. Donker, A. Meijerink, R. Lamminmaki, and J. Hosla, Vacuum-ultraviolet spectroscopy and quantum cutting for Gd^{3+} in $LiYF_4$, Phys. Rev. B, 56 (1997) 13841

[34] K.D. Oskam, R.T. Wegh, H. Donker, E.V.D van Loef, and A. Meijerink, Quantum cutting through downconversion in rare-earth compounds, J. Lumin., 87 (2000) 1017

[35] C. Feldmann, T. Justel. C. Ronda, and D. Wiechert, Quantum efficiency of downconversion phosphor $LiGdF_4$: Eu, J. Lumin., 92 (2001) 245

[36] K.D. Oskam, R.T. Wegh, H. Donker, E.V.D. van Loef, and A. Meijerink, Downconversion: a new route to visible quantum cutting, J. Alloy Comp., 300 (2000) 421

[37] P. Vergeer, T. Vlugt, M. Kox, M. den Hertog, J. van der Eerden, and A. Meijerink, Quantum cutting by cooperative energy transfer in $Yb_xY_{1-x}PO_4$: Tb^{3+}, Phys. Rev. B, 71 (2005) 014119

[38] G. Lakshminarayana, H. Yang, S. Ye, Y. Liu, and J. Qiu, Co-operative downconversion luminescence in $Tm^{3+}/Yb^{3+}:SiO_2–Al_2O_3–LiF–GdF_3$ glasses, J. Phys. D: Appl. Phys., 41 (2008) 175111

[39] S. Ye, B. Zhu, J. Luo, J. Chen, G. Lakshminarayana, and J. Qiu, Enhanced cooperative quantum cutting in Tm^{3+}-Yb^{3+} codoped glass ceramics containing LaF_3 nanocrystals, Opt. Express, 16 (2008) 8989

[40] Q. Zhang, G.F. Yang, and Z. Jiang, Cooperative downconversion in $GdAl_3(BO_3)_4:RE^{3+},Yb^{3+}$ (RE = Pr, Tb, and Tm), Appl. Phys. Lett., 91 (2007) 051903

[41] G. Lakshminarayana and J. Qiu, Near-infrared quantum cutting in RE^{3+}/Yb^{3+} (RE = Pr, Tb, and Tm): GeO_2-B_2O_3-ZnO-LaF_3 glasses via downconversion, J. Alloy Comp., 481 (2009) 582

[42] D. Chen, Y. Weng, Y. Yu, P. Huang, and F. Weng, Near-infrared quantum cutting in transparent nanostructured glass ceramics, Opt. Lett., 33 (2008) 1884

[43] B.M. van der Ende, L. Aarts, and A. Meijerink, Near-Infrared quantum cutting for photovoltaics, Adv. Mater., 21 (2009) 3073

[44] G.H. Dieke and H. Crosswhite, Spectra and Energy Levels of Rare-earth Ions in Crystals, John Wiley & Sons Ltd., 1968

[45] M.J. Weber, Science and technology of laser glass, J. Non-Cryst. Sol., 123 (1990) 208

[46] J.S. Wang, E.M. Vogel, and E. Snitzer, Tellurite glass: a new candidate for fibre devices, Opt. Mater., 3 (1994) 187

[47] T. Monro and H.E. Heidepriem, Progress in microstructured optical fibres, Ann. Rev. Mat. Res., 36 (2006) 467

[48] S. Manning, A Study of Tellurite Glasses for Electro-optic Optical Fibre Devices, Ph.D Thesis, The University of Adelaide, Australia, 2011

[49] P.W. Atkins, Physical Chemistry, 5th Edition, Oxford University Press, 1994

[50] J.R. Lakowicz, Principles of Fluorescence Spectroscopy, 3rd Edition, Plenum Press, 1983

[51] F.L. Pedrotti and L.S. Pedrotti, Introduction to Optics, 2nd Edition, Princeton Hall Inc., 1993

[52] J.W. Verhoeven, Glossary of terms used in photochemistry, Pure and Appl. Chem., 68 (1996) 2223

[53] E. Hecht, Optics, 4th Edition, Addison-Wesley Longman Publishing Co., 2004

[54] G. Ghosh, Sellmeier coefficients and chromatic dispersions for some tellurite glasses, J. Am. Ceram. Soc., 78 (1995) 2828

[55] M.R. Oerman, H.E. Heidepriem, Y. Li, T.Z. Foo, and T. Monro, Index matching between passive and active tellurite glasses for use in microstructured fiber lasers: Erbium doped lanthanum-tellurite glass, Opt. Express, 17 (2009) 15578

[56] R.A.H. El-Mallawany, Tellurite Glasses Handbook: Physical Properties and Data, CRC Press LLC, 2002

[57] J.F. Suyver, A. Aebischer, D. Biner, P. Gerner, J. Grimm, S. Heer, K.W. Kramer, C. Reinhard, and H.U. Gudel, Novel materials doped with lanthanides and transition metal ions showing near-infrared to visible photon upconversion, Opt. Mater., 27 (2005) 1111

[58] L. Aarts, B.M. van der Ende, and A. Meijerink, Downconversion for the Er, Yb couple in KPb_2Cl_5 – A low-phonon frequency host, J. Lumin., 131 (2011) 618

[59] L. Aarts, B.M. van der Ende, and A. Meijerink, Downconversion for solar cells in $NaYF_4$: Er,Yb, J. Appl. Phys., 106 (2009) 023522

[60] H.U. Gudel and M. Pollnau, Near-infrared to visible photon upconversion processes in lanthanide doped chloride, bromide and iodide lattices, J. Alloys Comp., 303 (2000) 307

[61] G. Blasse and B.C. Grabmaier, Luminescent Materials, Springer-Verlag, 1994

[62] R. Reisfeld, Inorganic ions in glasses and polycrystalline pellets as fluorescence standard reference materials, J. Res. NBS. Sect. A: Phys. Ch., 76A (1972) 613

[63] L.R. Wilson and B.S. Richards, Measurement method for photoluminescent quantum yields of fluorescent organic dyes in polymethyl methacrylates for luminescent solar concentrators, App. Opt., 48 (2), (2009) 212

[64] J.N. Demas and G.A. Crosby, Measurement of photoluminescence quantum yields. A review, J. Phys. Chem., 75 (1971) 991

[65] J.C. deMello, H.F. Wittmann, and R.H. Friend, An improved experimental determination of external photoluminescent quantum efficiency, Adv. Mater., 9 (1997) 230

[66] C.V. Bindhu, S.S. Harilal, G.K. Varier, R.C. Issac, V.P.N. Nampoori, and C.P.G. Vallabham, Measurement of the absolute fluorescence quantum yield of rhodamine B solution using a dual beam thermal lens technique, J. Phys. D: Appl. Phys., 29 (1996) 1074

[67] L.-O. Palsson and M.P. Monkman, Measurements of solid-state photoluminescence quantum yields of films using a fluorimeter, Adv. Mater., 14 (2002) 757

[68] Q. Duan, F. Qin, D. Wang, X. Xu, J. Cheng, Z. Zhang, and W. Cao, Quantum cutting mechanism in Tb-Yb co-doped oxyfluoride glass, J. Appl. Phys., 110 (2011) 113503

[69] B.M. van der Ende, L. Aarts, and A. Meijerink, Lanthanide ions as spectral converters for solar cells, Phys. Chem. Chem. Phys., 11 (2009) 11081

[70] K. Sanderson, Quantum dots go large, Nature, 459 (2009) 760

[71] J.S. Batchelder, A.H. Zewail, and T. Cole, Luminescent solar concentrator: Experimental and theoretical analysis of their possible efficiencies, App. Opt., 20 (1981) 3733

[72] Exciton Inc., Organic fluorescence dyes datasheet and product information, 2011, http://www.exciton.com/products.html

[73] A. Goetzberger and W. Greubel, Solar energy conversion with fluorescent collectors, Appl. Phys., 14 (1977) 123

[74] J.M. Drake, M.L. Lesiecki, J. Sansregret, and W.R.L Thomas, Organic dyes in PMMA in a planar solar concentrator: a performance evaluation, Appl. Opt., 21 (1982) 2945

[75] A.A. Earp, G.B. Smith, J. Franklin, and P. Swift, Optimisation of a three-colour luminescent solar concentrator day-lighting system, Sol. Energy Mat. Sol. Cells, 84 (2004) 411

[76] BASF Corporation, Lumogen F dyes product informatiom sheet, 2011, http://www.basf.com/productfinder.html

[77] L. Etgar, Semiconductor nanocrystals as light harvesters in solar cells, Materials, 6 (2013) 445

[78] A.P. Alivisatos, Perspectives on the physical chemistry of semiconductor nanocrystals, J. Phys. Chem., 100 (1996) 13226

[79] R.E. Sah and G. Baur, Influence of the solvent matrix on the overlapping of the absorption and emission bands of solute fluorescent dyes, Appl. Phys., 23 (1980) 369

[80] B.C. Rowan, L.R. Wilson, and B.S. Richards, Advanced material concepts for luminescent solar concentrators, IEEE J. Sel. Top. Quant. Phys., 14 (2008) 1312

[81] H. Du, C. Chen, R. Krishnan, T.D. Krauss, J.M. Harbold, F.W. Wise, M.G. Thomas, and J. Silcox, Optical properties of colloidal PbSe nanocrystals, Nano Lett., 2 (2002) 1321

[82] Nanoco Technologies Ltd., Nanoco group quantum dot products information, 2011, http://www.nanotechnologies.com

[83] S.J. Gallagher, B.C. Rowan, J. Doran, and B. Norton, Quantum dot solar concentrators, Device optimisation using spectroscopic techniques, Sol. Energy, 81 (2007) 540

[84] D. Timmermann, I. Izeddin, P. Stallinga, I.N. Yassievich, and T. Gregorkiewicz, Space-separated quantum cutting with silicon nanocrystals for photovoltaic applications, Nature Photon., 2 (2008) 105

[85] R.M. Mach, G. Mueller, M.R. Krames, H.A. Hoppe, F. Stadler, W. Schnick, T. Juestel, and P. Schmidt, Highly efficient all-nitride phosphor-converted white light emitting diode, Phys. Status Solidi A, 202 (2005) 1727

[86] J. Ueda and S. Tanabe, Visible to near infrared conversion in Ce-Yb co-doped YAG ceramics, J. Appl. Phys., 106, (2009) 043101

[87] C. Jindeng, Z. Hao, L. Fang, and G. Hai, High efficient near-infrared quantum cutting in Ce-Yb co-doped $LuBO_3$ phosphors, Mater. Chem. Phys., 128 (2011) 191

[88] R. Reisfeld, H. Munti, A. Patra, D. Ganguly, and M. Gaft, Spectroscopic properties of Cerium in glasses and their comparison with crystals, Spec. Chem. Acta, 54 (1998) 2134

[89] X. Liu, Y. Teng, Y. Zhuang, J. Xie, Y. Qiao, G. Dong, D. Chen, and J. Qiu, Broadband conversion of visible light to near infrared emission by Ce–Yb co-doped yttrium aluminium garnet (YAG), Opt. Lett., 34 (2009) 3565

[90] A. Winterstein, S. Manning, H.E. Heidepriem, and L. Wondraczek, Luminescence from bismuth-germanate glasses and its manipulation through oxidants, Opt. Mater. Express, 2 (2012) 1320

[91] PerkinElmer Inc., FTIR Software, 2013, http://www.perkinelmer.com/au/Catalog/Category/ID/FTIR20Software

[92] J. Garcia, L.E. Bausa, and D. Jaque, An Introduction to the Optical Spectroscopy of Inorganic Solids, John Wiley & Sons Ltd., 2005

[93] H.E. Heidepriem and D. Ehrt, UV radiation effects in phosphate glasses, J. Non-Cryst. Solids, 196 (1996) 113

[94] G.E. Jellison and R.F. Wood, Antireflection coatings for planar silicon solar cell, Sol. Cells, 18 (1986) 93

[95] T. Tiedie, E. Yablonovitch, G.D. Cody, and B.G. Brooks, Limiting efficiency of silicon solar cells, IEEE Trans. Electron Dev., 31 (1984) 711

[96] P. Sheng, A.N. Bloch, and R.S. Stepleman, Wavelength-selective absorption enhancement in thin-film solar cells, Appl. Phys. Lett., 43 (1983) 579

[97] R.F. Kubin and A.N. Fletcher, Fluorescence quantum yields of some Rhodamine dyes, J.Lumin., 27 (1982) 455

[98] S. Kasap and P. Capper, Handbook of Electronic and Photonic Materials, Springer-Verlag, 2007